Synchronized PIV-PLIF Experiments on Mixing in Confined Space by a Decelerating, Turbulent, Buoyant Jet

Submitted in partial fulfillment of
the requirements for the award of the degree of

Master of Science
in
Engineering

Submitted by
Albin Prince John

Engineering Mechanics Unit
Jawaharlal Nehru Centre for Advanced Scientific Research
Jakkur PO. Bangalore, India, 560064
December 2019

.

To my parents and grandmother

Declaration

I declare that the MS Research Report titled **Synchronized PIV-PLIF Experiments on Mixing in Confined Space by a Decelerating, Turbulent, Buoyant Jet**, is an original report of my experimental research, has been written by me and has not been submitted for any previous degree. The experimental work is almost entirely my own work; the collaborative contributions have been indicated clearly and acknowledged. Due references have been provided on all supporting literatures and resources.I declare that this research report was composed by myself, that the work contained herein is my own except where explicitly stated otherwise in the text, and that this work has not been submitted for any other degree or professional qualification. I acknowledge the support I had received for my research from Bhabha Atomic Research Centre, Mumbai.

Albin Prince John
2016/09/S0610, MS Engineering
Engineering Mechanics Unit
JNCASR, Jakkur
December 2019

Certificate

I hereby certify that the matter embodied in this MS Research Report entitled **Synchronized PIV-PLIF Experiments on Mixing in Confined Space by a Decelerating, Turbulent, Buoyant Jet** has been carried out by **Mr. Albin Prince John**, for his MS Engineering programme at the Engineering Mechanics Unit, Jawaharlal Nehru Centre for Advanced Scientific Research, Jakkur, Bangalore, India and that it has not been submitted elsewhere for the award of any degree or diploma.

Prof. Umesh V. Waghmare
Dean, Academic Affairs
JNCASR, Jakkur
December 2019

Certificate

I hereby certify that the matter embodied in this MS Research Report entitled **Synchronized PIV-PLIF Experiments on Mixing in Confined Space by a Decelerating, Turbulent, Buoyant Jet** has been carried out by **Mr. Albin Prince John**, for his MS Engineering programme at the Engineering Mechanics Unit, Jawaharlal Nehru Centre for Advanced Scientific Research, Jakkur, Bangalore, India and that it has not been submitted elsewhere for the award of any degree or diploma.

Prof. K.R Sreenivas
Chairman
Engineering Mechanics Unit
JNCASR, Jakkur
December 2019

Acknowledgements

I thank Bhabha Atomic Research Centre and Prof. Meheboob Alam for the experimental facilities provided. The test facility was funded by Bhabha Atomic Research Centre (Mumbai), Government of India under the MOU "Experiments using salt-water/fresh-water test facility for buoyancy induced flow studies", Ref. No:6/15/2014/BARC/R&D-1/2865.

I would like to express my sincere gratitude to Dr. Deepak Madiwal for his patience, continuous support and motivation. His guidance and professionalism have helped me refine my approach to research, explore the topic in detail and write the report. I will be always grateful to him for the time and effort he had taken to clarify my doubts on an hourly basis and reinstalling confidence. I would like to thank the jury of my comprehensive evaluation Prof. Sourabh Suhas Diwan (AE, IISc) for his insightful comments and encouragement, also for the questions he had asked which inspired me to widen my research and perspectives.

My sincere thanks goes to Prof. Umesh V. Waghmare and Prof. Diwakar S. Venkatesan for the report corrections, support and encouragement. I value the efforts of Prof. Diwakar S. Venkatesan in providing us more experimental facilities and improve our research standards. He always had time and energy for helping students. I would also like to thank Prof. Ganesh Subramanian for the long, quality hours he had spent for our coursework to show us the breadth and depth of fluid mechanics. I would be always excited to attend his classes whenever possible. I thank Mr. Bhuvaneswar Gera (BARC) for the inputs he had provided from his CFD work that helped me refine my experimental methods. I express my sincere gratitude to Mr. Brindaban Ghosh and Mr. Sunil Ganju, members of the BARC project evaluation committee for their valuable inputs and appreciation. I thank the NITC alumni at BARC for their support.

I would like to thank Prof. Jaywant .H Arakeri and Prof. Raghuraman .N Govardhan from the Department of Mechanical Engineering, IISc for setting up great examples in doing research with passion. The motivation and support they had provided was very crucial for the successful completion of my degree. I am grateful for the time they had

spent for helping me in times of difficulties, in spite of their busy schedule. The training I had received from the Fluid Mechanics Lab, IISc made me confident to pursue research further. I would like to express my sincere gratitude to my fabricator Mr. Sureshkumar for providing me quality products always before time. I also thank my batch mate Prashant Ramesh for his support and professionalism.

I would like to thank my professors at NIT Calicut and Mr. C.K Pavithran for their motivation and support. I thank the staff at Central Workshop, NIT Calicut for their extra efforts in helping me learn different skills and tools relevant for experimental research. I thank my teams in IISc football league and IISc badminton league for helping me balance research and personal space. I thank my friends Sayuj, Smitha, Sailendra and Asiz for the lively conversations. I thank my NITC seniors Dr. Anil Das, Aswin .N and Dr. Aswathi .N for the live discussions and sharing their experiences that helped me in my research life. I must also thank Arun Kumar, Sushmita Chandra and Murali .M Gopal for the extra efforts they had taken to maintain my career passion.

Finally, I must express my very profound gratitude to my parents Shri. John Varghese and Smt. Saley K.E, my grandmother Smt. O.L Veronica, my brother Noble and to my wife Rashma for providing me with unfailing support and continuous encouragement throughout my years of study and through the process of researching and writing this research report. This accomplishment would not have been possible without them.

Thank you.

.

"Imagination is more important than knowledge."

—**Albert Einstein**

Abstract

Turbulent jets of miscible fluids of different densities are commonly observed in natural and industrial flows. In these type of flows, the difference in densities causes a buoyancy driven convection along with the momentum driven flow. In the case of miscible fluids, the mixing causes variations in density and affects the properties of the jet. Understanding the behaviour of buoyant jet flows and mixing in confined space would help in the design of buildings in improving natural ventilation, especially during fire or gas leakage. Understanding the flow and mixing patterns and enhancing the natural ventilation would help in cases like fire or gas leakage as power shut-down during emergencies would stop forced ventilation.

The present work aims at studying the patterns of flow and mixing through experiments in a confined space with a jet source of unsteady buoyancy flux. The experiments were conducted in simple confinements that replicate a wall or roof opening. Approximately 50 flow visualization experiments were conducted on scaled models of a room with a jet source of buoyancy and flow outlets that resemble windows or roof openings. The air-smoke pair was replaced by water-salt solution pair to scale down the dimensions of the experiment set up. The confinement is located at the near-field of the jet. The results from the project may be used in optimizing the ventilation design to maintain sufficient oxygen levels inside buildings for safe evacuation and prevent suffocation from smoke caused by fire.

The experiments were conducted using synchronized Particle Image Velocimetry (PIV) and Planar Laser Induced Fluorescence (PLIF) techniques to get the high resolution, simultaneous, velocity and concentration fields. The design of the experiment set up, instrumentation, experiment techniques and analysis methods are discussed in the report. Different sets of experiments by varying the flow rate and the position of outlet have been conducted using simultaneous PIV-PLIF technique. A detailed description of velocity and density profiles along the flow are presented.

The experiments helped in extending the studies about decelerating, turbulent jet in confined space. It shows the variation in flow and mixing caused by the near-field

confinement compared to a free jet. While a free jet entrains fluid from the ambient fluid domain and transports it in the axial direction, the confinement in the near field causes steady circulation zones that enhance mixing. Inside the confined space, large variation from stably stratified flows to violent mixing were observed within Reynold number from $1500 - 3700$.

It is observed that in the tests with near-field confinement, the Reynolds number is the key parameter that decides the pattern of flow inside the confinement. The difference in the properties of the fluid at flow exits for side and bottom opening are discussed. The relationship between temporal mean centreline velocity and the axial coordinates is explained. The methods to apply Reynolds averaging for transient flows are also described. Self-similar profiles of velocity and concentration were observed inside the confinement. Reynolds stress and velocity-concentration correlations are described. The increase in mixing caused by the trapped circulation zones due to the confinement is also explained. Design parameters for buildings with a potential jet source of buoyancy can be inferred from the present studies. Possible improvements in the experiment methods for studying specific parameters are also discussed.

Contents

List of Symbols

ρ_s	Density of incoming salt solution
ρ_a	Density of ambient fluid
ψ	Geometric scale factor
$\Delta\rho_o$	Difference in density between incoming salt solution and ambient fluid at time t = 0s ($\Delta\rho_o = \rho_s - \rho_a$)
$\tilde{\rho}$	Instantaneous density with unity-based normalization
μ_s	Dynamic viscosity of incoming salt solution
μ_a	Dynamic viscosity of ambient fluid
D	Diameter of flow inlet
U	Notation for velocity in horizontal direction
V	Notation for velocity in downward direction
$\overline{V}_c$	Mean centreline velocity of jet
V_o	Mean inlet velocity calculated from overall flow rate
V_{av}	Mean downward velocity
$\overline{V}_{av}$	Mean downward velocity normalized by the maximum mean downward velocity in the sub-domain
V_{rms}	Root mean square of velocity fluctuations in the downward direction
$\overline{V}_{rms}$	Root mean square of velocity fluctuations in the downward direction normalised by the maximum mean downward velocity in the sub-domain
$\tilde{X}$	X coordinate in the inlet coordinate system
$\tilde{Y}$	Y coordinate in the inlet coordinate system
h	Elevation head
Δt	Time between laser pulse pair

HS30	High flow rate (1.265lpm), side opening = 30mm, Re = 4000
MS30	Medium flow rate (0.88lpm), side opening = 30mm, Re = 2700
LS30	Low flow rate (0.489lpm), side opening = 30mm, Re = 1500
HB30	High flow rate (1.265lpm), bottom opening = 30mm, Re = 4000
MB30	Medium flow rate (0.88lpm), bottom opening = 30mm, Re = 2700
LB30	Low flow rate (0.489lpm), bottom opening = 30mm, Re = 1500
MCS	Mean Cross Sectional
v_e	Velocity of entrainment
κ	Coefficient of entrainment
ζ	Size of the largest eddies
τ	Time period of rotation of the largest eddies
t_l	Eddy turnover time
u_l	Characteristic velocity of the turbulent flow
χ	Magnitude of a quantity to be measured
ϵ	Random error
σ	Standard deviation of random error
L_1	Laminar length of jet

List of Figures

List of Tables

Chapter 1

Introduction

Transport of fluids generally happen in two ways – Natural Convection and Forced Convection. In Natural convection, transport of fluid is caused by density gradients in an acceleration field, whereas in Forced Convection the fluid transport is caused by an imposed pressure gradient. The density gradient could be due to difference in concentration of a species or temperature or both. The pattern of motion, in a space with gravitational field acting downwards, is upwards for the lighter fluid parcels and downwards for the heavier fluid parcels. The net force that pushes the lighter fluid parcels in a direction opposite to the gravitational field is called the force of Buoyancy.

The force of buoyancy on a fluid parcel is proportional to the difference between densities of the fluid parcel and its surrounding fluid domain. The force of buoyancy occurs in an acceleration field. While a pure jet is a flow completely driven by momentum, a pure plume is a flow completely driven by buoyancy. A buoyant jet flow falls in between these two limits. A buoyant jet is driven by both momentum and buoyancy. Buoyant jets and plumes are commonly observed in atmospheric and oceanic flows. They are the common sources of buoyancy driven convection that needs to be addressed during the design of buildings and structures for better natural ventilation.

1.1 Natural ventilation

Natural Ventilation refers to the exchange of air from a building or chamber to the outer atmosphere, driven by existing pressure differences. Two main classifications in natural ventilation are 1. Wind Driven ventilation and 2. Buoyancy driven ventilation [34]. Wind driven ventilation causes the fluid transport by pressure difference caused by winds. Buoyancy driven ventilation occurs due to gradient in density caused by variations in temperature or concentration or both. Since most of the heat generating objects are kept near floor level in buildings, there will be a dominant motion of hot air from the bottom to the top of the room. Placing openings at ideal locations can cause desirable

changes in the flow and temperature conditions inside the room. The motion of air in and out of buildings and chambers caused by buoyancy is called Stack effect.

During emergencies like a quick fire or a gas leakage, the power would be shut down to avoid short circuit and similar issues. Shut-down of power would stop all means of forced convection that would have helped in flushing the smoke out of the buildings. Wind driven convection cannot be relied upon during such instances or for different geographic locations. Thus it is important to improve the natural ventilation by buoyancy driven convection to reduce the smoke concentration inside the room for quick evacuation and reduction of damage inside the premises. The intensity of buoyancy driven flows increases with the increase in the difference in densities of the fluids, which makes it more useful when there is larger temperature difference between the air inside the room or building and the ambient atmosphere as in the case of a fire. Therefore understanding the ideal geometries for buoyancy driven convection is useful for fire safety.

In buoyancy driven convection from a confined space, the presence of different openings at different vertical positions would allow cold air to enter the confinement through lower openings and flush out hot air through higher openings (displacement ventilation). In the case of confinement with a single opening, a bidirectional flow happens leading to mixing flows inside the confinement (mixing ventilation). In displacement ventilation, if the openings are separated by sufficient vertical distance, stable stratifications happens and a clear separation layer appears at steady state [35].The portion below this neutral layer will have denser fluid and the portion above will have lighter fluid. In the case of buildings, the lower portion of a room will be at a lower pressure compared to the ambient due to this buoyancy driven convection and draws cold air inside while the upper portion will be at a higher pressure compared to the ambient and pushes out the lighter fluid. The pressure at the neutral level will be equal to the pressure of the atmosphere in the absence of winds.

The project aims at studying the evolution of a buoyant jet and pattern of mixing in confinement from an unsteady source of buoyancy. The confinement was restricted to the near-field of the jet thus making it important to analyse the near-field dynamics first, based on which further studies can be made on buoyancy driven exit flows. Since the confinement in the axial direction falls in the near-field of the jet, flow patterns different from cases with confinement in the far-field were expected. The outflow from the confinement was expected to be primarily driven by buoyancy driven flows. Studying the pattern of flow and mixing in buoyancy driven convection from a confined space can help in estimating the time required for the safe evacuation of occupants.

1.2 Motivation

The problem of studying buoyant, confined jet through flow visualization experiments was proposed by Bhabha Atomic Research Centre, Mumbai, for verifying CFD models for natural ventilation from confined space which contains a jet source of buoyancy. Jet in confined space are used for applications including mixing in chemical industries, cooling turbine blades and fuel injection in internal combustion engines. The test cases fall under the category of mixing due to an unsteady, turbulent, buoyant jet in confinement.

Turbulent jet causes transportation of momentum and mixing of species. These flows falls under the category of canonical flows and are extensively studied by researchers from different perspectives, using a variety of tools. The turbulent jet causes transport of momentum in the free-shear layers due to Kelvin-Helmholtz instability and this feature make these flows useful for various industrial purposes like atomic reactor safety, chemical mixing chambers, rocket designs etc. The design of safety systems of atomic reactors are closely related to the effects of density variations of flows inside. Cases like high temperature local fires and gas leakages may be considered as examples. The coupling between velocity of flow and mixing adds complexity to these flow cases. Navier-Stokes equations were used as the governing equations to solve the velocity fields in these cases. Since there are no generic analytical solutions for non-linear PDEs, no analytical solutions were obtained for the above mentioned flow cases. The limitations in computational capabilities make turbulence modelling extremely difficult. Direct numerical solutions currently are not able to resolve the entire spectra of spatial and temporal scales of practical, engineering problems.

Characteristics of turbulent jet and plume are extensively studied, especially in the far-field of the source. But in many real life cases the flow domain would be restricted to the near-field of the jet or plume. Therefore it is important to study about the pattern of flow and mixing in the near-field of a fire or gas leakage in a small room. Previously, many experiments were performed by others using measurement probes to measure flow parameters. The probe-based measurement systems (hot wires, conductivity probes etc) were able to give only the point data which was insufficient to characterize any large flow field. Furthermore these are intrusive methods which can influence the flow field. Therefore, placing probes at every significant location can affect the flow and decrease the signal-to-noise ratio (SNR). CFD methods require high resolution experimental data to refine the turbulent multiphase mixing model.

Therefore it is important to generate an experiments-based database with high resolution, for flows with density gradients so that the flow physics can be explained better

and the present numerical models can also be improved. In this study about natural ventilation from confined space, it was assumed that the concentration gradient, inlet velocity and the confinement geometry are the key factors that decide the flow pattern where concentration gradient and velocity fluctuations are coupled quantities.

Non-intrusive experimental methods that can give information from a large spatial domain is preferred over probe-based measurements. Two-dimensional Particle Image Velocimetry (2D PIV) is a non-intrusive flow velocity measurement method capable of providing velocity data from a cross sectional plane of the flow. A properly set-up PIV system has high SNR. 2D- PIV on a vertical plane can be used to extract the vertical component and one of the horizontal components of flow velocity. The fluid domain needs to be uniformly seeded with small, neutrally buoyant particles, with a cross sectional plane illuminated by a laser beam to record images for calculating the flow velocity from the motion of particles.

Planar Laser Induced Fluorescence (PLIF) is another non-intrusive flow diagnostics method used to measure concentration of flow components from a cross sectional plane illuminated by a laser beam of suitable wavelength. The flow seeded with a fluorescent dye in different concentrations for different components would exhibit fluorescence, at the selected wavelength, with intensities proportional to the concentration from which density values can be calculated.

Since PIV and PLIF are non-intrusive flow diagnostics methods and the outputs from these methods do not affect each other, they can be coupled to form a Synchronized PIV-PLIF flow measurement system that can give simultaneous velocity and concentration fields from a cross sectional plane of flow. This combination method can be useful as velocity and concentration are coupled in buoyancy driven flows of miscible fluids. Synchronized PIV-PLIF data is useful in finding meaningful velocity-concentration correlations as identical flows cannot be reproduced for PIV or PLIF when done separately, because each realization of a turbulent flow would be different. There is a considerable advantage in time also as the total number of experiments can be reduced to half.

Thus the basic problem was identified, experiment techniques and instruments were selected, and the key parameters were considered. Elaborate planning and design of inflow and experimental set up was done. Once the design was finalized, the set up prototype was tested and improved. The instrumentation, data acquisition, verification and processing procedures were refined and verified before starting the final experiments. Literature review was also done in this period and the relevant flow physics domains were identified.

1.3 Literature review

Turbulent jet is a pressure driven flow through an outlet/cavity. Turbulent jet dynamics is an extensively studied topic due to its importance in various scientific and engineering applications. The basic difference between turbulent jet and plume is in the rate of production and dissipation of turbulent kinetic energy. Jet being primarily momentum driven, the mean flow produces turbulent kinetic energy and it is lost in viscous dissipation. The plumes being primarily buoyancy driven, the buoyancy factor 1. increases the mean momentum flux and thus the mean shear production and 2. causes the direct energy transfer from potential to turbulent kinetic. Viscous dissipation being the sole mode of dissipation, the intensity of turbulence at equilibrium levels for a plume would be fairly higher than a jet [36]. The complex flow structure interactions in turbulent jet flows make accurate predictions difficult and therefore multiple aspects of turbulent jet flow continue to be unexplored.

Tollmien [54] had provided one of the first theoretical descriptions of the flow phenomenon based on the mixing-length theory of Prandtl. Three major domains were identified in the flow field of a turbulent jet namely the near-field, the intermediate or transition-field and the far-field. The flow characteristics of the turbulent jet matches the inlet conditions in the near-field. The jet dynamics start to appear in the near-field, undergoes transformation in the transition-field and reaches a self-similar state in the far-field [30, 21]. The jet flow domain can be also divided into a developing portion and a fully developed portion. The developing portion comprises of both the near-field and the intermediate-field. The developed portion comprises of the far-field. The flow dynamics in the developing portion is important in many practical applications of a jet flow where the inlet conditions can affect the heat, mass and momentum transfer.

It is observed that the momentum fields of both buoyant and same density jets have a significant relation with the Reynolds number [17]. As in the case of a buoyant jet, when a jet enters a medium of lighter fluid with gravity in the direction of the flow, the velocity at the inlet is higher than the case of a jet entering a medium of same fluid. At the beginning of the jet flow from the orifice, an unstable laminar shear layer is produced by the flow. The sudden growth of this shear layers initiates turbulence and creates ring vortices. These vortices creates further mixing of the jet fluid with the ambient fluid [12]. These vortices induce motion in the fluid and these motions influence other vortices in its field of influence which results in the pairing off of adjacent vortices [22, 56]. It is also identified that the important reason for initial dilution of the jet is the production of these vortices [36].

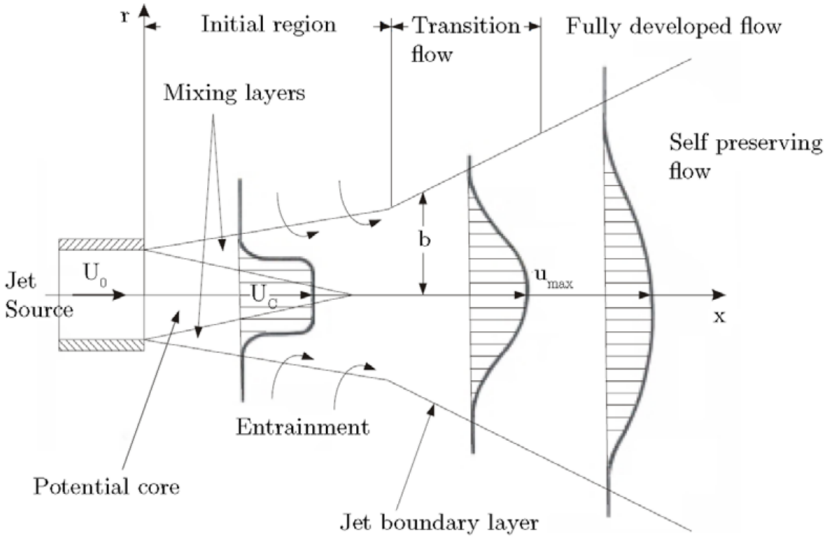

Figure 1.1: Schematic diagram of a free turbulent round jet (image courtesy: Ruud Weersink [48])

McNaughton and Sinclair [38] had identified a semi-turbulent region of jet near the inlet before the jet becomes fully turbulent. This region, known as the "laminar length" has a length which depends on the inlet Reynolds number.

The large gradient in velocity in the lateral direction of the turbulent jet causes the formation of large eddies from the pairing-up of vortex cores at the shear layers, which later cascades down to smaller scales. It should be noted that for higher thickness of the initial shear layer, the vortex formation is weaker [2].

George and Davidson [25] had observed that the mean velocity profiles when normalized with appropriate velocity and length scales collapse to a single curve, in the case of simple, free shear flows. Even though they had stated that *"One of the most persistent ideas of turbulence research is that turbulence forgets its initial conditions"*, they had added that the collapse of data does not necessarily convey that the flow is independent from the initial conditions but on the dependence of normalizing scales with the streamwise dimension, which varies with experiments. Reungoat *et al.* [44] states that the axial velocity profiles of the jet become self-similar in the fully turbulent region.

Turbulent jets are expected to show self-similar velocity profiles from an axial distance of $5D$ from the inlet. There will be both large and small scale structures associated with the jet. The large scale structures were predominant till an axial distance of $10D$ according to the works of Dimotakis [16]. The region outside an axial distance of $10D$ is considered as the self-similar far-field domain of the turbulent jet.

For a non-buoyant jet, the jet is laminar for $Re < 30$ (dissipated laminar jet), the jet has a "laminar length" and becomes turbulent downstream for $Re > 500$ and the jet becomes turbulent from the near-field and spreads at a constant rate for $Re > 2000$ [33]. The laminar length is smaller for higher Reynolds numbers. With the decrease in Reynolds number, the centreline velocity also decreases. The rate of radial spread of a circular jet decreases continuously with Reynolds number [43]. The studies of Ricou and Spalding [45] showed that the entrainment by a turbulent jet becomes constant after Reynolds number increases above 20000.

The continuous entrainment caused by the turbulent buoyant jet adds more mass into the flow and gain momentum in the downstream flow [36]. There would be a reduction in the axial velocity and core concentration of the jet due to entrainment from the surroundings. Boundary conditions like presence of lateral enclosures, walls and the characteristics of the surrounding fluid domain such as large-scale motions and background turbulence, decide the further development of the jet downstream.

The pattern of mixing in the near-field of buoyant jet or non-buoyant jet is extremely complex [5]. Dimotakis [16] divides mixing into three categories - Level 1, 2 and 3. In Level-1 mixing, mixing is passive and does not affect the flow dynamics. In Level-2, mixing influences the flow dynamics but not effectively control it. In Level-3, mixing causes changes to the fluid properties like concentration, density or change in enthalpy or pressure. Buoyancy driven flows of miscible fluids falls in Level-2 and Level-3.

There can be two types of mixing pairs due to a miscible, buoyant jet in fluid - lighter jet being injected to a heavier fluid and a heavier jet injected to a lighter fluid. The mixing due to a lighter jet from the floor, in a heavier medium was observed to be higher than the mixing due to a heavier jet from the floor, in a lighter medium as the buoyancy favours deeper penetration into the medium. The deceleration in the axial direction observed in a lighter jet injected to a heavy fluid is greater than the deceleration in the axial direction observed in a heavier jet injected to a light fluid. The higher momentum of the heavier jet also favours lesser deceleration [51]. Therefore while using salt-bath technique for modelling smoke-air pair caused by fire from the floor of a room, the heavier jet must be injected from the top in salt-bath so as to replicate the mixing pattern caused by buoyancy. Certain studies of Gartrell shows that most of the turbulent mixing will stop once the jet start spreading sideways after reaching the neutral stability layers within the density stratified domain [23].

The presence of buoyancy can significantly influence the mass transportation in the flow. It can cause overestimation of thermal stratification in the present turbulent momentum flux models. It also leads to underestimation of turbulent mixing in these models

[42]. The sub-grid scale models that assume local isotropy can fail to deliver consistent solutions. The available literature about the behaviour of jet turbulence when the jet enters a density stratified environment. There are chances that the buoyancy acts against the turbulent kinetic energy and breaks the self-similarity pattern [36].

Anisotropy in Turbulence arises when the time scale of straining motion is significantly different from the time scale for return to isotropy. Structural anisotropy occurs in turbulent flows due to the mean flow gradient if present. The large eddies would be stretched and oriented by the mean flow gradient. Since the large eddies contain most of the energy, the mean flow causes anisotropy in the velocity fluctuations by increasing the velocity fluctuations in certain directions and decreasing in the other directions. The spectrum of length and time scales of fluctuations were centred on the local large-scale length and time of flow [13]. Most of these ideas from momentum-driven turbulent jet can also be applied to buoyant turbulent jet [40], [41].

The complexity of the flow case demands high resolution, non-intrusive data recording methods. Resolving directional ambiguity using the conventional flow measurement method of hot wire is nearly impossible as it underestimates fluctuations in velocity and over estimates the mean velocity of the flow [36]. In the case of a fire, higher temperature at the source would make the smoke lighter and enhances mixing thereby reducing the evacuation time window.

1.4 Flow description

In natural convection caused by a temperature gradient, the lighter fluid moves upwards, mixes with the ambient fluid, becomes heavier and settles down, leading to a steady state after some time. Similar pattern is observed in the case of natural convection caused by concentration gradient also, leading to stratification. If there is a steady source of buoyancy, there will be a continuous change of concentration inside the confinement, either increase or decrease depending on the type of source, throughout the duration of the flow.

Natural convection problems of large physical dimensions like fire or gas leakage in a building are difficult to perform in typical laboratory conditions. It would be convenient if the experimental set up can be scaled down to fit laboratory conditions. The flow dynamics depends mainly on the inlet Reynolds number for jet flows inside confinement, which means flows happening in different physical dimensions with the same Reynolds number are similar.

In the case of natural ventilation in buildings, the flow of air-smoke pair in a room can be replaced with flow in a scaled experimental set up with same Reynolds number, using water-salt solution pair (salt-bath technique). Salt-bath technique is found to have good agreement with mathematical models in ventilation flows [35]. The salt-bath technique provides the required difference in density but does not consider the effects of thermal radiation and diffusion. The The higher density of water compared to air will help in scaling the experimental set-up to laboratory conditions. The flow configuration can be even inverted as Boussinesq flows appear similar when viewed upside-down when the fluids are interchanged.

Equating the mass flux of air in a building to a scaled set up with water, where ψ is the geometric scale factor

$$\rho_a Vol_a = \rho_w Vol_w = \rho_w Vol_a \psi^3 \tag{1.1}$$

$$\psi = (\frac{\rho_a}{\rho_w})^{1/3} = 0.106. \tag{1.2}$$

where ρ_a is the density of air, Vol_a is the volume of the room, ρ_w is the density of water and Vol_w is the volume of the scaled confinement.

When a fluid in motion enters a quiescent body of the same fluid, a velocity shear is created between the entering and ambient fluids, causing the formation of eddies that lead to turbulence and mixing. Since the pattern of a turbulent flow largely depends on the geometry of the flow domain and on the type of forces acting on the fluid, there can be a wide variety of flow conditions where each case require specific investigation.

Analogous to the case of a fire happening in a room with roof or wall openings, experiments need to be done on confined space where a lighter fluid enters a heavier fluid domain, mixes and flows out through the flow exits. Starting from a simple case, the source of constant buoyancy can be modelled as a plume or buoyant jet fed from a constant flow rate source. Experiments with buoyant jet help in understanding the pattern of mixing in confinement due to turbulence.

The room or building in the problem can be experimentally modelled as a box of scaled dimensions. Two important parts of the problem are 1.The flow characteristics of the incoming buoyant jet and the pattern of mixing and 2.The buoyancy driven convection from the confinement to the ambient through the flow exits. The buoyancy driven convection is slower than the flow caused by the buoyant jet. The study primarily focusses on the flow pattern of a buoyant jet in confinement.

1.4.1 Boussinesq approximation

In a system of incompressible fluids with small density difference, the non-linearity of the Navier-Stokes equations can be removed if variations in density are neglected in the inertial terms and continuity equation. But even small variations in density can influence buoyancy because of gravity. Therefore the actual density is retained with the buoyancy term in the equation of motion in the vertical direction. This approach is called Boussinesq Approximation.

Navier-Stokes equation

$$\rho[\frac{\partial(u_j)}{\partial t} + \frac{\partial[u_i u_j]}{\partial x_j}] = -\frac{\partial p}{\partial x_j} + \frac{\partial \tau_{ij}}{\partial x_i} + \rho f_j \tag{1.3}$$

Hydrostatic balance

$$\frac{\mathrm{d}\bar{p}}{\mathrm{d}x_j} = \bar{\rho} g_j; \quad g_j = f_j \tag{1.4}$$

Expanding the Navier-Stokes equation considering the density variation,

$$(\bar{\rho} + \rho')\frac{\partial[u_i u_j]}{\partial x_j} = -\frac{\partial p'}{\partial x_j} + [-\frac{\partial \bar{p}}{\partial x_j} + \bar{\rho} g_j] + \rho' g_j + \frac{\partial \tau_{ij}}{\partial x_i} \tag{1.5}$$

Physically the approximation means that the flow field is not affected by the small variations in density except that they give rise to buoyancy forces. The approximation is valid when the dimensionless density difference $\Delta\rho/\rho$ is less than unity. Thus the modified equations of motion becomes

$$\bar{\rho}\frac{\partial[u_i u_j]}{\partial x_j} = -\frac{\partial p'}{\partial x_j} + \rho' g_j + \frac{\partial \tau_{ij}}{\partial x_i} \tag{1.6}$$

The magnitude of buoyancy force is the weight of the fluid displaced.

1.4.2 Diffusion

Diffusion is the net transport of species due to a gradient in concentration, from higher concentration to lower concentration. In fluid flow and mixing, two types of diffusion are present: molecular and turbulent diffusions. Molecular diffusion involves motion of molecules and hence is a slow process compared to turbulent diffusion. Turbulent diffusion on the other hand refers to the transport of mass, energy or momentum by turbulent motions. Turbulent diffusion is a quicker process than molecular diffusion and thus plays a huge role in environmental flows and mixing. Unlike laminar flows, turbulent flows comprise of eddies with wide range of length scales. The spread of contaminants in the flow will be affected by these eddies.

The eddies smaller than the fluid parcel distort the parcel causing sharp gradients in concentration and the eddies larger than the parcel transport the whole parcel with less mixing. The sharp gradients in concentration due the parcel distortions will be smoothened by molecular diffusion. Therefore turbulent diffusion plays a vital role in large scale mixing processes. In the case of a fire or a gas leakage in a room, turbulent diffusion mixes these contaminants in the room which reduces the oxygen content in the room and the time window for evacuation.

1.4.3 Flow parameters

Inlet Reynolds number (Re) : Reynolds number at the inlet is used to classify various jet flow cases. The diameter of the inlet nozzle is taken as the characteristic length scale of the jet flow and the velocity from average flow rate is taken as the characteristic velocity of the flow to calculate Re.

$$Re = \frac{\rho V_o D}{\mu} \tag{1.7}$$

where ρ is the density of the fluid, V_o is the mean velocity of the flow at inlet, D is the diameter of the inlet and μ is the dynamic viscosity of the fluid.

Size of test volume: The experiments were conducted to study the case of a room with a local fire. The buoyancy flux (strength of buoyancy) was taken as the basis of scaling. The average source temperature of fire was taken as 1000^oC and the ambient was assumed to be at 20^oC. Equating the buoyancy flux of real scenario and scaled case with a uniform scaling factor, z,

$$z = [(\frac{\Delta\rho}{\rho})_{air}.(\frac{\rho}{\Delta\rho})_{water}]^{1/3} \tag{1.8}$$

where ρ denotes the reference density of the fluid and $\Delta\rho$ denotes the difference in density of the incoming fluid from the reference density.

Time scale for averaging: Turbulent flows happen over a wide range of length and time scales. The largest length scales (size of eddies) may go upto the size of the physical constraints. These large scale (L) eddies are responsible for the bulk transport of the species concentration in the experiments conducted. The size of smaller scales are dependent on viscosity. In the experiments conducted, the mixing caused by the large eddies were greater than the mixing in small scales. The time scale associated with eddies of size l can be estimated as

$$Eddy\ turnover\ time, t_l \approx \frac{l}{U_l} \tag{1.9}$$

where l is the diameter of the eddy and U_l is the characteristic velocity of the eddy (rms velocity). The transfer of energy from larger to smaller length scales also happen at this time scale. The mixing becomes complete with the diffusion in the smaller length scales. Diffusion effectively acts over a scalar field at the smaller length scales and homogenizes the scalar field. The smallest length scale of the scalar field at which the homogenization happens is smaller than Kolmogorov scales, it is called Batchelor's scale, or Obukov-Corrsin scale. The mixing also depends on the difference in scales between the smallest and Kolmogorov length scales which in turn depends on the kinematic viscosity and molecular diffusivity [52].

1.4.4 Entrainment

When a turbulent jet enters a fluid medium, the sharp velocity gradients due to the relative motion between the layers cause flow instabilities at the flow boundaries. This instabilities lead to mixing of the jet fluid with the ambient fluid. This phenomenon is known as turbulent entrainment. The strength of turbulent entrainment depends on the relative velocity between the flow and surrounding fluid.

Taylor's entrainment relationship postulates that the mean inflow velocity across the boundary [39] of a free turbulent shear flow is proportional to a characteristic velocity of the flow, generally taken as the time-averaged maximum mean centreline velocity ($\hat{V}_{av}$). Entrainment causes vigorous mixing and the jet flow gets diluted along the axial dimension. As mentioned above, this entrainment velocity (V_x) was assumed to be proportional to the mean centreline velocity (V_y) and it can be denoted as

$$V_x = \alpha V_y \tag{1.10}$$

where α is the coefficient of entrainment. The rate of entrainment into the plume is proportional to the local velocity [39]. The entrainment coefficient varies with the local Richardson number [31]. Entrainment coefficient is approximately about 0.08 for a vertical jet and 0.12 for a vertical, buoyant plume. Larger value of the entrainment coefficient corresponds to higher mixing of the ambient fluid with the jet. Even though laminar and turbulent jets cause entrainment, the entrainment mechanism is different for both. Entrainment in a laminar jet happens due to diffusion of vorticity.

1.5 Outline of the research report

The study attempts to explore the topic of fire safety and gas leakages in confined space through experiments on scaled models. Experiment methods were devised for the study and the tools were optimized. The experiments study basic room geometries. Focus was made on identifying key parameters that decide the overall flow dynamics. The details about the experiment set-up, instruments and materials, procedures, selection of parameters, calibrations, methods used in measurements, types of experiments and corrections applied are discussed in Chapter 2. Chapter 3 discusses about the flow dynamics. The types of analysis, trends in jet velocities etc are described in this section. The section compares the flow patterns in side and bottom opening configurations. Chapter 4 presents the detailed analysis of entrainment and mixing in different experiments. Analysis, conclusion and future works are discussed in Chapter 5. Information about previous works in the sub topics is provided in each chapter also. The present study discusses about turbulent jet cases only and therefore the term 'jet' means turbulent jet unless otherwise specified and Reynolds number means inlet Reynolds number.

Chapter 2

Experiments

2.1 Motivation and design

The design of the experiment set up was based on the realistic fire conditions in both household and industrial environments. While households have rooms with smaller height (Y) and smaller sized fire sources (D), the industries have comparatively taller rooms (Y) with larger, stronger sources of fire or gas leakages (D). In either cases, compared to the size of the fire source, most of the flow domain would be in the near-field of the turbulent jet ($0 \leq Y/D \leq 15$). Therefore it is important to study the flow and mixing pattern associated with turbulent jet flows in a confinement located at the near-field of the jet.

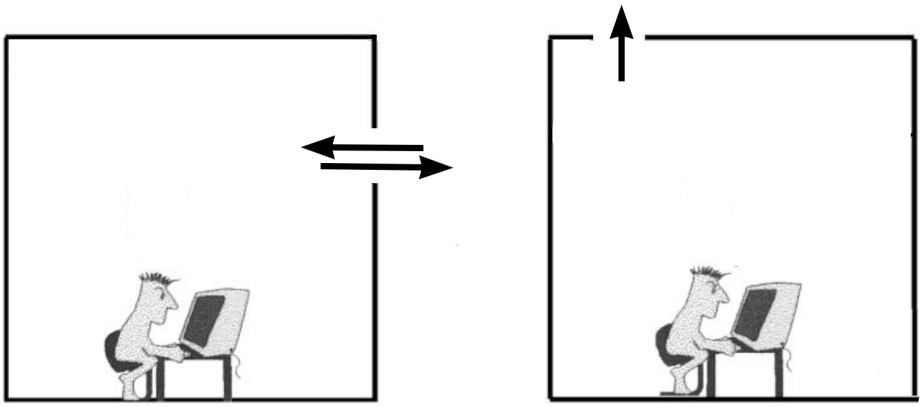

Figure 2.1: Schematic of wall and roof opening (image courtesy: P.F Linden [34])

Salt-bath method method was selected to bring down the physical dimensions of the experiment set up to laboratory conditions. Unlike the case of air, salt-bath method require flow outlets along with sources/flow inlets owing to the incompressibility of the fluid. Two simple cases of flow outlets used in building architecture were selected for the experiment cases namely 1. wall opening and 2. floor opening. For simplicity, the outlets were required to be placed away from the jet axis to reduce the direct interference with the jet flow regime. They also need to be placed away from the walls for the same reason.

In order to replicate the upward flow of smoke aided by buoyancy with a denser jet, the jet flow had to be inverted in salt-bath method. The confinement had to be placed in a fluid domain of larger size with the same ambient fluid to replicate the atmosphere and interaction through the opening on the confinement.

Trial experiments using dye visualisation were conducted to refine the design of the experimental set up. These tests had ensured that the dimensions of the set up would allow the experiments to run for sufficient time to obtain meaningful data. They also ensured/verified sufficient laser illumination, PIV particle concentration, photo-stability of the dye, position of cameras, laser and optics, standard operating procedures for running experiment consistently, laser and chemical safety and various calibrations.

2.2 Experimental set-up

The study of buoyant jet in confined space to understand local fires and gas leakages, was conducted in an inverted model with salt solution-water fluid pair replacing smoke-air fluid pair, with denser, salt solution as the incoming fluid. The test set up consists of a larger, rectangular cuboid shaped glass tank filled with water, which resembles the ambient atmosphere and a smaller, square cuboid shaped acrylic box with openings, immersed in the large tank and filled with water, that replicates a room. Since the heavier salt solution was selected as the incoming fluid that enters the confinement from the top, the square cuboid shaped small box was suspended from the top with its top surface $3cm$ below the free surface of water inside the large tank (Fig. 2.2) with its horizontal walls parallel to the free surface of water in the large tank.

The inside dimensions of the large tank are $36.5cm$ x $40.7cm$ x $61.5cm$. It has an open top and provisions to suspend the small box. The small box has inner dimensions $14cm$ x $14cm$ x $21.2cm$ and has openings at different locations. The volume of the small box is approximately 4.2 litres. The salt solution would be injected from an $8mm$ circular inlet at the top rectangular surface of the small box.

Two types of small boxes were fabricated for the experiments based on the geometry of the flow exit - one with a $30mm$ circular opening on the centroid of the square side wall away from the inlet and another one with a $30mm$ circular opening on the rectangular bottom surface (Fig. 2.5), along the longest centreline, placed evenly between the centroid and the edge away from inlet. Comparing the inlet diameter with the jet axial length scale, it can be observed that the confinement in the axial direction is located at $17D$ from the inlet and it restricts the jet flow within the near-field (D is the inlet diameter).

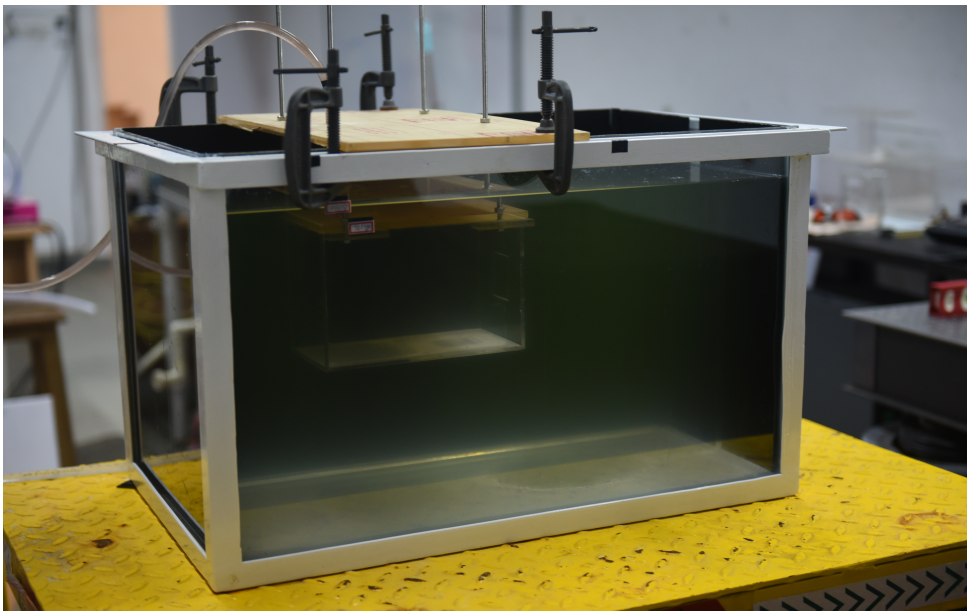

Figure 2.2: Photograph of the Experimental Set up. The rectangular cuboid shaped large tank and the square cuboid shaped small tank suspended from the top are shown. The large tank is mounted on a height adjustable platform aligned with the laser sheet. All faces of the large tank except the ones for laser and image capturing are covered by opaque, non-reflecting coatings.

Trial experiments were conducted on the test set up to understand the flow pattern and synchronize the instruments. After running multiple flow visualization experiments, salt solution with a density difference of $5kg/m^3$ from water was selected as the incoming fluid for all experiments based on the Boussinesq approximation and the window of recording of the transient flow. The salt solution was fed from a constant flow rate source. Experiments were conducted at a room temperature of 20^oC. The large tank was filled with 72 litres of water. The fluids were then prepared for PIV and PLIF which will be explained in subsequent sections. The salt solution was stored in an overhead tank which is connected to the small box suspended inside the large tank through a flexible pipe without air bubbles.

The salt solution was made to flow from an overhead tank placed at a constant height to the small box through the inlet at the top of the small box and allowed to interact with ambient fluid in the large tank through the side or bottom wall openings of the small box. The experiments were conducted for three cases of inlet flow based on inlet Reynolds number – (i) $Re = 1500$, (ii) $Re = 2600$ and (iii) $Re = 3700$. The inlet Reynolds number was changed by adjusting the flow rate from the overhead tank.

The salt solution comes from a single homogeneous source with constant density placed at a fixed height. There would be a decrease in the incoming mass flux due to the reduction in 1. density difference due to mixing and 2. net elevation head when the

water level rises in the large tank.

Figure 2.3: Small box with the frame used to suspend it inside the large tank

2.2.1 Openings in the cuboidal confinement

Position of the opening in the small box to the ambient plays an important role in the type of fluid interactions. There are two configurations used in the small box - bottom wall openings and side wall openings. Different types of flow patterns were observed for bottom wall and side wall openings for cases where the axial confinement was kept at the far-field of the jet (axial distance $y > 40D$ where D is the inlet diameter). Since the experiments conducted in this project work have confinement in the axial direction (near-field) ($y < 17D$), deviation from stable stratification patterns observed in a far-field confinement could be expected.

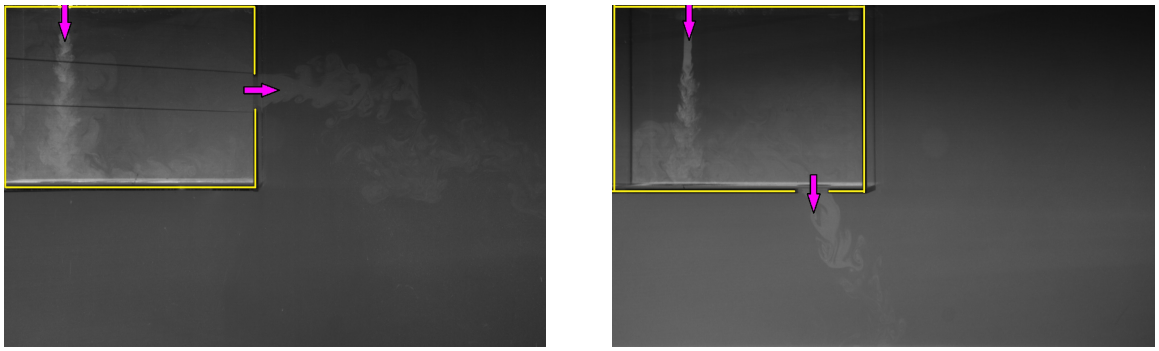

(a) Box with side opening

(b) Box with bottom opening

Figure 2.4: Positions of flow inlet and exit used in the experiments. The figure represents the region of interest and the inner box is represented by yellow lines. The flow inlet and outlet are denoted by arrows. The image covers a physical area of size 480mm x 280mm

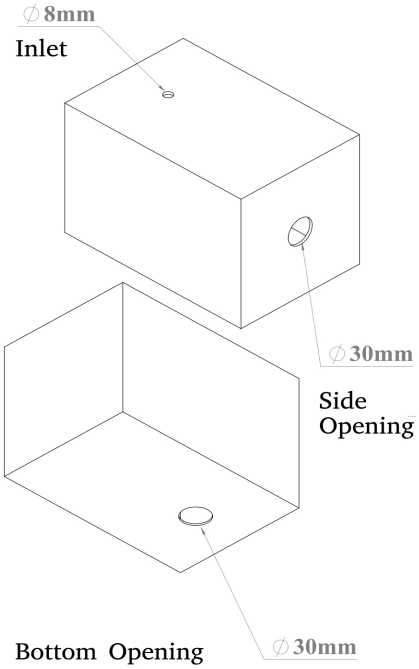

Figure 2.5: Position and dimensions of small box openings - One box has a side opening of 30mm diameter whereas the second one has a bottom opening of 30mm diameter. The openings on walls are centred at the centreline along the longest dimension of the walls. The inlet and bottom outlet are placed at 25% of the length near to the vertical wall so that they are equally spaced from the central plane and side wall

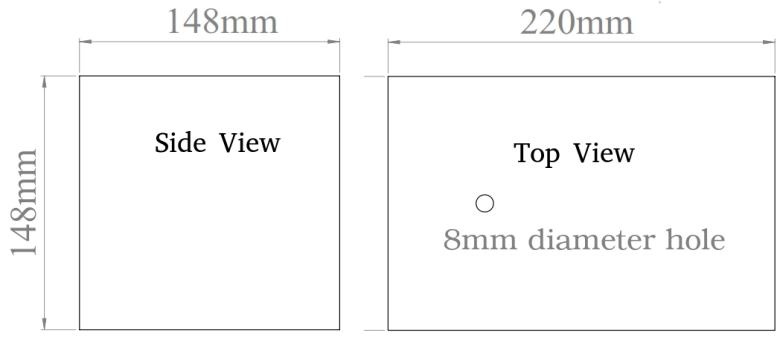

Figure 2.6: Dimensions of the small box

2.3 Particle Image Velocimetry (PIV)

2.3.1 Principle and components

Particle Image Velocimetry (PIV) is a optical flow diagnosis technique to obtain the velocity field of a flow. The flow was seeded with micro particles and illuminated by a laser. The seeding particles move with the flow and scatter the light from the laser. The photographs of their motion can be used to extract the $2D$ flow velocity field . $2D$ PIV was used in the experiments where a plane in the flow is illuminated by a pulse laser and images were captured. Images were recorded as pairs at $10Hz$ frequency and analysed to obtain velocity vectors. Considering the total flow picture, there is a time scale (t_{p1}) below which the suspended particles move only a negligible distance.

The suspended particles were assumed to follow the instantaneous, straight line, in plane, flow packet velocity above this time scale till the next time scale t_{p2}. Above t_{p2}, the particles starts moving in 3D space and moves out of the illuminated plane. Image pairs taken within these time scales will show the displacement of fluid packet through particle tracking. Large time scales also cause large scale motions that affect the post processing of PIV data.

PIV requires a high intensity light source like a pulse laser, suitable lenses to make a sheet of light of thickness approximately $1mm$, neutrally buoyant particles of appropriate size, uniform seeding, refractive index matching, cameras synchronized with laser pulses and a post processing program. The scattering caused by the seeding particles fall under Mie scattering since size of the particles are comparable to the wavelength of laser.

2.3.2 Post processing

The captured digital images are divided into interrogation windows. The size of these windows could be minimized up to a level where they contain at least four seeding particles per window. Within an image pair, each window was compared with the adjacent windows in the next image to find the displacement of the seeding particles. The interrogation window from first image will be overlapped at a specific percentage in the neighbourhood of the corresponding window of the second image in the image pair to identify the displacement. An image cross correlation is used to find the best match in shift of windows among image pairs. The net displacement, taken as an average of vectors in an interrogation window, is divided by the time period between image pairs to get the average velocity of the fluid packet in the interrogation window.

When an image pair is fed into the code, it outputs a velocity field of fluid parcels

where its size depends on the size and overlap of interrogation windows. Thus, there is a reduction of resolution between the image and the output vector field. In the experiments conducted, interrogation window size of 16x16 pixels and an overlap of 50% was selected to obtain best results. The smallest window size with the required number of particles and an overlap area that completely covers the net displacement is preferred. Dantec Dynamic Studio was used to analyse the PIV data.

2.3.3 Errors in measurement

At the edges of images or at walls, there are no interrogation windows on one side which cause errors in the calculation. Outlier detector code was used to detect error vectors and remove them. Non-uniform seeding and out-of-plane motions create errors with the velocity vectors. The PIV system cannot capture the instantaneous velocity field of the flow. Instead it gives an average velocity vector from each interrogation window . Refractive index matching between the two fluids is also important for capturing clear images. PIV signals are prone to errors from uncertainties due to the drag on seeding particles, processing of vectors and SNR [50]. All these effects combine to bring a net uncertainity of less than 5% in the velocity fields obtained from PIV measurements.

For any measurable quantity χ, the measured value would deviate from the true value by a small quantity. The measured values can be expressed as the sum of actual value and error.

$$\chi_{measured} = \chi_{true} + Error \tag{2.1}$$

$$Error = systematic\ error + random\ error \tag{2.2}$$

The systematic error is difficult to quantify but is a constant for the system. The random error (ϵ) fluctuates continuously, following a normal distribution around a zero mean and standard deviation σ. PIV and PLIF has high SNR and they can be considered almost bias free. Errors on the horizontal displacement U and vertical displacement V are independent and both are normal distributed with zero mean and identical standard deviations $\sigma_u = \sigma_v$. The system has 95% confidence that the measured U or V displacement or velocity deviates at most 1.96σ from the true value [15].

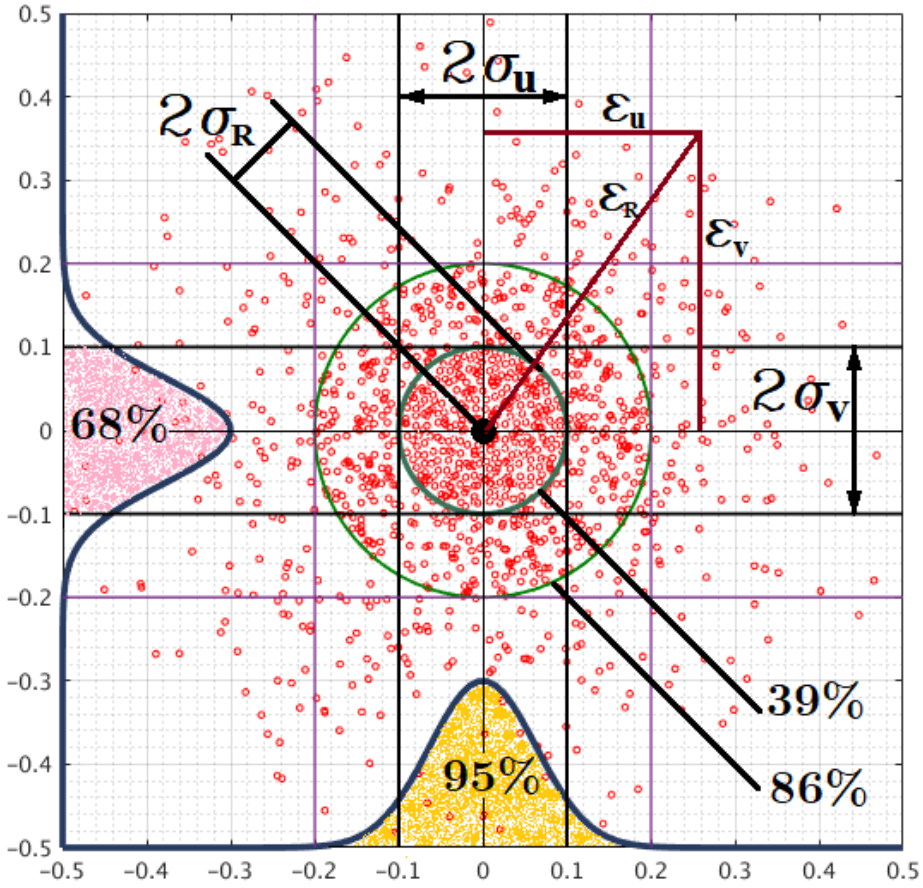

Figure 2.7: The pattern of the error distribution. Each of the small red circles represent the error of a specific vector with signed errors ϵ_u and ϵ_v on the displacement components and positive radial error ϵ_r.

2.4 Planar Laser Induced Fluorescence (PLIF)

2.4.1 Principle and components

Planar Laser Induced Fluorescence (PLIF) is an optical flow diagnosis technique to obtain the concentration field at a plane of flow by recording and analysing high speed images of an illuminated plane in a flow, seeded with a fluorescent dye, which was excited by the pulse laser. Rhodamine 6G fluorescent dye was selected because of its high stability against photo-bleaching and consistent fluorescent spectrum. The concentration of the dye needs to be low so as to obtain linear relation between fluorescence and concentration.

Initially the ambient fluid domain would be seeded with lower quantity of dye so as to provide a background illumination. The incoming fluid had a higher concentration of

the dye so as to appear different from the ambient fluid domain. The fluorescent dye would absorb the light energy, and after a short time period, in the order of nanoseconds, release the light energy at a wavelength higher than the excitation wavelength.

The pattern of mixing and concentration of components can be observed from the variation of intensity of fluorescence from the dye solution. Fluorescence needs to be separated from the laser light while recording. Suitable optical filters were attached with the cameras to avoid laser illumination. To calibrate the light signal during the flow, two extra data sets were recorded to find the equation of the linear relation between intensity and concentration.

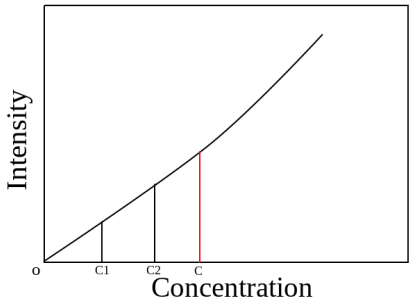

Figure 2.8: The pattern of fluorescence intensity exhibited by $R6G$ dye at weak concentration. The zero concentration point and a known concentration ($C1$) is used to get the unknown concentration value ($C2$) within the linear intensity-concentration limit C.

The images were captured from two known concentrations, preferably from a zero concentration time instance (no fluorescent dye mixed) and the background concentration of the ambient flow domain. The high intensity from the pulse laser improves the signal to noise ratio and the short pulse duration improves the temporal resolution. PLIF can be run in synchronization with PIV as these methods do not interfere each others signal.

2.4.2 Post processing

A lower limit and upper limit for the concentration of fluorescent dye were selected and then the fluorescence intensity values were calibrated. Since the intensity of fluorescence follows a linear pattern within this concentration limit, the variations in concentration within this limit can be calculated. 12bit images are captured for PLIF compared to 8bit for PIV so as to get 2^{12} levels of intensity. The intensity values are then converted to concentration. Digital filters were used to reduce noise and improve the signal quality. Unlike PIV there is no reduction in resolution for the output from PLIF post processing.

2.4.3 Errors in measurement

Refractive index matching is crucial for the success of PLIF. Mismatches in refractive index leads to formation of bands and affects the intensity levels. Concentration of dye

must be low enough to be in the linear range. Calibration of laser beam is required to improve the results. The primary error comes from the camera sensor but since the PLIF system has high SNR, the magnitude of signal is considerably higher than the magnitudes of error. The PLIF calibration based on known concentration also ensures the reliability of the data. The details of calibrations are discussed in further sections.

2.5 Instruments

2.5.1 Laser and associated optics

The intensity of illumination is an important factor in deciding the quality of acquired signal in PIV and PLIF. Pulse lasers have higher intensity than continuous wave lasers and are ideal for PIV and PLIF. Pulse lasers use a technique called Q-switching to generate high intensity short duration pulses of peak power in megawatts which is significantly higher than a beam produced by the same laser in a continuous wave mode. A frequency doubled, Nd-YAG pulsed laser ($\lambda = 532nm$) with an output of $200mJ/pulse$ was used to illuminate a plane in the flow in all experiments.

A combination of spherical and cylindrical lenses were used to make the laser sheet of approximately $1mm$ thickness. The peak intensity of the laser beam follows a Gaussian distribution with respect to time. Rhodamine 6G was selected for PLIF experiments as it exhibits fluorescence of $566nm$ at an absorption wavelength of $532nm$.

Dye visualization experiments were conducted for laser calibration and locations were identified on the illuminated plane of the ambient fluid where the fluorescent dye concentration is negligible throughout the duration of the experiment. Since fluorescence in the experiments is caused only due to the presence of the fluorescent dye, these areas were used to set a reference intensity to analyse the variation of laser beam intensity with respect to time.

The laser was used to fire pulse pairs at a frequency of $10Hz$. The $532nm$ light from the laser was scattered by the PIV particles whereas the fluorescent dye used for PLIF absorbs it and exhibits fluorescence at $566nm$ thus providing output in two different bands of wavelength. Since the intensity of light from the pulse laser ($\approx 10^8 W$)is higher than the possible noise levels from scattering and camera sensors, PIV and PLIF methods have high Signal-to-noise ratio and provide high resolution data.

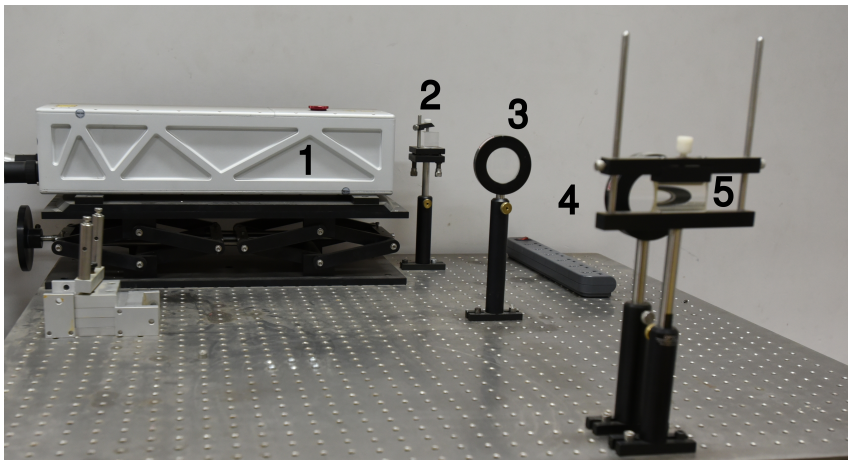

Figure 2.9: Pulse laser and optics used for generating laser sheet. 1. Laser, 2. Triangular prism, 3. Diverging lens, 4. Converging lens, 5. Cylindrical lens. The laser beam from the source was deflected 90^o horizontally by a prism, sent through a pair of diverging-converging lenses and finally converted into a triangular sheet by a cylindrical lens.

2.5.2 Cameras, lenses and filters

Two identical Phantom Speedsense 9040 CMOS high speed cameras were used for capturing images - one for PIV, with a $550nm$ low-pass optical filter to record images in scattered light and another for PLIF, with a $550nm$ high-pass filter to record images in fluorescence light. Thus the PIV particles would not appear in PLIF images and the PLIF dye would not over-illuminate the particles. Nikkor 17-35mm lenses at F2.8 aperture were used on both cameras for capturing the images. The walls of the large tank in the background were covered to avoid stray reflections. The position and alignment of the laser, lenses, tanks and camera were verified before each experiment.

A calibration plate with a printed grid was used to correct the distortions in captured images. The concentration of dye and the concentration of PIV seeding particle were verified to provide quality signal output. The aperture of camera lenses, the position of lenses for laser beam were adjusted to optimize the signal quality. The PIV images were stored as 8 bit images and PLIF images as 12 bit images. Therefore the duration of one set of continuous readings depend on the maximum number of 12 bit (PLIF) images that can be stored in one of the two identical cameras.

The cameras have storage space for 512 image pairs of 12 bit format. With a laser pulse pair firing frequency of $10Hz$, one set of continuous readings can last upto 51 seconds. Based on these factors, one set of continuous image recording time was restricted to $50s$ at a pulse pair firing frequency of $10Hz$. The time gap between two sets of continuous image recording (4 mins) was decided based on the data transfer speed between cameras and the data acquisition computer.

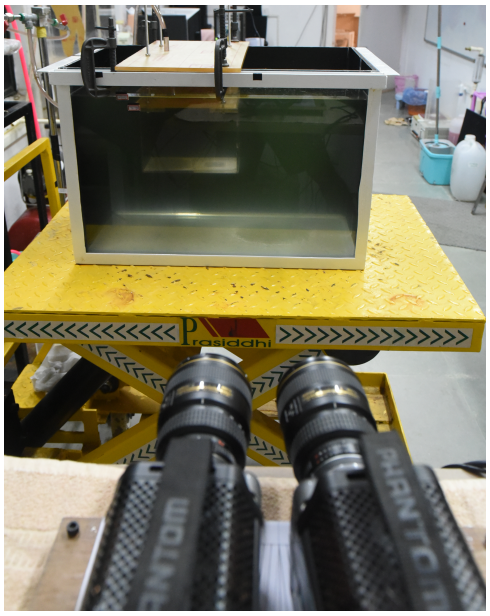

Figure 2.10: Position of cameras. Left : PIV Camera. Right: PLIF Camera

2.5.3 Synchronization

The cameras and laser were synchronized using a National Instruments NI-PCI 6602 timer board. Dantec Dynamics DynamicStudio 5.1 software was used to manage the data acquisition and process the PIV data. Synchronization of cameras with laser was verified separately for PIV and PLIF and then both cameras were synchronized with the laser so as to get simultaneous velocity and concentration data. The PLIF camera also captured image pairs like the PIV camera but only the first image from each pair was taken for PLIF data processing. The synchronization of laser and cameras were verified by emitting laser pulses at a narrow time window and recording the images with the cameras . The data transfer time for synchronized experiments were checked for consistency to finalize the experiment procedure.

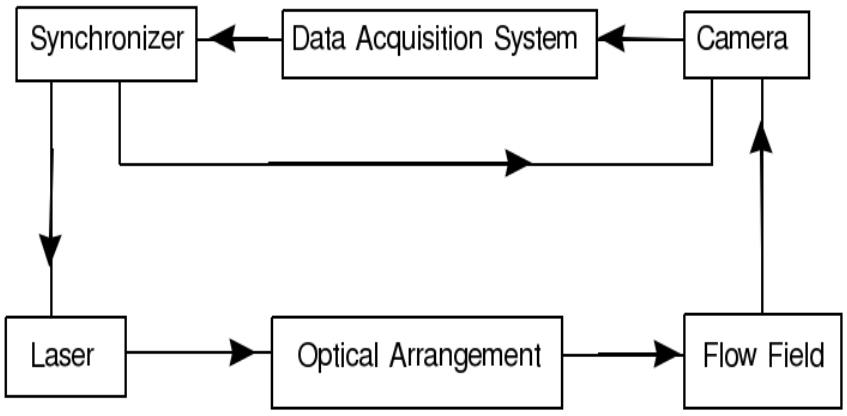

Figure 2.11: Schematic of the instrumentation and the flow of control and data

2.5.4 PIV particles

Neutrally Buoyant seeding particles in sufficient number density per unit volume are required for PIV experiments to obtain quality signal for image processing. LaVision 55 micron poly amid seeding particles with relative density 1.1g/cc and Dantec Dynamics 50 micron poly amid seeding particles with relative density 1.03g/cc were used separately as tracer particles. Lesser concentration of particles cause reduction in the number of tracable pathlines and reduces the quality of the signal. Excess quantity of tracers if used makes more light scattered thus reducing the share for fluorescence and can affect the PLIF readings. Higher concentration also lead to accumulation of particles and gives wrong velocity vectors.

Soap was used in small amounts to prevent the agglomeration of PIV particles while mixing. The ambient fluid domain (water) and the incoming salt solution were seeded with PIV particles at the same concentration. The experiments were conducted within the timescale where the particles stay neutrally buoyant. The particles start settling upwards or downwards at larger timescales.

2.5.5 Rhodamine dye

Rhodamine 6G is an organic fluorescent dye used as a tracer in aqueous solutions to determine the rate of transport and mixing of components in a flow. Rhodamine 6G is pumped by second harmonic ($532nm$) from an Nd-YAG Laser. It displays fluorescence with the emission peak at $566nm$. The dye was selected for its higher photo-stability (Lifetime = $500Wh$), high fluorescence quantum yield (0.95) and absorption peak near the laser wavelength. The dye solution is prepared by dissolving the highly soluble R6G chloride ($C_{28}H_{31}ClN_2O_3$) in water.

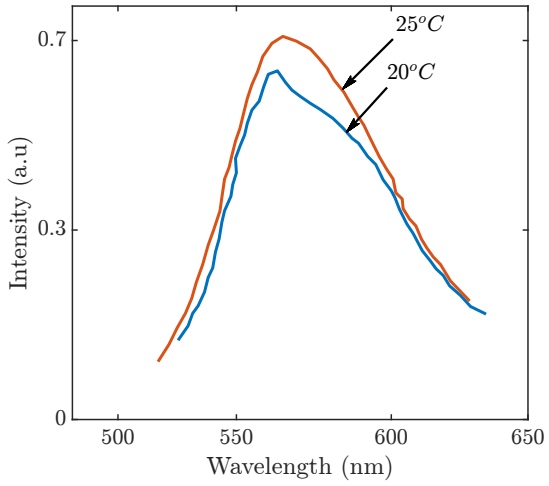

Figure 2.12: Emission Spectra of Rhodamine 6G

The incoming salt solution was seeded at four times larger concentration than the water in the large tank. Unlike PIV where the PIV tracer concentration remain same throughout the experiment, PLIF tracer concentration varies. In experiments with confinements, the fluorescent dye accumulates near inlet after some time and over expose the images and distort contrast values preventing the capture of flow structures. Thus PIV experiments can be run for longer timescales than PLIF experiments.Therefore the PLIF experiment decides the possible duration of synchronized PIV-PLIF experiments.

2.5.6 Constant flow rate mechanism for salt solution and removal of air bubbles

The salt solution was made to flow from an overhead tank to maintain constant flow rate throughout the duration of the experiment. The height of free surface in the overhead tank containing the salt solution was maintained by a recirculating circuit with salt solution, using a set of small tanks and a pump. The overhead tank for salt solution was connected to another overhead tank with water seeded with PIV and PLIF tracers at the same concentration with respect to the ambient fluid domain in the large tank. This tank circulates the ambient fluid through all channels and flush air bubbles out.

2.6 Measurements and calibration

2.6.1 Density difference between fluids

The experiments were performed at dilute concentrations of salt in the salt solution, within the Boussinesq range ($\frac{\Delta\rho}{\rho} << 1$). Density difference of $5kg/m^3$ between water and salt solution (20^oC) was used for the buoyant jet experiments. This value corresponds to a density ratio of 0.5%

2.6.2 Refractive index matching

Optical flow diagnosis methods like PIV and PLIF of a flow requires fluids of same refractive index interacting, even though their densities are different. Variations in density of fluids are related to their refractive index. The refractive index of the salt solution is higher than water. Since water and salt solution are miscible, there will be dynamic change in refractive index values during the mixing of salt solution and water inside the small box. The differences in refractive index in a disordered manner, in the path of the laser beam would deflect the laser beam in different directions and causes variation in intensities, reducing the quality of the PIV and PLIF signals. Thus it is important to match the refractive indices of water and the salt solution used in experiments without

changing the density differences between them for any quantitative analysis. A difference of 0.0002 in refractive index between the mixing fluids can render the PIV images unworthy [4].

McDougall [37] was the first to propose an approach to denote refractive index and density as functions of concentrations of solutes in water, using Taylor series expansion. Hannoun [26] had proposed the NaCl-ethanol pair for refractive index matching. Addition of ethanol can increase the refractive index of water depending upon its concentration. Since ethanol is a lighter fluid, along with the addition of refractive index, it causes a reduction in density. Therefore instead of having a fluid pair with density difference caused only by salt, and having different refractive indices, a similar fluid pair can be made with same density difference, caused by adding lesser salt on one fluid and ethanol on the other fluid, with same refractive index. Sixteen sample solutions were made at different concentrations of salt in water and ethanol (ROH) in water, covering the entire span of density differences required for the experiments and the trend lines were plotted. The solutions were tested at 20^oC and atmospheric pressure.

For the measured values of densities and refractive indices, cubic interpolation equations were found to provide a smooth fit within the range of values. Calculations were done to find out the mass of salt and ethanol required to match refractive index for a specific density difference. The curve fitting equations are

$$Density\ of\ salt\ solution,\ \rho_s = 238.07x^3 + 124.22x^2 + 706.86x + 998.53 \tag{2.3}$$

$$Refractive\ Index\ of\ salt\ solution,\ RI_s = 4.5744x^3 - 0.5998x^2 + 0.1912x + 1.3336 \tag{2.4}$$

$$Density\ of\ ethanol\ solution,\ \rho_a = -71.205y^3 + 274.66y^2 - 188.24y + 998.46 \tag{2.5}$$

$$Refractive\ index\ of\ ethanol\ solution,\ RI_a = 0.7875y^3 - 0.059y^2 + 0.0642y + 1.3336 \tag{2.6}$$

In above equations, x represents the concentration of salt and y represents the concentration of ethanol in mass fraction. The density of salt solution was varied from $1001.31kg/m^3$ to $1055.42kg/m^3$ and the density of ethanol solution was varied from $997.72kg/m^3$ to $983.57kg/m^3$ – which covers a wide range of density differences $\Delta\rho \in (0, 65)\ kg/m^3$ required for the experiments. These four equations were used to find the mass of salt and ethanol required to match refractive index of two fluids having a specified density difference $\Delta\rho$. Refractive index matching was done upto four digits after the decimal point.

Sample solutions were made from the concentration values obtained from the equations and, density and refractive index were measured to verify the equations. The density and refractive index were measured by a Rudolf Analytic density-meter and an Atago 3810 refractometer, respectively, and are found to be matching with above equations. The least count of (i) the density-meter is $0.01 kg/m^3$ and (ii) refractometer is 0.0001 units.

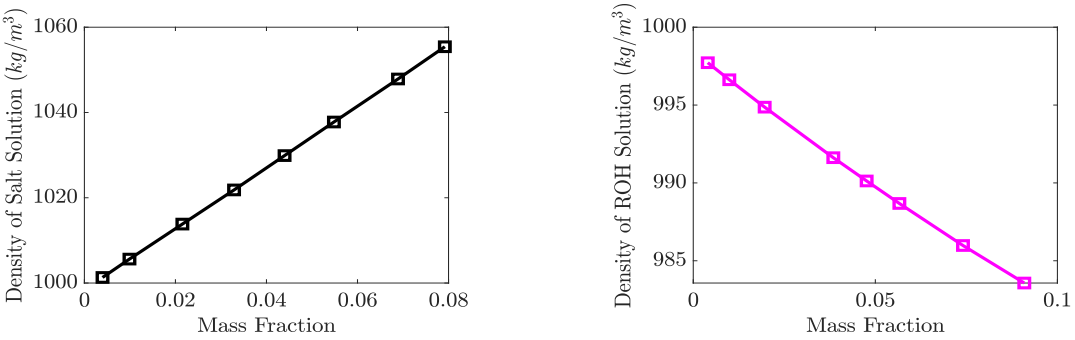

(a) Salt solution (b) Ethanol solution

Figure 2.13: Density plots of salt solution and ethanol solution for a mass fraction ranging from 0-0.1. Addition of salt increases the density and addition of ethanol decreases the density. The change in density is higher for the addition of salt compared to ethanol

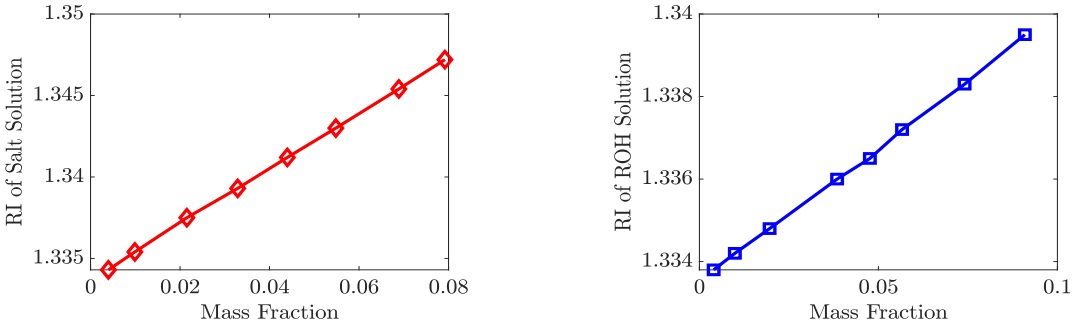

(a) Salt solution (b) Ethanol solution

Figure 2.14: Refractive Index plots of salt solution and and ethanol solution for a mass fraction ranging from 0-0.1. There is a steady increase in the refractive indices in both cases. The rates of increase in refractive index with respect to mass fraction are comparable for both solutions

2.6.3 PLIF calibration

The minimum and maximum values for the concentration of Rhodamine dye were selected to be $15\mu g/l$ and $60\mu g/l$. The ambient fluid domain was seeded with the dye to get a concentration of $15\mu g/l$, for background illumination and the salt solution was seeded to get a concentration of $60\mu g/l$. Zero concentration of the dye gives zero fluorescence with laser.

Images of the ambient fluid domain were taken at zero concentration and at a concentration of $15\mu g/l$. With these two values, the slope of the intensity Vs Concentration line was obtained. Once the linear equation was obtained, any intermediate value of fluorescence intensity between the maximum and minimum concentrations used in the experiment could be computed. The laboratory temperature was maintained at 20^oC throughout the experiment so as to get consistent intensity from both the fluorescent dye and the pulse laser.

2.6.4 Laser and image intensity correction

The pulse laser was found to have a warm up period for reaching steady intensity levels for the pulses. Trials were conducted for the duration of actual experiments to check the pattern of variation of laser pulse intensity. Images were captured at $10Hz$ for $50s$ and intensity variation at various regions of the image were found out. It was observed that the laser intensity variations get limited to less than 5% after $5s$ from the first pulse. Therefore only the images after first $5s$ were used for calculations. The difference in intensity between pulses and unevenness in intensity in the vertical dimensions were corrected using a cubic interpolation filter.

2.6.5 Image straightening

Simultaneous capturing of images for PIV and PLIF requires two cameras synchronized with the laser. To keep both cameras perpendicular to the illuminated plane, the cameras have to be kept at large distance from the illuminated plane of flow which would result in the reduction in intensity of images. Hence the cameras were kept at an angle with each other so as to keep them closer to the illuminated plane. A tilt in camera position affects the PIV results more than PLIF results as PIV measures a vector field and PLIF measures a scalar field. Therefore the PIV camera was kept perpendicular to the illuminated plane and the PLIF camera was kept at an angle (5^o). This causes warping of the captured images. Straightening of images were done to reduce distortions.

Images of a calibration plate with grid was taken by both cameras. The common region of interest was identified and images from both the cameras were transformed and made to overlap on this common region of interest. The image pixel coordinates were converted to physical units for further calculations. Thus both the PIV and PLIF cameras take pictures of the same area, within a particular boundary. This helps in getting simultaneous velocity and concentration fields at any particular point on the illuminated plane. The straightened images represent a physical area of size 480mm x 280mm.

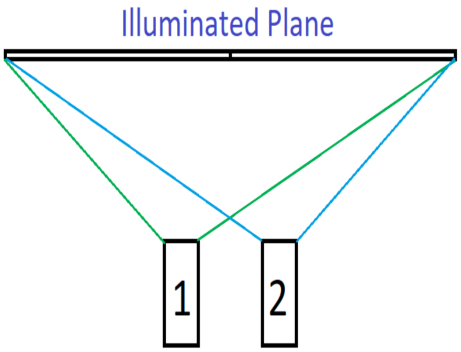

Figure 2.15: Field of view of camera-1 and camera-2 recording the same domain. The asymmetry in the lateral direction stretches the vectors generated from particle tracking

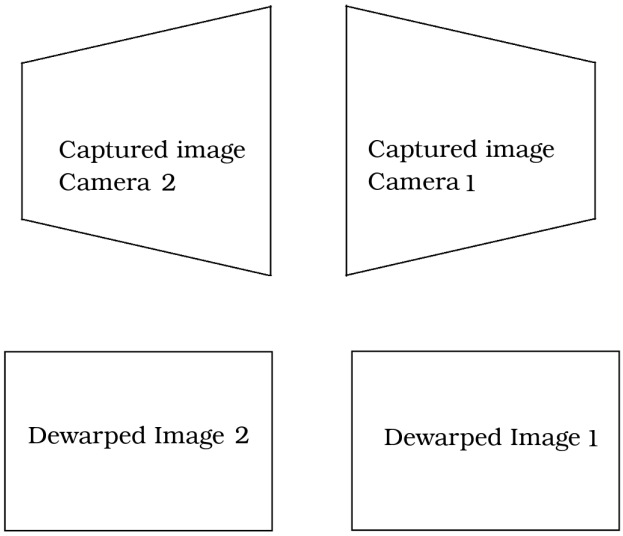

Figure 2.16: Warped images captured from PIV and PLIF cameras were straightened before processing. The results from straightened images were overlapped to find the simultaneous velocity-density field

2.6.6 Selection of time interval for PIV

The laser and the cameras were synchronized to fire and capture image pairs. The time between these images in a pair or the time between pulses (Δt) is an important parameter for PIV. The value of Δt should be sufficiently long to see the motion of the fluid but should be short enough that the tracer particles do not cross the interrogation window or the plane of illumination. Trials were conducted to find the optimum (Δt) for different flow rates. Lower values of (Δt) are used for high Reynolds number flows. The PIV image pair time interval depends on the flow rate as well as density of the salt solution in the set of experiments conducted. The values of Δt for different inlet Reynolds number are given in table 2.1.

2.6.7 Coordinate systems

Two Coordinate systems were used in plotting. The overall flow characteristics were plotted using the XY coordinate system with origin O, at the top left corner of the image. The jet flow characteristics were plotted using $\tilde{X}\tilde{Y}$ coordinate system with origin, $\tilde{O}$ below the flow inlet, the axes $\tilde{X}$ and $\tilde{Y}$ parallel to X. The $\tilde{Y}$ axis is aligned with the jet centreline.

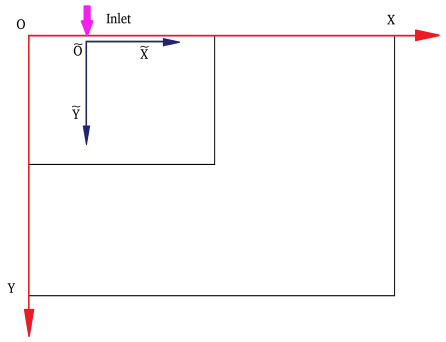

Figure 2.17: The adopted XY coordinate system has the positive Z axis into the plane of the paper. The positive Y axis is vertically downwards and the positive X axis is anti parallel to the laser beam.

2.6.8 Inlet Reynolds number

The present experiments study about a turbulent jet in a near-field confinement. In the near-field, it is assumed that the turbulent jet retains many of its inlet characteristics. Inlet Reynolds number is an important parameter that helps to describe the inlet flow conditions. In the experiments conducted, salt solution was introduced to the confinement as a buoyant jet at three different flow rates for different experiments, from three different elevation of the overhead salt solution tank. Reynolds number of the flow based on

the inlet parameters was calculated to differentiate the flows. It should be noted that the flow velocity at the inlet decreases with time (less than 10%) and thus the mean Reynolds number may not convey information about instantaneous flow characteristics but it explains the overall volume transport or roughly, the strength of the source of buoyant fluid. The mean elevation head, density of the incoming fluid, inlet-diameter and dynamic viscosity of the incoming fluid are required to determine inlet Reynolds number.

$$\text{Inlet Reynolds Number, } Re = \frac{\rho V_o D}{\mu} \tag{2.7}$$

where ρ is the density of the salt solution measured with density-meter Rudolph Research Analytical DDM2911, V_o is the mean inflow velocity calculated by measuring the net flow volume and time of flow, D is the nozzle diameter at inlet and μ is the dynamic viscosity measured with Rheometer Anton Paar $MCR302$.

The mean inflow velocity was calculated from the total volume inflow measured over time. Water level in the large tank was measured before starting the flow and after a time "t". Rise in the water level times the base area of the large tank gives the volume added in time "t". The mean velocity of inflow was calculated by dividing the volume flow rate by the inlet cross section area. For the values of height of free surface of salt solution in the overhead tank of $55mm$, $126mm$ and $216mm$ from the inlet of the confinement, the Reynolds numbers at the inlet were approximately 1500, 2600 and 3700 respectively. These values corresponds to a laminar flow, a transition flow and a turbulent flow. These values were selected to demonstrate the difference in the jet flow pattern. These elevation head values would be addressed in subsequent sections as low head or flow rate, medium head or flow rate or high head or flow rate cases.

2.7 Correlations

Velocity and concentration are coupled quantities in the case of buoyancy driven flows of miscible fluids. A quantitative way of describing the coupling between certain parameters is through defining two point correlation functions which is widely used in the field of natural ventilation. Correlation between velocity and concentration can be checked for time scales where the flow is quasi-steady. A velocity ($V(x,y)$)-concentration ($C(x,y)$) correlation function $G(x,y)$ is the correlation of the fluctuation of the velocity and concentration from their average values and can be defined as

$$G(x,y) = \langle (V(x,y) - \langle V(x,y) \rangle)(C(x,y) - \langle C(x,y) \rangle) \rangle \tag{2.8}$$

In the case of a perfect direct linear relationship where one value increases with the

other, the correlation coefficient approaches +1 whereas in the case of a perfect inverse linear relationship where one value decreases with the increase in the other value, the correlation coefficient approaches -1 and it is called anticorrelation. For independent quantities, the correlation coefficient would approach zero.

2.8 List of experiments on confined jets

Each experiment was conducted at a particular mean flow rate of salt solution.

List of types of experiments - Buoyant jet in confinement				
Sl.No	Exit Geometry	Mean Flow Rate (lpm)	$\Delta t(\mu s)$	Density Difference (kg/m^3)
1	Side	1.265	2000	5
2	Bottom			
3	Side	0.88	5000	
4	Bottom			
5	Side	0.489	10000	
6	Bottom			

Table 2.1: List of types of experiments conducted on buoyant jet in confinement.

Chapter 3

Turbulent, Buoyant Jet in Confined Space: Flow Dynamics

Synchronized PIV-PLIF experiments were conducted on unsteady, confined, vertical, turbulent, buoyant, round jet to understand the evolution of smoke and the pattern of mixing during fire in a small room. A cuboidal, acrylic box suspended in a water tank was used as the confinement and a jet of salt solution was fed in to it from its top surface. The inner dimensions of the cuboidal confinement were $212mm$ x $140mm$ x $140mm$ and the jet inlet diameter was $8mm$. This confined space extends upto $17D$ from inlet in the axial direction ($140mm \approx 17D$), $7D$ ($55mm$) upto one side wall, $9D$ ($70mm$) upto two vertical walls and $20D$ ($157mm$) upto the fourth vertical wall, where D is the jet inlet diameter (Fig. 3.1). The velocity and concentration measurements were made upto an axial length span of $0 - 15D$ from the inlet, in these experiments, instead of the full span of $0 - 17D$ from inlet, to avoid errors in PIV measurements caused by rigid walls in the near-field of the turbulent, buoyant jet.

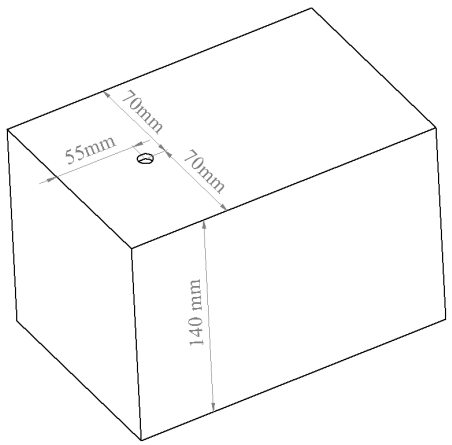

Figure 3.1: The schematic of the cuboidal confinement with the position of the inlet at its top surface.

The unsteady round jet source of salt solution was fed from an overhead tank kept at a fixed height. The salt solution was made to flow through a flexible pipe of length $2m$ from the overhead tank and become a fully developed flow before entering the confinement as a round jet (laminar length $= 0.13m$ for $Re = 3700$). The experiments conducted comprised primarily of two flow domains: the unsteady round jet and the volume around it inside the confinement. The case of mixing of jet in its near-field during fire emergency is similar to the case of fuel jets mixing in cylinders in internal combustion engines, but the confinement geometry changes continuously in these engine combustion chambers unlike the experiments described in this report.

The jet flow domain is primarily momentum driven and the flow inside the confinement away from the jet and outflow from the confinement are primarily buoyancy driven. The time scales are different for the jet of salt solution and the buoyancy driven convection from the confinement to the ambient flow domain. The buoyancy driven convection requires more time to reach a steady state by which time the fluorescent dye would fill the whole confinement, reducing the output signal quality. Thus the jet domain was studied in detail and the study focusses on the unsteady dynamics and mixing in the near-field of an unsteady, vertical, turbulent, buoyant, round jet in confinement.

During the experiment, the total fluid level in the large tank had risen and a difference in concentration had occurred in the confined space. Both these factors reduce the temporal mean inlet velocity of the jet by decreasing the net elevation head and the favourable concentration gradient. The data from the PIV analysis showed that there was a finite reduction in the jet axial velocity along the centreline between the first and second set of readings taken during the time periods $t = 0-50s$ and $t = 240-290s$ respectively. Further analysis were done on the profiles of temporal jet axial velocity along the centreline to understand the pattern of development of flow and to check velocity-density correlations.

The finite reduction in the axial velocity of the jet observed over a longer time period and the unsteady flow characteristics of the jet make it important to check the time scale over which the flow may be treated as quasi-steady. Reynolds averaging could be applied only for turbulent flows that are statistically quasi-steady over the selected time scale [52]. Since the flow in the jet domain and surrounding space inside the confinement are dynamically different, they need to be analysed separately.

The denser salt solution would get mixed with the water inside the confinement due to turbulence and high molecular diffusivity of salt. The turbulent mixing was caused by jet entrainment, enhanced by confinement in the axial and lateral directions and the flow exits. The jet entrainment pattern inside confinement needs to be analysed in par-

ticular. The flow outlets were positioned away from the jet and the flow through the outlets was slow. The role of flow outlets in the pattern of mixing in the jet domain was less significant compared to that of entrainment and confinement. In short, in the experiments conducted, there was a jet flow, eddies caused by jet-wall interactions, outward flow through flow outlets, a slow buoyancy driven convection from the bottom of the confinement to the top and in the case of side openings, a bidirectional flow from the ambient flow domain.

3.1 Velocity and density pattern

The continuous supply of denser fluid into the confinement keeps the time scale (L/U) of turbulence nearly constant throughout the experiment. This time scale is shorter than the time scales related to the frequencies of buoyancy generally by three orders of magnitude [51]. Thus the flow in the present studies falls under momentum-dominated flow and it exhibits typical characteristics of turbulent jet.

(a) $t = 10s$

(b) $t = 20s$

(c) $t = 50s$

(d) $t = 240s$

Figure 3.2: Confinement with side opening geometry with a jet inlet flow rate = $1.265lpm$ ($Re = 3700$). The observed laminar length was minimal as the salt solution had become turbulent even before reaching the jet inlet. High degree of mixing also could be observed in the images.

Experiments were conducted on turbulent jet cases with different flow rates ($1.265lpm, 0.88lpm$ and $0.489lpm$) and geometry conditions with $\Delta\rho = 5kg/m^3$ to understand the flow patterns of a decelerating, vertical, turbulent, buoyant, round jet in a cuboidal confinement. The flow rates of $1.265lpm, 0.88lpm$ and $0.489lpm$ correspond to Reynolds numbers $Re = 3700, Re = 2600$ and $Re = 1500$ respectively. The confinement in the axial dimension were placed at the near-field of the turbulent jet ($17D$). The inlet velocity profile can be considered to have a 'turbulent pipe-flow' velocity distribution. The images represent a physical area of dimension $480mm$ x $280mm$.

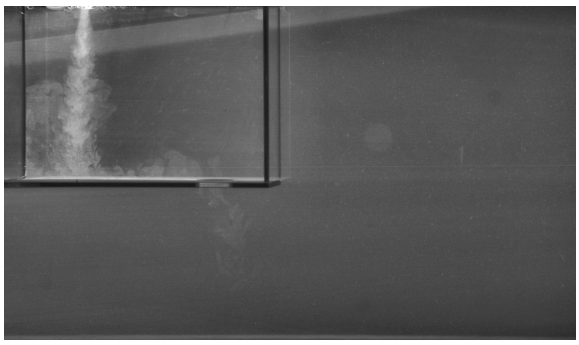

(a) $t = 10s$

(b) $t = 20s$

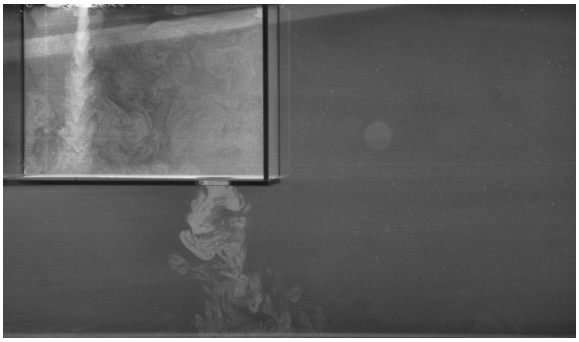

(c) $t = 50s$

(d) $t = 240s$

Figure 3.3: Confinement with bottom opening geometry with a jet inlet flow rate = $1.265lpm$ ($Re = 3700$). The observed laminar length was minimal as the salt solution had become turbulent even before reaching the jet inlet. High degree of mixing also could be observed in the images.

The cuboidal confinement has inner dimensions $212mm$ x $140mm$ x $140mm$ and the inlet is located at $55mm$ from the wall away from the laser and normal to it, on the centreline of the top face, along the longer edge. There are two separate configurations for the flow exits; one with a circular opening at the bottom wall of the confinement, centred $50mm$ away from the wall near to the laser and normal to it, on the centreline of the bottom face, along the longer edge and another configuration where the opening is placed on the centroid of the square side wall near the laser. Three flow rates were used to study the jet inlet Reynolds number dependence of the flow patterns. The flow evolution proceeds as shown in Fig. 3.2- 3.5.

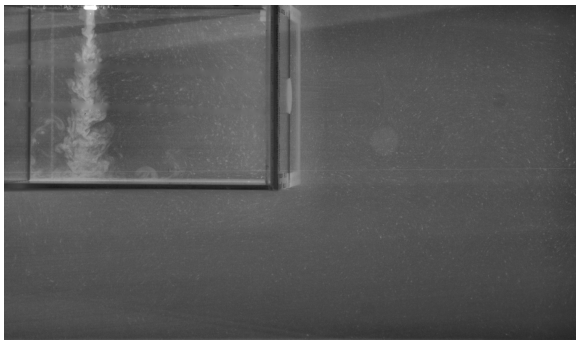

(a) $t = 10s$

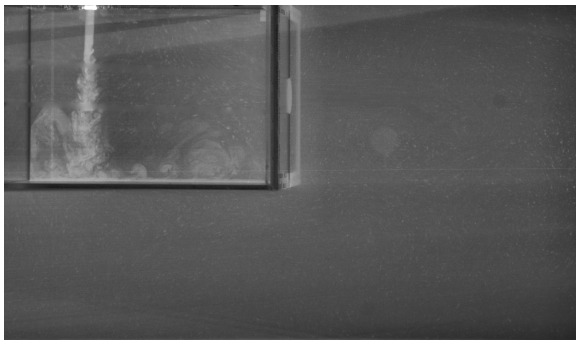

(b) $t = 20s$

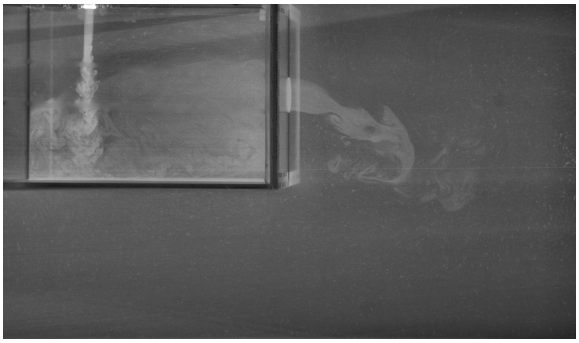

(c) $t = 50s$

(d) $t = 240s$

Figure 3.4: Confinement with side opening geometry with a jet inlet flow rate = $0.489lpm$ ($Re = 1500$). A steady laminar length was observed in this low flow rate case. Stable stratification and a clear neutral level were also observed.

Considering the extreme cases of Reynolds numbers, the jet with $Re = 3700$ is turbulent from the beginning for both side opening (Fig. 3.2) and bottom opening (Fig. 3.3) cases. It can also be observed that in these cases the fluorescent dye gets saturated due to high degree of mixing inside the confinement in the second set of measurements from $t = 240s$. Looking at the cases of jet with lowest Reynolds number ($Re = 1500$), it can be observed that the mixing is significantly lesser and a stable stratification is observed from the second set of readings from time, $t = 240s$ in both side opening (Fig. 3.4) and bottom opening (Fig. 3.5) cases.

Unlike many existing works in the topic where stratification and mixing caused by a jet in confinement were directly related to the flow exit geometry [35], the flow pattern inside the near-field confinement in the experiments conducted depends mainly on the jet inlet Reynolds number. The magnitude and range of Reynolds number used in the experiments conducted by Linden *et al.* [35] were smaller compared to the experiments described in the report. Since the separation between the inlet and outlets is less than that of the cases described in many of the existing literature, the chances of stable stratification inside the confinement are lesser for high Reynolds number flows ($Re > 2000$). Thus the natural ventilation for normal air circulation and natural ventilation for fire emergency or gas

leakage from pressurized tanks or pipes must be treated differently due to the difference in flow patterns caused by the difference in the strength of source of buoyancy.

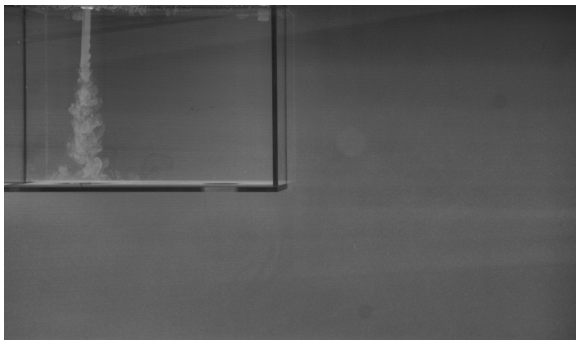

(a) $t = 10s$

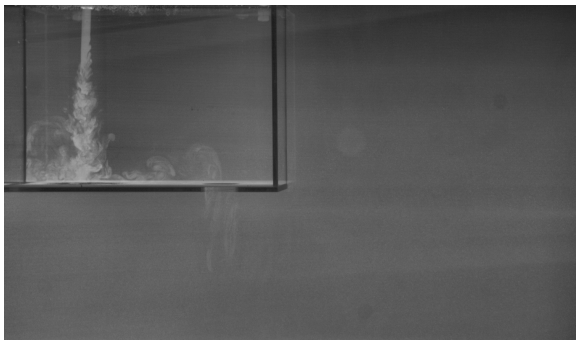

(b) $t = 20s$

(c) $t = 50s$

(d) $t = 240s$

Figure 3.5: Confinement with bottom opening geometry with a jet inlet flow rate = $0.489lpm$ ($Re = 1500$). A steady laminar length was observed in this low flow rate case. Stable stratification and a clear neutral level were also observed.

To understand the differences in flow due to a source of buoyancy in a confined space and due to density difference between the incoming fluid and the ambient flow domain, experiments were also conducted in the same set up without confinement and at different densities. In the range of Reynolds number used in the experiments, for a time period of $500s$ used in the experiments, various flow patterns were observed that range from the ones reaching steady state in the time frame of recording, to the ones that were transient all throughout the experiment.

3.2 PIV and PLIF measurements

Two sets of synchronized PIV-PLIF readings were taken from each experiment in the time period $0 - 290s$ from the beginning of the jet flow ($0 - 50s$ & $240 - 290s$). Each set of reading was taken for $50s$ at a sampling frequency of $10Hz$. From the first set of reading ($t = 0 - 50s$), image pairs from time $t = 5s$ from the starting of the jet flow to the time $t = 50s$ were taken for analysis. From the second set of reading ($t = 240 - 290s$), image

pairs from time, $t = 245s$ to $t = 290s$ were used for analysis. The data from the first $5s$ from each set of reading was discarded to avoid the errors caused by the fluctuations in laser intensity during the warm up time of the laser. The acquired PIV and PLIF images were transferred from the cameras to the PC during the time gap between the two sets of readings.

The time interval between PIV image pairs were taken as $2ms$ ($Re = 3700$), $5ms$ ($Re = 2600$) and $10ms$ ($Re = 1500$) for the experiments, based on the inlet flow conditions, in the decreasing order of jet flow rate. The PLIF camera also acquired image pairs at the same rate and the first image from each image pair from PLIF camera was used for PLIF analysis. The vertical span of the confinement covered in the measurement was $17D$ and the horizontal span of the confinement covered in the measurement was $26D$. The momentum of the jet was adjusted by changing the mass (density) and inlet velocity (flow rate from the overhead tank) of the incoming salt solution.

3.3 Jet spread angle

Laboratory investigations of free jet penetrating into a quiescent fluid of the same density reveal that the envelope containing the turbulence caused by the jet adopts a nearly conical shape. The lateral size of the round turbulent jet increases with the downstream distance from the nozzle. The initial jet radius was not zero but a finite nozzle radius, $(D/2)$. Therefore there exists a virtual origin for the jet cone. This point of origin is called the virtual source of the jet.

The radius R of the jet at any axial location is proportional to the distance y downstream from the discharge location. Further, the opening angle was the same, regardless of the nature of the fluid (air or water) and of other circumstances (such as diameter of outlet and discharge speed). This universal angle is 11.8^o giving approximately 24^o from side to opposite side [28] . It follows that the coefficient of proportionality between the jet radius R and the downstream distance y from the outlet is $tan(11.8^o) \approx 1/5$

$$R(y) = \frac{1}{5}y \tag{3.1}$$

The temporal evolution of jet angles for the experiments conducted (confined jet) were studied (Fig. 3.6) and it was observed that the jet angles were comparable to the free jet cases at time, $t = 5s$ and later moves towards an angle of 18^o at time, $t = 45s$. This reduction in the jet angle is different from the cases reported by Shin *et al.* [18] where it was stated that the temporal evolution of free jet spreading angle showed less variation over the duration of the experiment. The variation in the present experiments could be due increase in the turbulence in the surrounding fluid and also due to the trapped eddies

caused by the confinement.

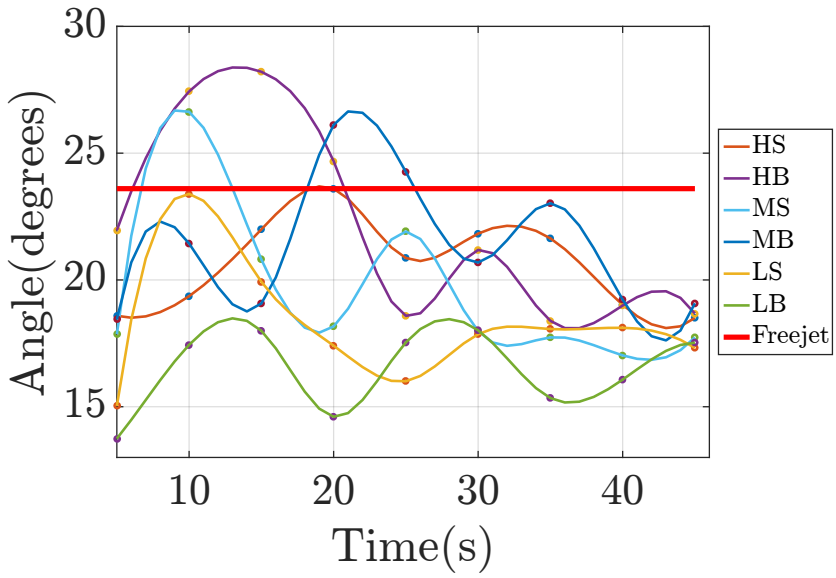

Figure 3.6: The temporal variation of the jet angle from $t = 5s$ to $t = 45s$ (**S**: side opening, **B**: bottom opening, **H**: flow rate $= 1.265lpm, Re = 3700$, **M**: flow rate $= 0.88lpm, Re = 2600$, **L**: flow rate $= 0.489lpm, Re = 1500$). The value of jet angle for a free jet is also provided for reference

3.4 Temporal evolution of jet axial velocity along the centreline

Trends in the mean centreline jet velocity profiles for **1.** Statistically steady, free, submerged, turbulent jet and **2.** Statistically unsteady, free, submerged, turbulent jet of same fluid show certain remarkable differences. Assuming self-similar behaviour for the jet, the continuity equation can be modified to get the mean (ensemble average) centreline jet velocity profile [18] as

$$\overline{V}_c(y,t) = A(t)y^n \tag{3.2}$$

where $\overline{V}_c(y,t)$ is the ensemble mean axial velocity along the centreline and y is the axial dimension. The factor $A(t)$ depends on time and the exponent n varies for different self-similar regions but constant within a region. Self-similarity condition requires $n = -1$ for the statistically steady, turbulent jet and $n = 1$ for statistically unsteady (decelerating), turbulent jet [18]. While the ensemble mean centreline jet velocity is inversely proportional to the axial distance in statistically steady jet, it is directly proportional to axial distance in statistically unsteady jet. The experiments were conducted for jet of heavier, miscible fluid entering a lighter ambient fluid in confinement and the trend of

centreline velocity needs to be checked.

Assessing the case qualitatively, an immiscible, heavier fluid jet entering a lighter ambient fluid has higher momentum than a jet of same fluid and the velocity is expected to decay over a longer period. But when the heavier but miscible salt solution enters the confinement as a jet, it undergoes mixing and loses momentum faster than the previous case. Mixing and the reduction in the axial velocity of the incoming jet are coupled. During the course of time, the denser fluid parcels after mixing forms stratified layers near the bottom wall of the confinement, reducing the favourable density gradient for the incoming jet, which also reduces the jet inflow into the confinement. Finally, the small variation in the level of ambient fluid in the large tank also contributes towards the reduction in jet axial velocity along the centreline. Acceleration or deceleration of the fluid can cause increase in shear, open up larger areas to interact and that can enhance entrainment and mixing.

The linear dependence of the ensemble mean centreline velocity on the axial coordinate shows possible dependence between the temporal mean centreline velocity and the axial coordinate which is relevant for fire safety cases. To understand the effect of mixing in deciding the jet centreline velocity over time and vice versa, the present experiments were analysed to see the pattern of temporal mean axial velocity of the jet along the centreline in confined space for a submerged jet of a miscible fluid with a small density difference with the ambient fluid ($\Delta\rho = 5kg/m^3$) and the plots were made (Fig. 3.7- 3.12). The jet centreline velocities were plotted for different time instances ($t = 5 - 50s, t = 245 - 290s$) upto a distance of $15D$ from the inlet (inlet diameter, $D = 8mm$). The bottom wall of the confinement was at a distance of $17D$ from the inlet.

The plots of temporal mean axial velocity of the jet along the centreline at various time instances show a narrow region near the inlet ($0 - 5D$) after which the velocity decreases. A turbulent jet is expected to accelerate for a short distance downstream from the nozzle but due to high noise in this region caused by out-of-plane motions of PIV particles, no quantitative studies are made for the centreline profiles upto $5D$ from the inlet. The point of inversion of slope of centreline velocity varies for different cases based on the inlet Reynolds number of the jet. The temporal mean centreline jet velocity profiles were plotted and curve fitting was done to evaluate the trend. The readings with higher noise, caused by high velocity 3D motion of particles, shadows from the edges of the outlet, were not considered in curve fitting.

The trend of the mean centreline jet velocity profiles was nearly linear and thus a first order curve fitting was implemented. The temporal mean centreline jet velocity profile follows a linear trend with negative slope from the region where the slope of velocity

changes. The same pattern is observed in all the experiment cases with various inflow and outlet positions. The analysis was done for periods of time ($5s$) starting at different time instants and similar trends were found. It shows how the temporal flow profiles switch towards different self-similar modes.

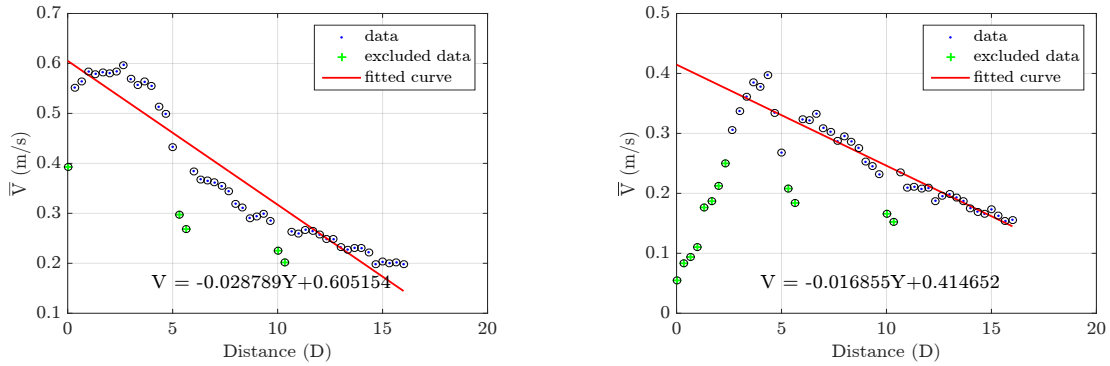

(a) HS30 $t = 5 - 50s$ (b) HS30 $t = 245 - 290s$

Figure 3.7: Mean of the jet axial velocity along centreline for inlet flow rate = $1.265lpm(Re = 3700)$ in a confinement with $\phi 30mm$ side opening

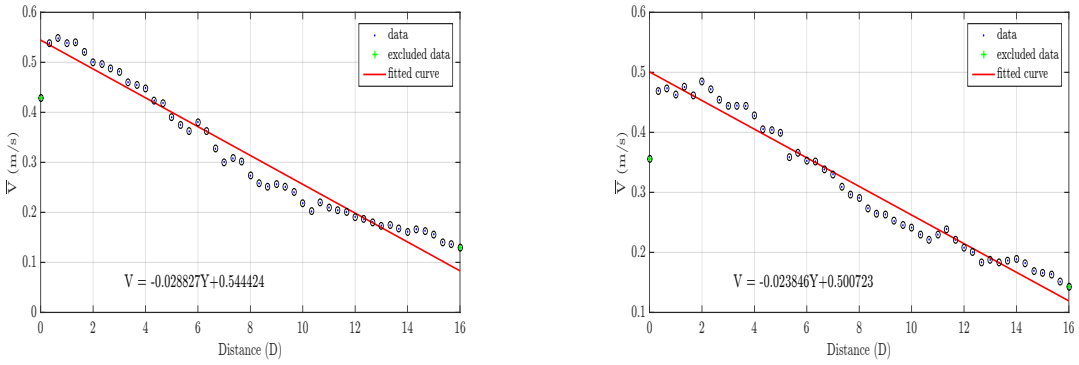

(a) HB30 $t = 5 - 50s$ (b) HB30 $t = 245 - 290s$

Figure 3.8: Mean of the jet axial velocity along centreline for inlet flow rate = $1.265lpm(Re = 3700)$ in a confinement with $\phi 30mm$ bottom opening

At $Re = 3700$, the bottom opening case (Fig. 3.8) shows clear linear dependence of temporal mean jet centreline velocity on axial coordinates. The temporal mean jet centreline velocity in side opening case at $Re = 3700$ also shows linear dependence on axial coordinate but not as evident as the bottom opening case (Fig. 3.7). At $Re = 2600$ also, the temporal mean jet centreline velocity has linear dependence with the axial coordinate in the bottom opening case (Fig. 3.10) having a higher match with the predicted model compared to the side opening case (Fig. 3.9). At $Re = 1500$, temporal mean jet centreline velocity of bottom opening case has similar linear behaviour like previous cases (Fig. 3.12) but the temporal mean jet centreline velocity in side opening case shows weak linear

dependence with the axial coordinate (Fig. 3.11).

The profiles of temporal mean axial velocity of the jet along the centreline, for side opening cases have higher deviation from the linear behaviour compared to the bottom wall opening cases in experiments with decrease in Reynolds number ($Re = 3700$ to $Re = 1500$). It is an indication of the higher tendency for stable stratification in the bottom opening cases over the side opening cases (Fig. 3.7- 3.8). The pattern is similar for low flow rate cases also (Fig. 3.9- 3.12). The outlier values at $5D$ and $10D$ are caused by the shadow of the side opening in all side opening cases.

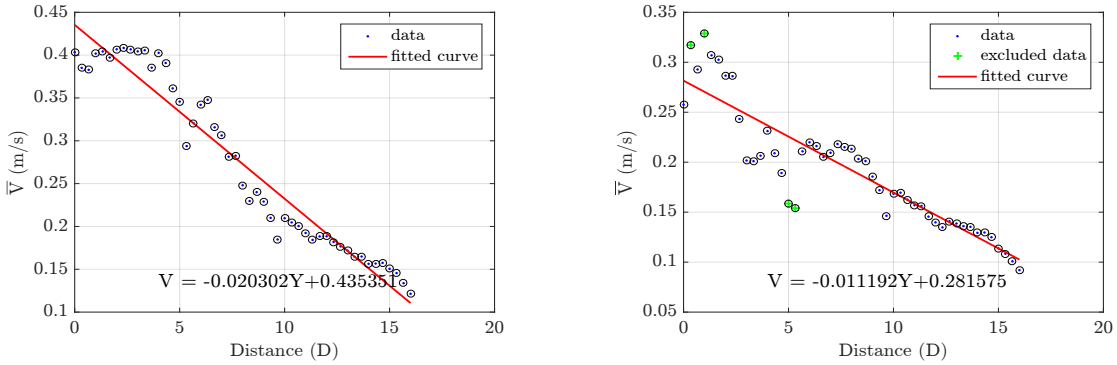

(a) MS30 $t = 5 - 50s$ (b) MS30 $t = 245 - 290s$

Figure 3.9: Mean of the jet axial velocity along centreline for inlet flow rate = $0.88lpm(Re = 2600)$ in a confinement with $\phi 30mm$ side opening

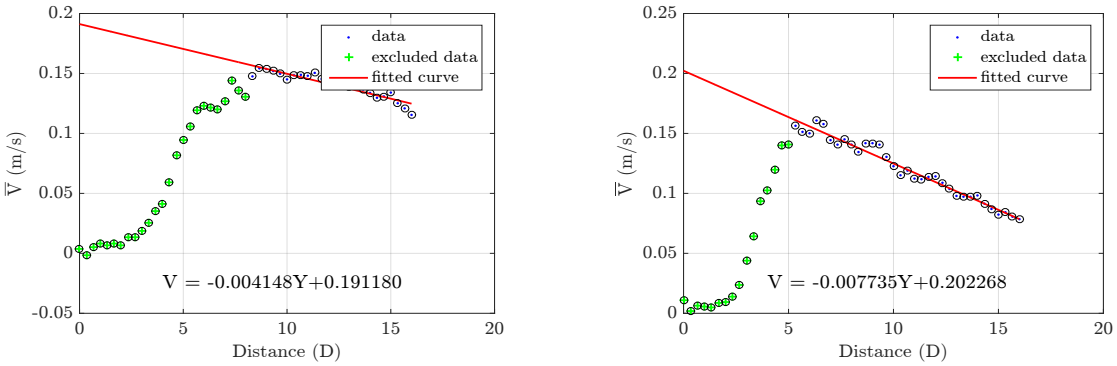

(a) MB30 $t = 5 - 50s$ (b) MB30 $t = 245 - 290s$

Figure 3.10: Mean of the jet axial velocity along centreline for inlet flow rate = $0.88lpm(Re = 2600)$ in a confinement with $\phi 30mm$ bottom opening

Acceleration of the buoyant jet was observed from $5 \leq Y/D \leq 15$ for jet flow cases with a density ratio of 3.16% [51]. But in the present studies, the density ratio used was 0.5% and therefore it acts more like a non-buoyant decelerating jet which is evident in the plots from $Y/D = 5 - 15$. The PIV signals from $Y/D = 0 - 5$ in the present studies have less resolution and hence cannot be used to make any quantitative assessment.

The profiles of temporal mean axial velocity of the jet along the centreline maintain temporal self-similarity. But in the case of mean concentration, it shows increasing trends which are temporally different since it is a scalar. PLIF images of experiments with and without concentration gradient were taken. The variation in intensity in PLIF images with concentration gradient shows the role of diffusion between the phases whereas the PLIF images without the concentration gradient shows how pure mixing due to turbulence happens.

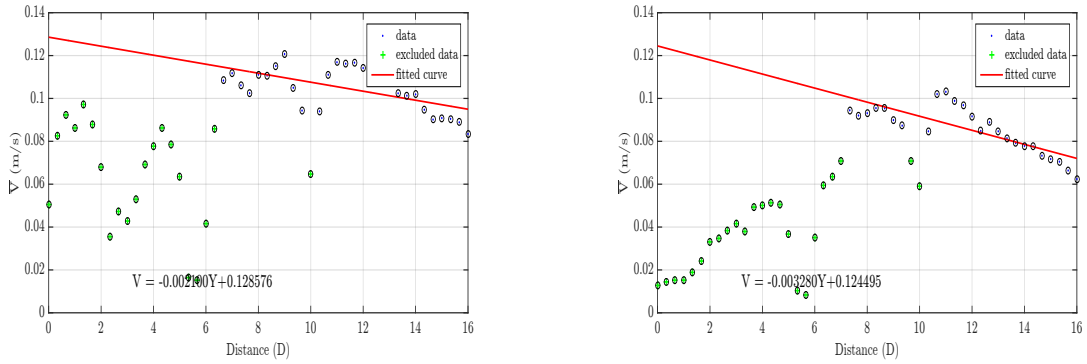

(a) LS30 $t = 5 - 50s$ (b) LS30 $t = 245 - 290s$

Figure 3.11: Mean of the jet axial velocity along centreline for inlet flow rate = $0.489lpm(Re = 1500)$ in a confinement with $\phi 30mm$ side opening

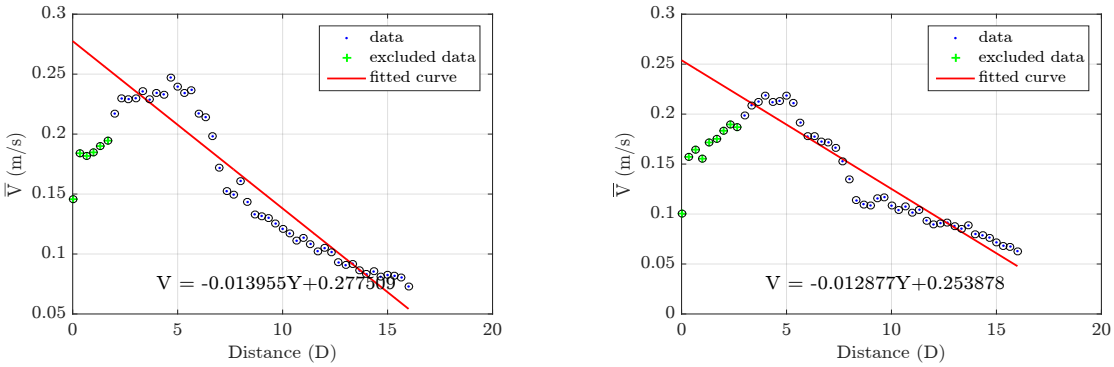

(a) LB30 $t = 5 - 50s$ (b) LB30 $t = 245 - 290s$

Figure 3.12: Mean of the jet axial velocity along centreline for inlet flow rate = $0.489lpm(Re = 1500)$ in a confinement with $\phi 30mm$ bottom opening

3.5 Unsteady turbulent round jet

The pattern of temporal evolution of jet and mixing are important in various biological, industrial and environmental flows. The time scale associated with reaching statistically steady state and the degree of mixing in this period decide various design and safety parameters of different engineering flow systems.

The temporal evolution of the jet was analysed for all the experiments from $t = 5-50s$ and $t = 245 - 290s$. Comparing the distribution of velocity in these two time periods will show whether the flow is statistically steady or unsteady. It is important to verify whether the jet flow is temporally steady or unsteady during the period of measurement so as to select appropriate analysis methods.

The axial velocity values at 4 different points along the jet centreline, separated by a distance of $D, 2D, 4D$ and $8D$, were checked for the duration of measurement. The temporal values of axial velocity from these points for different flow cases were plotted (Fig. 3.13- 3.16). A third order curve fitting was overlapped with the scatter plots to show the trend of velocity, along with a lower limit (set at 50% of the value shown in the trend of velocity) and an upper limit (set at 150% of the value shown in the trend of velocity). It can be observed that within a set of reading, the variation of axial velocity has a dispersed spread on either sides of the trend line throughout the period of data recording with a variation of 100% of the half value.

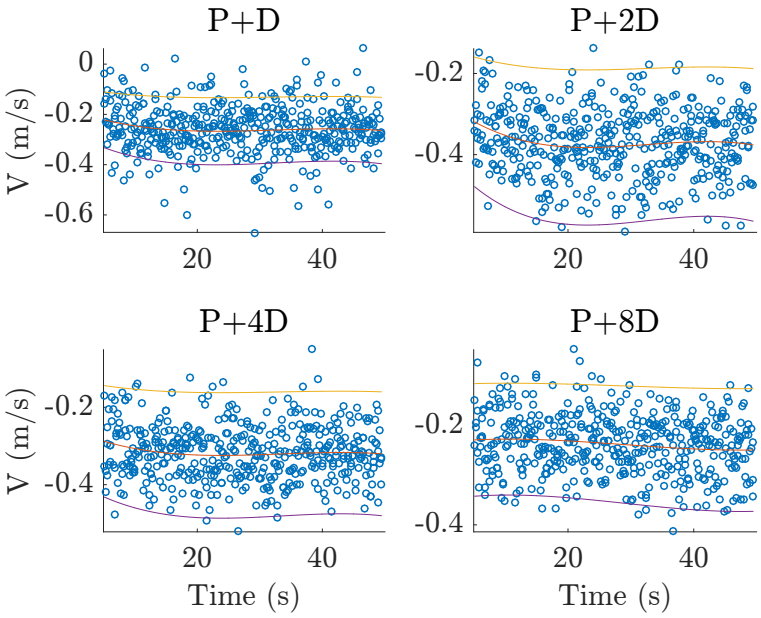

Figure 3.13: Temporal evolution of the jet axial velocity along the centreline, in the experiment with an inlet flow rate = $1.265lpm$ ($Re = 3700$), for a confinement with $\phi 30mm$ side opening ($t = 5 - 50s$)(P is the end of inlet and D is the inlet diameter)

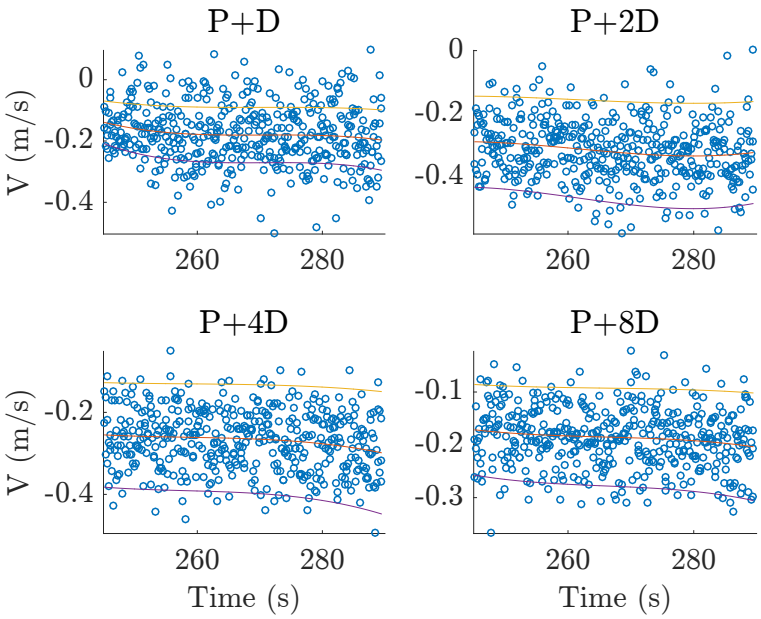

Figure 3.14: Temporal evolution of the jet axial velocity along the centreline, in the experiment with an inlet flow rate = $1.265lpm$ (Re = 3700), for a confinement with $\phi 30mm$ side opening ($t = 245 - 290s$)(P is the end of inlet and D is the inlet diameter)

Comparing the pattern of velocity at time, $t = 5 - 50s$ (Fig. 3.13) and $t = 245 - 290s$ (Fig. 3.14) at $Re = 3700$ in a side opening case, it can be seen that there is a reduction in velocity at all four axial locations plotted. Similar trend is seen for bottom opening case also at Re = 3700. Reduction of velocity with time happened also for the other four cases also (Re = 2600 with side opening, Re = 2600 with bottom opening, Re = 1500 with side opening, Re = 1500 with bottom opening) and they are provided in Section .1.1. Autocorrelations were performed on the signals and weak correlations were observed (Fig. 3.17- 3.18). Similar trend of weak correlation was observed for the temporal evolution of axial velocity for the remaining test cases also.

Since there is a time dependence for the jet velocity, the mean flow changes with time and therefore these are not statistically steady turbulent flow cases. The sum of fluctuations deviated away from zero. Therefore a relevant time scale needs to be identified where the flow is quasi-steady and thus Reynolds averaging can be applied. From the autocorrelation analysis, it could be noticed that there is no particular correlation existing over this time period for the jet axial velocity along the centreline. A gradual reduction in the velocity also could be observed in the plots. Thus the jet in the experiments falls under the category of statistically unsteady, decelerating, turbulent, buoyant, round jet.

The lack of temporal correlations in axial velocity allows averaging to be done on time scales larger than the eddy turnover time of the flow. The *eddy turnover time* of the flow in confinement is related to the dimensions of the largest eddies near the jet domain and

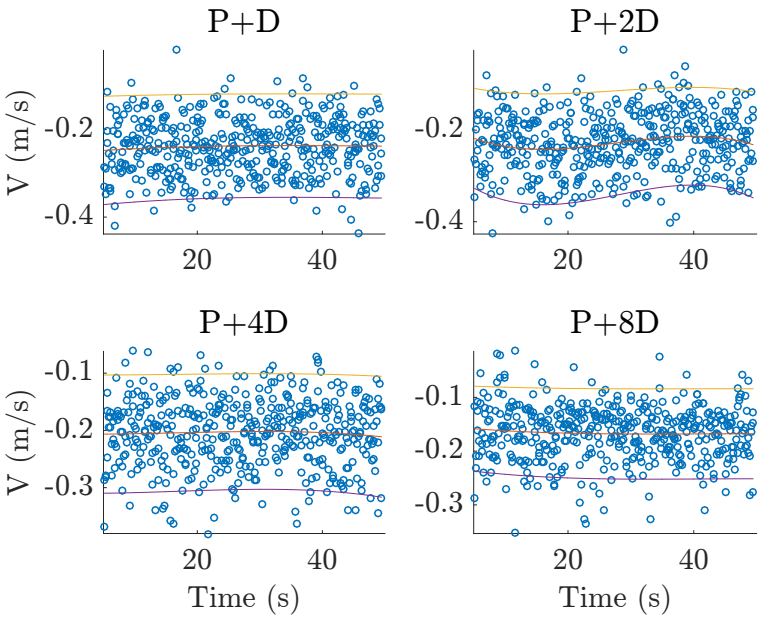

Figure 3.15: Temporal evolution of the jet axial velocity along the centreline, in the experiment with an inlet flow rate = $1.265lpm$ (Re = 3700), for a confinement with $\phi 30mm$ bottom opening ($t = 5 - 50s$)(P is the tip of inlet and D is the inlet diameter)

the rms velocity of fluid at this length scale, which was obtained from ensemble averaging.

The eddy turnover time for a jet of $Re = 1500 - 3700$ falls in the range $2 - 3$ seconds. It was calculated from the size of the largest eddies and the root mean square of velocity fluctuations from ensemble averaging of experiments. An averaging time window of 5 seconds (50 images) was selected to analyse the quasi-static flow features in the jet region. Thus quasi-steady state analysis can be applied for the flow in this time window and Reynolds averaging of velocity also can be applied. Similar tests were conducted on all experiment data sets to understand the flow behaviour.

Turbulent flow comprises of flow structures of multiple length and time scales. The fluid parcels would be undergoing both transport and strain in this type of flows. The rate of strain is higher for the smaller flow structures compared to the larger flow structures. Since the strain rate has units of $time^{-1}$, the time scales associated with strain would be inversely proportional to the strain rate. Hence the smaller flow structures have time scales less than the larger flow structures. Therefore the eddy turnover time can accommodate all dynamics in the smaller scales.

In the experiments conducted, the salt solution jet is flowing throughout the duration of the experiments causing a mean flow. When the pattern of these flows were observed, they appeared to be evolving during the complete duration of the period of data acquisition which means that the integral time scale of the evolution of the flow is larger than

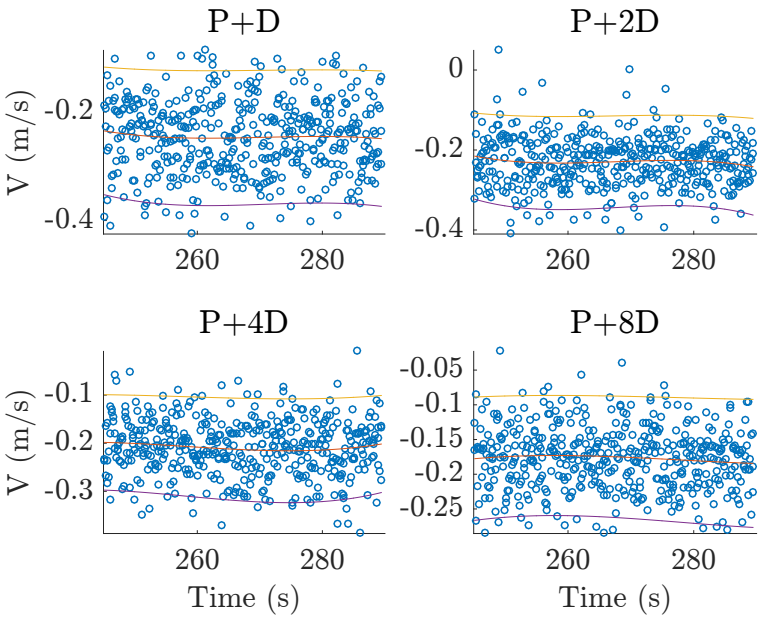

Figure 3.16: Temporal evolution of the jet axial velocity along the centreline, in the experiment with an inlet flow rate = $1.265lpm(Re = 3700)$, for a confinement with $\phi 30mm$ bottom opening ($t = 245-290s$)(P is the tip of inlet and D is the inlet diameter)

the recording time. However portions of flow were identified where spatial or temporal correlations did not exist in the time scale. Checking the sizes of eddies and their time of dispersal, the relevant time window for averaging was chosen based on the eddy turnover time. The temporal evolution of velocities at various points were plotted and verified.

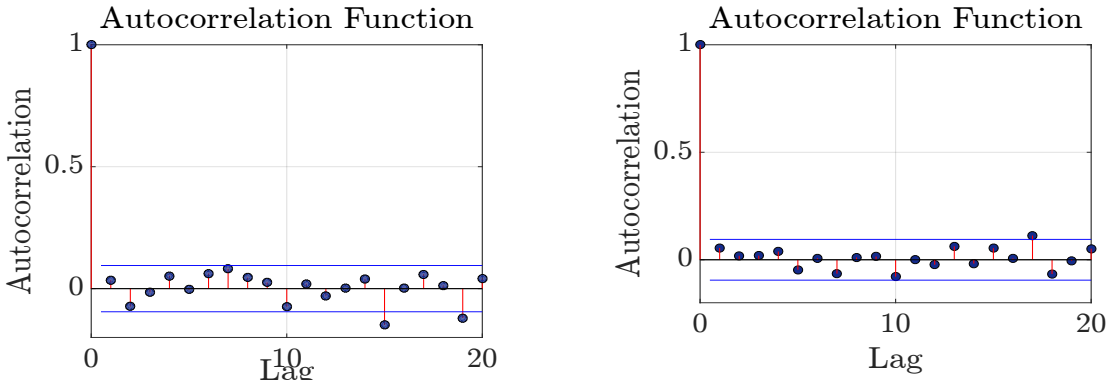

(a) P+D

(b) P+2D

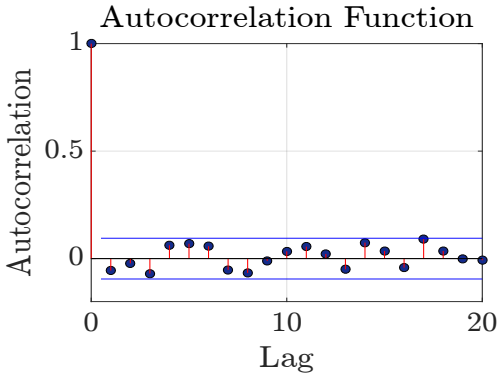

(c) P+4D

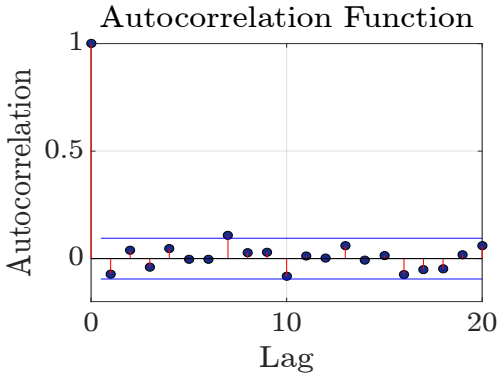

(d) P+8D

Figure 3.17: Autocorrelation of the jet axial velocity along the centreline at different axial locations from time, $t = 5 - 45s$, for a confinement with side opening of $\phi 30mm$ and jet inlet flow rate = $1.265lpm(Re = 3700)$

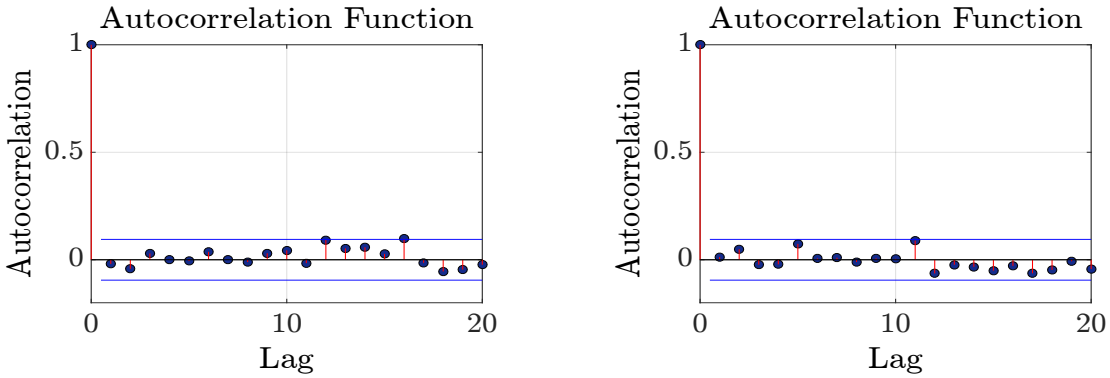

(a) P+D

(b) P+2D

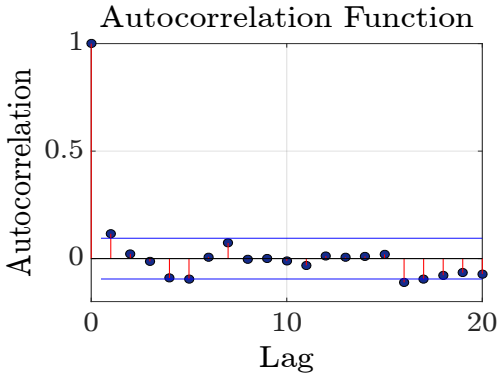

(c) P+4D

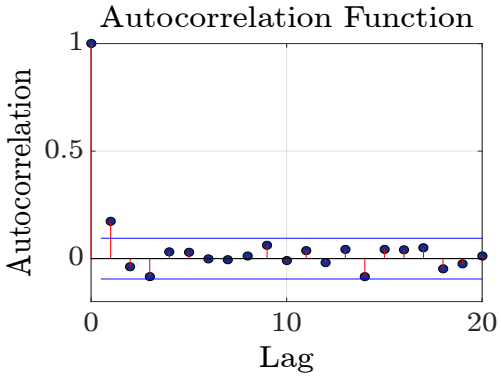

(d) P+8D

Figure 3.18: Autocorrelation of the jet axial velocity along the centreline at different axial locations from time, $t = 5 - 45s$, for a confinement with bottom opening of $\phi 30mm$ and jet inlet flow rate = $1.265lpm(Re = 3700)$

3.6 Cross section profiles of axial velocity

Jet experiments were conducted with a density difference of $5kg/m^3$ with confinement. The cross section profiles of axial velocity at different axial locations for a steady, unconfined jet are expected to be self-similar after an axial distance greater than $40D$. They exhibit nearly Gaussian profiles throughout the axial direction in the far-field. Thus a curve fitting model can be proposed for the radial cross section profiles of axial velocity $V(y, x)$ as

$$V(y, x) = V_{max}\ e^{\left(-\frac{x^2}{2\sigma^2}\right)} \tag{3.3}$$

where y is the axial dimension, x is the radial dimension inside the jet cone, V_{max} is the maximum axial velocity at a particular axial location from inlet and σ is the standard deviation for the velocity distribution. 95% of the area under the curve falls under four times the standard deviation which makes $4\sigma = D$, where D is the diameter of the nozzle ($D = 2R$). Thus combining eq. 3.3 and eq. 3.1,

$$V(y, x) = V_{max}\ e^{\left(-\frac{50x^2}{y^2}\right)} \tag{3.4}$$

Experiments were done on unsteady, confined, turbulent jet cases and the variation of temporal evolution of jet axial velocity along the centreline was plotted. After plotting the cross section profiles of axial velocity at different axial locations, it could be observed that these profiles are nearly self-similar.

3.7 Behaviour of the jet-core with Re

McNaughton and Sinclair [38] categorizes different regions in a submerged jet in cylindrical confinement, based on the jet inlet Reynolds Number. They had defined a "Semi-turbulent jet" domain of Reynolds number between 1000 and 3000 where a clear laminar length was observed at the region near the entry of the jet into the ambient fluid domain (Fig. 3.19). The jet interaction with the surroundings was minimal in this region. Similar flow pattern was observed in the experiments conducted and as per the literature, the jet in experiments would start to entrain the ambient fluid domain only after some characteristic length (laminar length). In a "fully turbulent jet" ($Re > 3000$), strong entrainment flows can be observed immediately after the entry of jet into the ambient fluid domain and hence the laminar length is found to be shorter than a jet with $Re < 3000$.

The submerged jet flow can be divided into three distinct flow regimes: **1.** The laminar length regime, **2.** the developing flow regime and **3.** the fully developed flow regime [1]. The entrainment flows are weaker near the laminar length regime. There would be less

fluctuation in the jet axial velocity along the centreline in the laminar length regime. Thus the jet axial velocity along the centreline in the laminar length regime would be nearly equal to its value at the jet exit. The axial length of the laminar length could go upto $4D$ for a round jet, where D is the diameter of the inlet, according to the works of Martin [27] and the Nasa technical report by Gauntner *et al.* [24] states that the laminar length could vary from $4.7D$ to $7.7D$

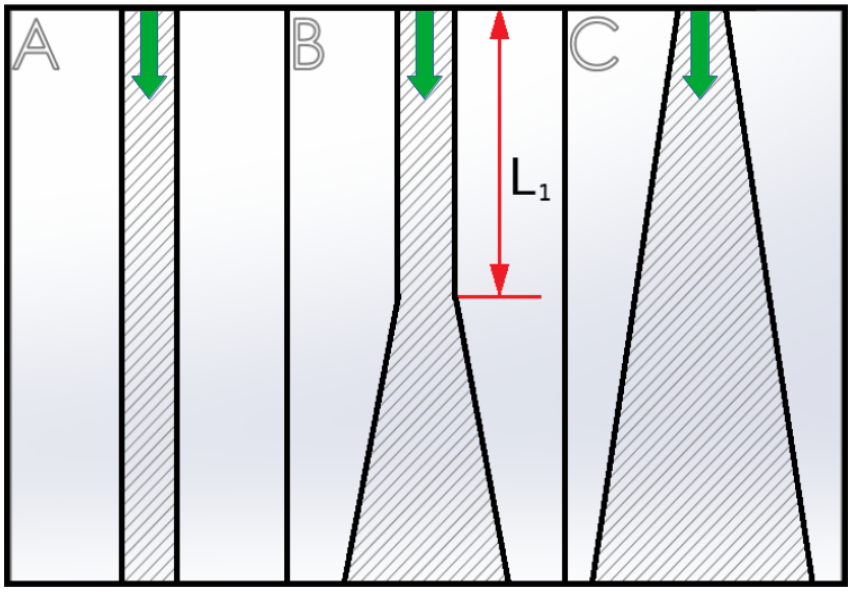

Figure 3.19: The variation of laminar length of vertical jet in cylindrical confinement based on inlet Reynolds number. The jet inlets are located at the top of the figure. The root of the arrows shows the locations of the source of each jet and the arrow heads show the direction of jet. **A**: Fully laminar jet ($300 < Re < 1000$, dependent on vessel dimensions), **B**: Semi-turbulent jet ($1000 < Re < 3000$, dependent on vessel dimension. The laminar length (L_1) is marked from the source to the fully developed region), **C**: Fully turbulent jet ($Re > 3000$, independent of vessel dimensions).

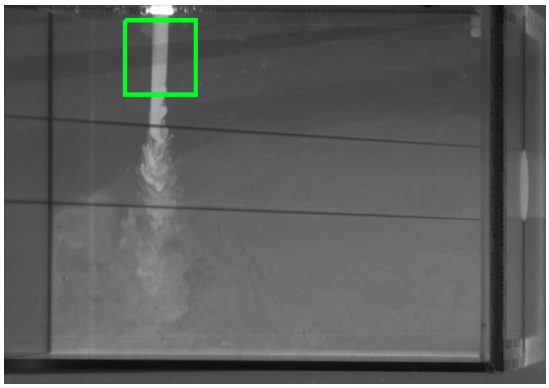

(a) Semi turbulent jet, $Re = 1500$, flow rate $= 0.489 lpm$

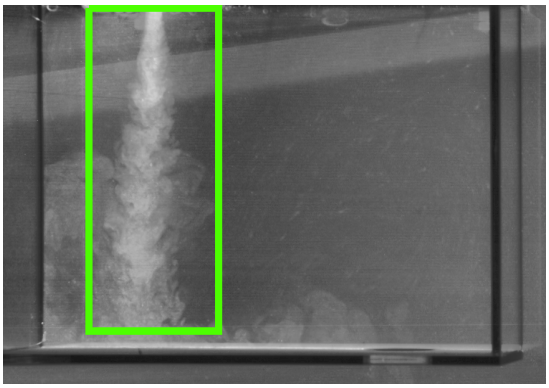

(b) Fully turbulent jet, $Re = 3700$, flow rate $= 1.265 lpm$

Figure 3.20: Variation of laminar length with Reynolds number for confined jet

Fig. 3.20 shows the difference in laminar length with Reynolds number. While the laminar length is clearly visible in for jet with $Re = 1500$, the laminar length is minimal for the jet with $Re = 3700$. The near-field of the turbulent jet is the region where the jet retains the inlet flow characteristics. Up to a downstream distance less than $5D$ from the inlet, the lateral spread and the axial velocity variations of the jet are minimal. The higher axial velocity at this region causes high noise in PIV data as the time gap between PIV image pairs would be set at a larger time scale based on the mean velocity of the jet.

The turbulence instabilities becomes evident on the jet boundary after an axial distance of $4D - 5D$ and start penetrating into the jet-core which causes lateral spread and reduction in the axial velocity of the jet with downstream distance from the nozzle. With increasing downstream distance, the encroachment of turbulence generated at the interface into the jet-core also increases and jet-core gets consumed further. The core of the jet less affected by the turbulence thus obtains a conical shape (potential cone). The axial distance from the nozzle to the tip of the potential cone of the jet is an important factor that decides the span of the flow development region. The fully developed turbulent jet flow starts after some axial distance downstream from the point where the potential cone cease to exist.

3.8 Statistically unsteady self-similar state

The difference in the pattern of jet axial velocity along the centreline, between a statistically steady jet and a decelerating jet affects the patterns of entrainment. The radial (cross sectional) profiles of mean axial velocity of the jet at different axial locations were plotted for all the experiment cases and the trends were analysed. It is known that Gaussian self-similar profiles were observed for the statistically steady jet cases. In the present study,cross sectional profiles of mean axial velocity were made at different time instants based on the *eddy turnover time*. Nearly self-similar velocity profiles were observed in the case of confined jet cases studied in the experiment in the near-field (upto $15D$).

The radial profiles of mean axial velocity was normalized by the peak axial velocity at the same axial location and the radial distance by the *full width half maximum* of the cross section profiles of the mean axial velocity. Radial profiles of mean axial velocity over different time periods shows that the self-similarity varies temporally. The idea of temporal self-similar axial velocity profiles from the works of Boree *et al.* [7, 8] on a decelerating jet between two statistically steady states can now be safely extended towards gradually decelerating jet over a longer period.

The cross section profiles of mean axial velocity and concentration, at different axial locations of the incoming jet were analysed to check the evolution of the flow. The jet flow was found to have a conical shape. The denser fluid from the jet moved upto the bottom of the confinement, undergoes mixing en route, occupied the bottom most layers of the confinement and displaced the existing lighter fluid upwards. Thus, the mixed, intermediate density fluid kept on rising to the top of the confinement. A jet inside confinement with higher momentum caused better mixing and weaker stratification was observed inside the confinement. Thus the strength of stratification depends on the momentum and on the strength of the source of buoyancy also. Strong stratification pattern was observed in jet with low flow rate ($Re < 1800$). It was also observed that the ambient fluid trapped at the top region of the confinement remained less mixed.

3.8.1 Velocity

The size of the jet at the inlet is not zero but the finite nozzle diameter. Therefore the jet can be assumed to possess a conical shape with its apex taken as a virtual origin or a point source. This virtual origin could be calculated from the values of jet cone angle given in section 3.3. For a free jet, the virtual origin is located at $2.5D$ from the tip of the inlet [28]. In the present study, the location of the virtual origin varied from $1.45D$ to $1.74D$ from the tip of the inlet, for different cases at time $t = 40s$.

The widening of jet-cone is linear with distance, and the axial velocity profiles of the jet at different cross sections, except those near the orifice, were similar to one another, after suitable averaging accounting turbulent fluctuations. Observations suitably averaged over many turbulent fluctuation time scales show that the axial velocity of the jet obeys a law of similarity: All cross-sections appear nearly identical, except for a stretching factor, and the axial velocity profile across the jet exhibits a nearly Gaussian shape. Therefore, it can be written as

$$U(y,r) = U_{max} e^{\frac{-r^2}{2\sigma^2}} \tag{3.5}$$

$$g\frac{\Delta\rho}{\rho}(y,r) = g\frac{\Delta\rho}{\rho}(y).e^{-r^2/b^2} \tag{3.6}$$

where y is the downstream distance along the jet (counted from the virtual source), r is the cross-jet radial distance from its centreline, $U_{max}(y)$ is the maximum speed at the centreline, $\sigma(y)$ is the standard deviation related to the spread of the profile across the centreline, g is the acceleration due to gravity, ρ is the density of the fluid and $\Delta\rho$ is the difference in density between the two fluids.

The Mean Cross Sectional (MCS) axial velocity profiles of the jet normalized by the local peak axial velocity were plotted along a horizontal axis normalized by the *full-width at half-maximum* (FWHM) values. FWHM denotes the separation between the horizontal coordinates (independent variable) when the value of the function (dependent variable) is half of its peak value (peak amplitude) (Fig. 3.21). Gaussian functions can be integrated by simple multiplication if its full width at half maximum is known.

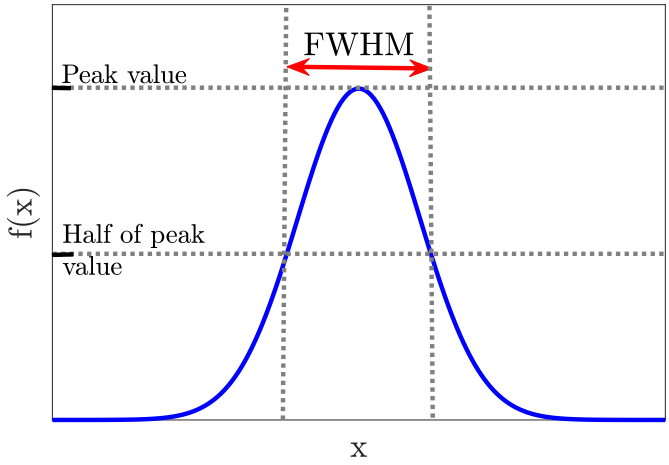

Figure 3.21: Full width at half maximum (FWHM) for a Gaussian curve

The These MCS axial velocities were found to have a nearly Gaussian profile. The incoming jet was found to accelerate initially due to buoyancy $0 - 5D$, decelerate and, spread as a ceiling jet once it reaches the bottom region of the confinement. Line plots are used to denote the mean axial velocity values for tracing the approximate shape. Any line between two data points in these plots does not represent velocity values.

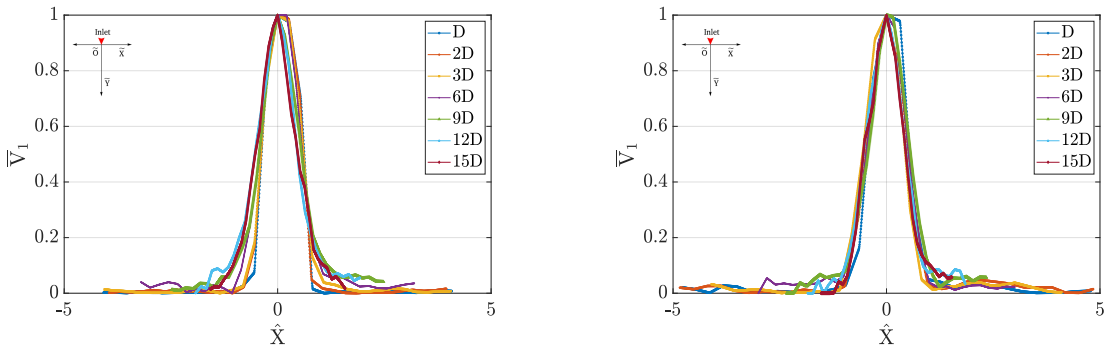

(a) Side opening geometry

(b) Bottom opening geometry

Figure 3.22: Radial profiles of mean axial velocity of the jet at different axial positions for jet with an inlet flow rate = $1.265lpm(Re = 3700)$. Since the jet was turbulent from the inlet, nearly self-similar profiles were observed in this case. The data was taken from the first set of readings from $t = 5 - 50s$ averaged based on the eddy turnover time.

Highly self-similar MCS axial velocity profiles were obtained in the case of high Reynolds number jet flow. At $Re = 3700$, self-similarity of the MCS axial velocity is more evident in the case of jet in confinement with a bottom opening (Fig. 3.22b) compared to the cases of jet in confinement with a side opening (Fig. 3.22a).

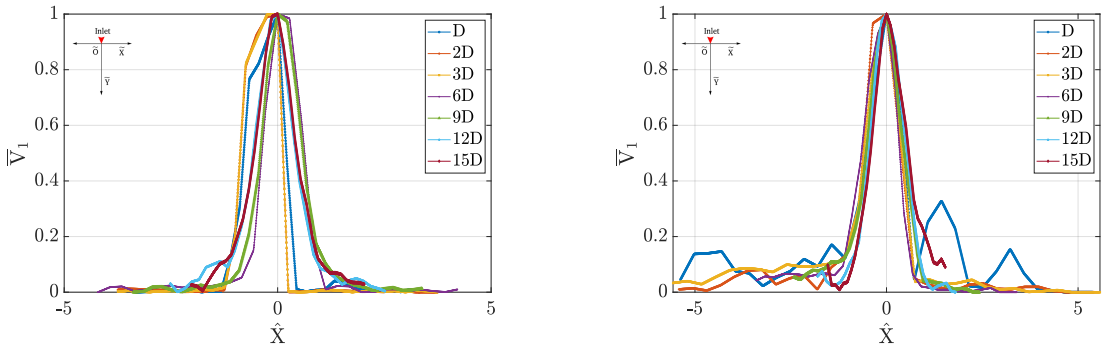

(a) Side opening geometry (b) Bottom opening geometry

Figure 3.23: Radial profiles of mean axial velocity of the jet at different axial positions for jet with an inlet flow rate = $0.88lpm(Re = 2600)$. Since the jet is undergoing from laminar to turbulent in the test cases, clear self-similarity profiles were not observed. The data was taken from the first set of readings from $t = 5 - 50s$ averaged based on the eddy turnover time.

In the case of jet flow with $Re = 2600$ in side and bottom opening confinements, higher self-similarity in MCS axial velocity is observed in the case of jet flow in confinement with a bottom opening (Fig. 3.23b) compared to the jet flow in confinement with a side opening (Fig:3.23a). But in both of these jet flow cases ($Re = 2600$), the self-similar character of MCS axial velocity is weaker compared to the jet flow cases with higher Reynolds number ($Re = 3700$).

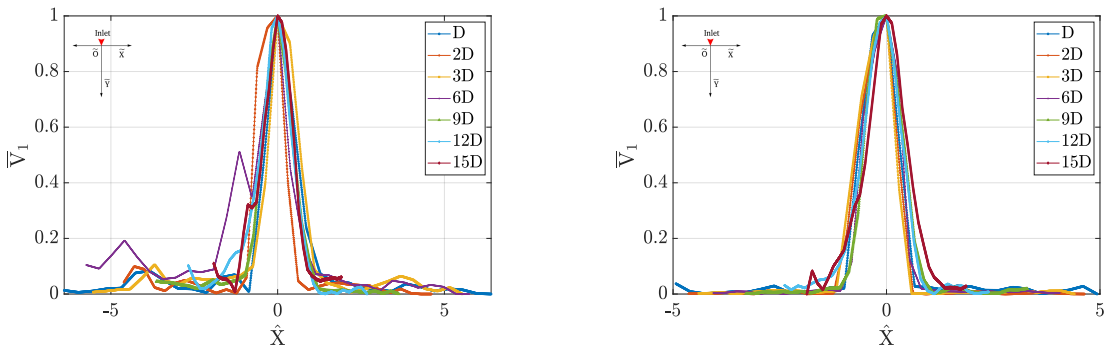

(a) Side opening geometry (b) Bottom opening geometry

Figure 3.24: Radial profiles of mean axial velocity of the jet at different axial positions for jet with an inlet flow rate = $0.489lpm(Re = 1500)$. Since the jet is mostly laminar in the test cases, self-similarity profiles were not observed. The data was taken from the first set of readings from $t = 5 - 50s$ averaged based on the eddy turnover time.

Nearly self-similar MCS axial velocity profiles were obtained for the jet flows with low Reynolds number ($Re = 1500$) also like the previous two cases. The self-similar character of MCS axial velocity for the jet flows at $Re = 1500$ is comparable to that of the jet flows at $Re = 2600$ and weaker than that of jet flows at $Re = 3700$. In these cases also, more dominant self-similar MCS axial velocity profiles were observed in jet flow in confinement with a bottom opening (Fig. 3.24b) over jet flow in confinement with a side opening (Fig. 3.24a). It is evident in the experiments that the higher self-similarity in axial velocity is observed where the jet has lesser laminar length (Fig. 3.20, 3.22).

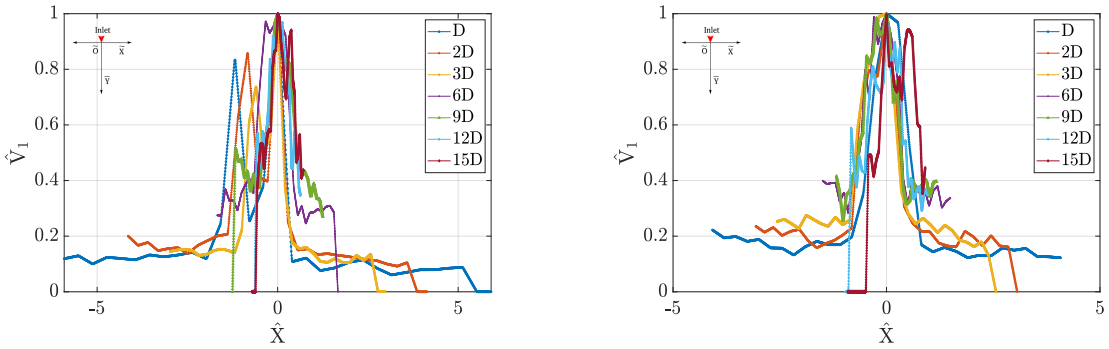

(a) Side opening geometry

(b) Bottom opening geometry

Figure 3.25: Radial profiles of rms axial velocity of jet at different axial positions with an inlet flow rate = $1.265 lpm (Re = 3700)$

The rms axial velocity of the jet was measured in all the experiment cases and the the values were plotted (Fig. 3.25- 3.27). For all values of Reynolds number, the self-similar characteristics of rms axial velocity are weaker compared to that of the MCS axial velocity profiles. Out of these weakly self-similar profiles, the jet flow cases in confinement with a bottom opening (Fig. 3.25b, 3.26b) has relatively more self-similar characteristics over the side opening cases (Fig. 3.25a, 3.26a) for $Re = 3700$ and $Re = 2600$.

Unlike the jet flow cases with $Re = 3700$ and $Re = 2600$, the jet flow case with $Re = 1500$ has similar pattern of rms axial velocity for both side and bottom opening cases (Fig. 3.27). Stable stratification was observed in these flow cases and the laminar length of jet in both cases were greater than the higher Reynolds number cases. Similarity in jet domain and stratified layers contribute to similar fluctuation patterns for the jet flows with low Reynolds number in confinement with side or bottom opening.

3.8.2 Concentration

The radial profiles of mean concentration normalized by the local maximum concentration at different axial locations were plotted and it could be observed that these profiles are

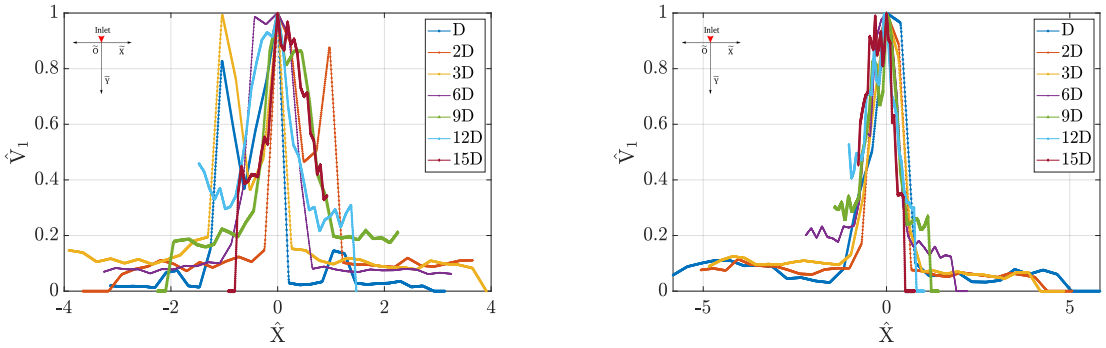

(a) Side opening geometry

(b) Bottom opening geometry

Figure 3.26: Radial profiles of rms axial velocity of jet at different axial positions with an inlet flow rate = $0.88lpm(Re = 2600)$

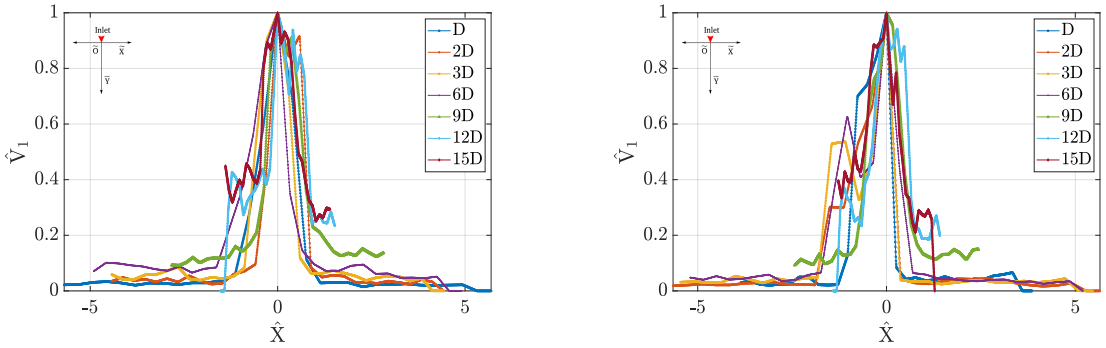

(a) Side opening geometry

(b) Bottom opening geometry

Figure 3.27: Radial profiles of rms axial velocity of jet at different axial positions with an inlet flow rate = $0.489lpm(Re = 1500)$

nearly self-similar (Fig. 3.28- 3.30). It can be also observed that the mixing pattern is different for side opening cases and bottom opening cases. The side opening cases have larger spread of concentration near the jet-core. The the radial spread of fluctuations in axial velocity were higher in the case of confinement with side opening compared to confinement with bottom opening.

Looking at the cross section profiles of concentration at $Re = 3700$, it can be observed that they exhibit nearly self-similar behaviour upto $15D$. This is an important information in the case of decelerating turbulent buoyant jet in a near-field confinement.

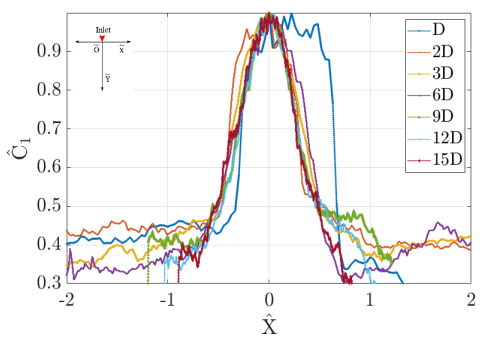

(a) Side opening geometry

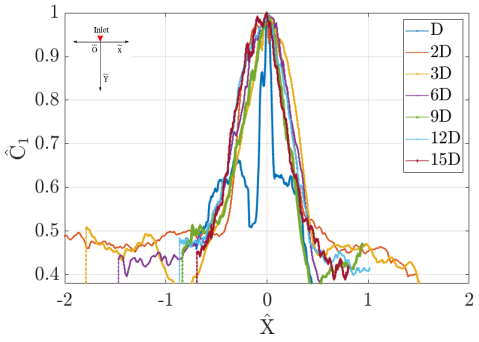

(b) Bottom opening geometry

Figure 3.28: Radial profiles of concentration across the jet axis at an inlet flow rate = $1.265lpm(Re = 3700)$

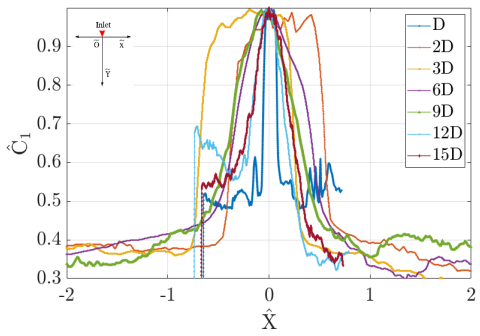

(a) Side opening geometry

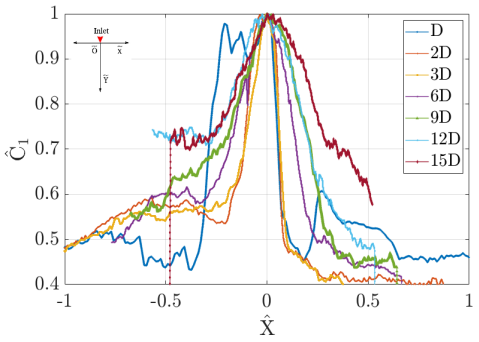

(b) Bottom opening geometry

Figure 3.29: Radial profiles of concentration across the jet axis at an inlet flow rate = $0.88lpm(Re = 2600)$

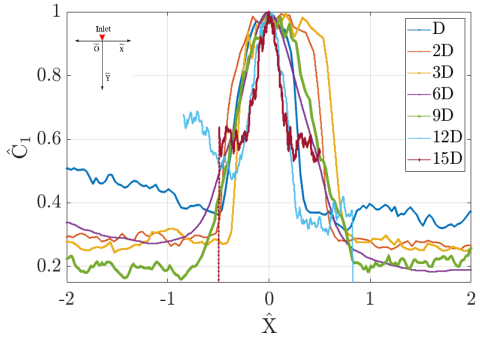

(a) Side opening geometry

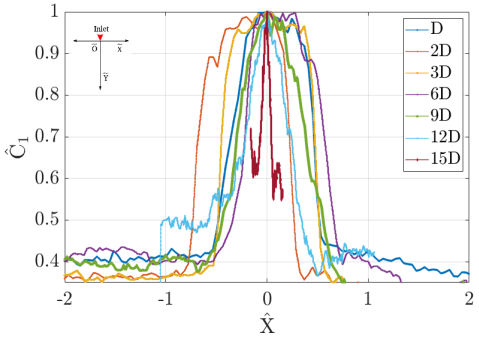

(b) Bottom opening geometry

Figure 3.30: Radial profiles of concentration across the jet axis at an inlet flow rate = $0.489lpm(Re = 1500)$

3.8.3 Correlations

Reynolds Stress

Velocity fluctuations were extracted from PIV data after suitable averaging. Cross sectional profiles of Reynolds stress values at different axial locations were plotted for different experiments. The Reynolds stress ($\overline{U'V'}$) is a symmetric tensor that decides the mean transport of fluctuating momentum in one direction by velocity fluctuations in the other direction. A higher value of Reynolds stress shows strong correlations between the velocities in either directions.

In the Reynolds stress plots, the positive and negative portions relate to the magnitude and direction of entrainment. The larger magnitudes of Reynolds stress clearly confirms the entrainment model described by MTT [39]. It can be taken as an indicator of the intensity of mixing. The value is highest for confinement with a side opening at $Re = 3700$ (Fig. 3.31). The values of Reynolds stress is lesser for confinement with bottom opening at the same Reynolds number. The values of Reynolds stress get reduced by an order of magnitude for the low Reynolds number cases (Fig. 3.33). The value of Reynolds stress for jet flow in confinement with a bottom opening is always less than jet flow in confinement with a side opening. The plots also shows that the correlation is zero at the jet centreline (jet-core). The horizontal axis is normalized by diameter of inlet, D ($\hat{X} = X/D$)

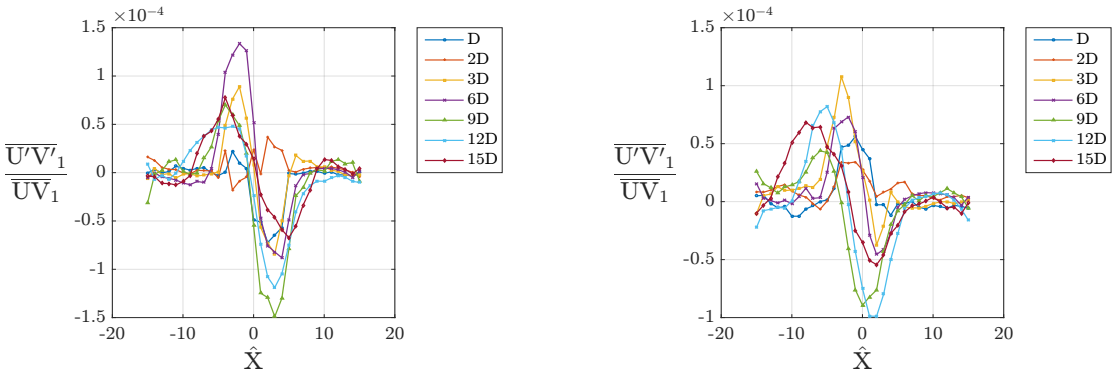

(a) Side opening geometry

(b) Bottom opening geometry

Figure 3.31: Cross section plots of Reynolds Stress for jet with an inlet flow rate = $1.265 lpm$ ($Re = 3700$)

The Reynolds stress decides the exchange of momentum between the turbulence and the mean flow even though the turbulent velocity fluctuations have zero mean momentum. The low inlet Reynolds number experiments have smaller values for Reynolds stress which matches with the mixing patterns observed. The side opening cases have higher values for Reynolds stress over the bottom opening cases.

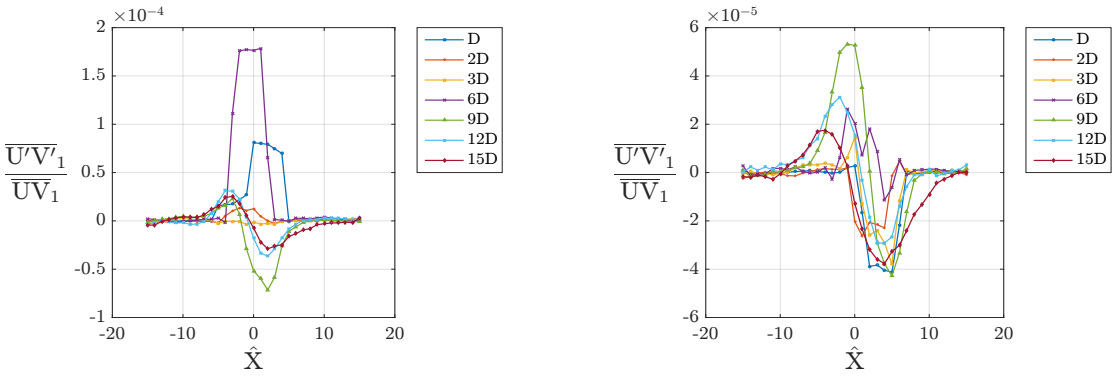

(a) Side opening geometry (b) Bottom opening geometry

Figure 3.32: Cross section plots of Reynolds Stress for jet with an inlet flow rate = $0.88lpm$ ($Re = 2600$)

The large, trapped eddies were evident in the jet flow cases with $Re = 3700$. The size of these eddies at the near-wall region was almost the gap between the jet and the near-wall. Therefore the jet-wall interactions and hence fluctuations in velocities are higher in this region causing high values of Reynolds stress (Fig. 3.31) in the near-wall region whereas in the case of $Re = 2600$ (Fig. 3.32) and $Re = 1500$ (Fig. 3.33), the values of Reynolds stress are lower on the near-wall region possibly due to smaller size of the eddies compared to the gap between the jet and the near-wall.

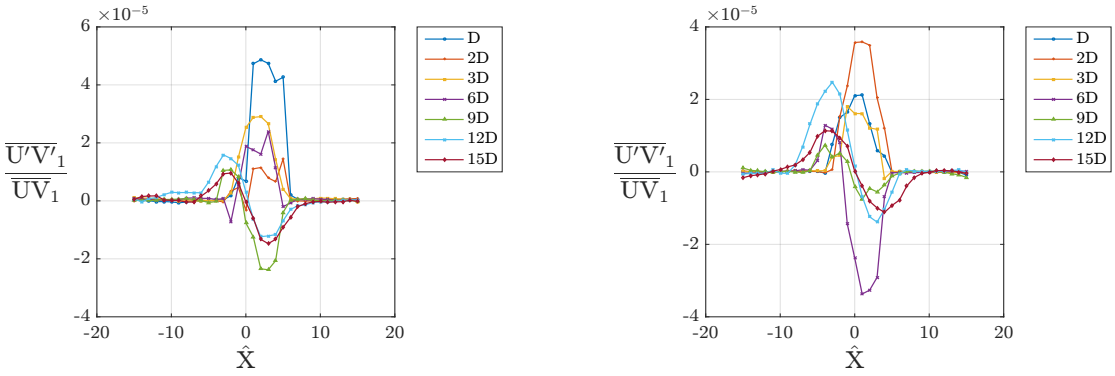

(a) Side opening geometry (b) Bottom opening geometry

Figure 3.33: Cross section plots of Reynolds Stress for jet with an inlet flow rate = $0.489lpm$ ($Re = 1500$)

The jet flow cases with higher Reynolds number ($Re = 3700,\ 2600$) have larger values of Reynolds stress at the far-wall side possibly due to the bidirectional flow from the side opening. In the jet flow case with $Re = 1500$, the entire fluid inside the confinement was not turbulent and stable stratification was also observed. The Reynolds stress values in this case are similar in the side and bottom opening flow cases.

Velocity-Concentration correlations

The axial velocity-concentration correlations were also studied and it was observed that the values are higher for confinement with side opening compared to the confinement with bottom opening (Fig. 3.34). The axial velocity and concentration in flow cases with confinement with side opening at $Re = 2600$ (Fig. 3.35a) has higher correlations than bottom opening cases with higher Reynolds number ($Re = 3700$) (Fig. 3.34b).

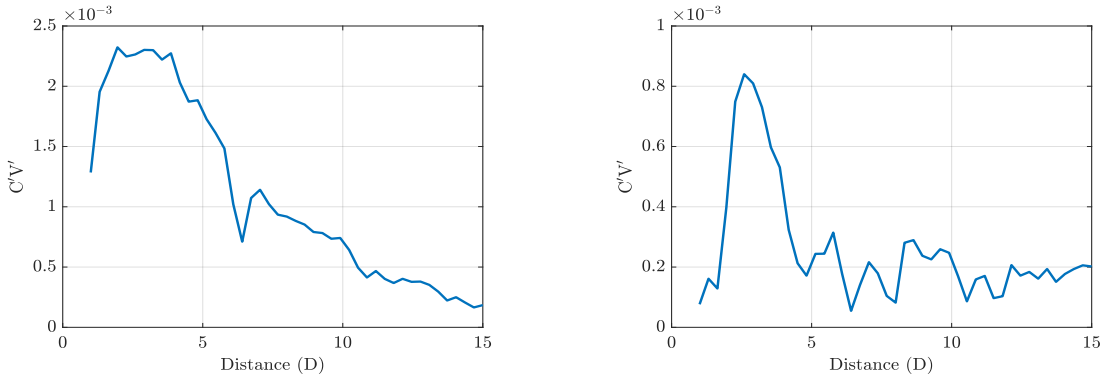

(a) Side Opening Geometry (b) Bottom Opening Geometry

Figure 3.34: Velocity-Concentration correlation for confinement with side and bottom opening (flow rate $= 1.265lpm$, $Re = 3700$, $t = 5 - 50s$)

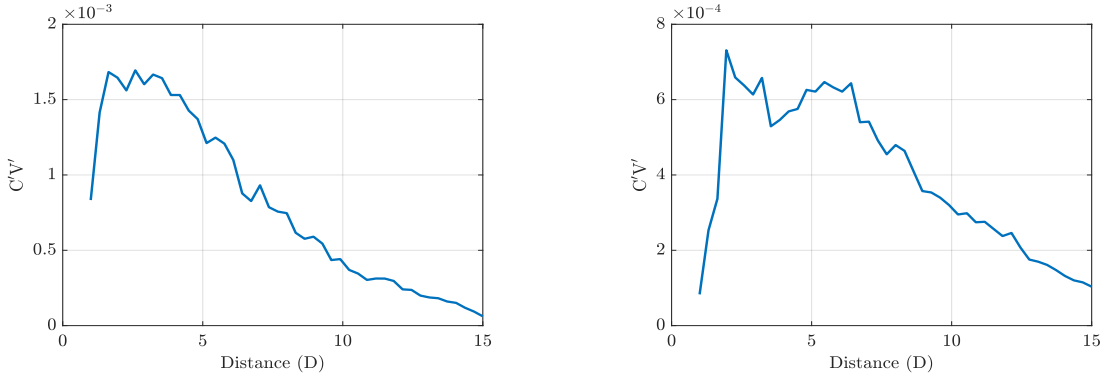

(a) Side Opening Geometry (b) Bottom Opening Geometry

Figure 3.35: Velocity-Concentration correlation for confinement with side and bottom opening (flow rate $= 0.88lpm$, $Re = 2600$, $t = 5 - 50s$)

It shows that the changes in velocity and concentration affect each other more dominantly in the confinement with side opening. In the flow cases described in the study, the confinement geometry appears to be a more important factor in mixing than the jet flow rate.

3.8.4 Centreline profiles of velocity and concentration

The centreline profile plots of normalized axial velocity, axial velocity fluctuations, concentration and concentration fluctuations were plotted for all flow rates for the jet flow cases in confinement with side opening and bottom opening. The peak of MCS axial velocity was expected to be near an axial distance of $3D$ from the nozzle where D is the nozzle diameter. Previous works in the topic states that the flow would start with a velocity approximately equal to 95% of the peak velocity till an axial distance of $3D$ and decelerates further. The flow gets accelerated when buoyancy forces dominate over the viscous forces due to high density difference or less mixing and less entrainment [29, 20]. The peak velocity was observed when buoyancy balances viscosity. After that point, the jet decelerates, density difference gets reduced and entrainment increases. In the case of axial velocity, it could be observed qualitatively that the jet-core had started decelerating (Fig. 3.36) from an axial distance of $5D$ from the inlet. $\hat{U} = U/U_{max}$, $\hat{V} = V/V_{max}$, $\hat{C} = C/C_{max}$, $\hat{Y} = Y/D$ where U, V, C represent the mean or rms values of radial velocity, axial velocity and concentration respectively.

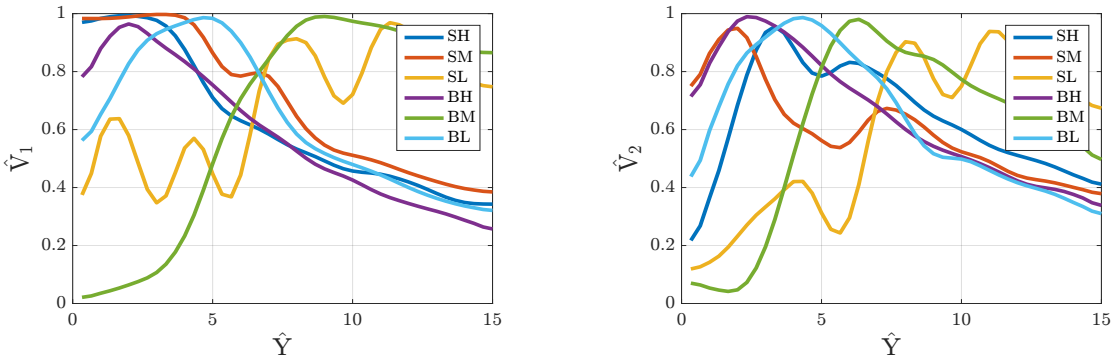

(a) $t = 5 - 50s$ (b) $t = 245 - 290s$

Figure 3.36: Centreline profile of axial velocity (**S**: side opening, **B**: bottom opening, **H**: flow rate $= 1.265lpm, Re = 3700$, **M**: flow rate $= 0.88lpm, Re = 2600$, **L**: flow rate $= 0.489lpm, Re = 1500$)

The plots of rms of velocity fluctuations show that the axial velocity fluctuations does not vary with time possibly due to the steady supply of incoming fluid inside the confinement and the relative strength of the momentum flow over the buoyancy induced secondary flows (small density difference) (Fig. 3.37). During time $t = 5 - 50s$ and $t = 245 - 290s$, the trend is similar in pattern and magnitudes of rms values. Due to confinement at the bottom, the axial velocity fluctuations die down to lower values for all time instants. The values at an axial distance of $15D$ are almost identical for same flow rate cases. There is also a clear difference in the axial velocity fluctuations for the high flow rate case compared to other cases.

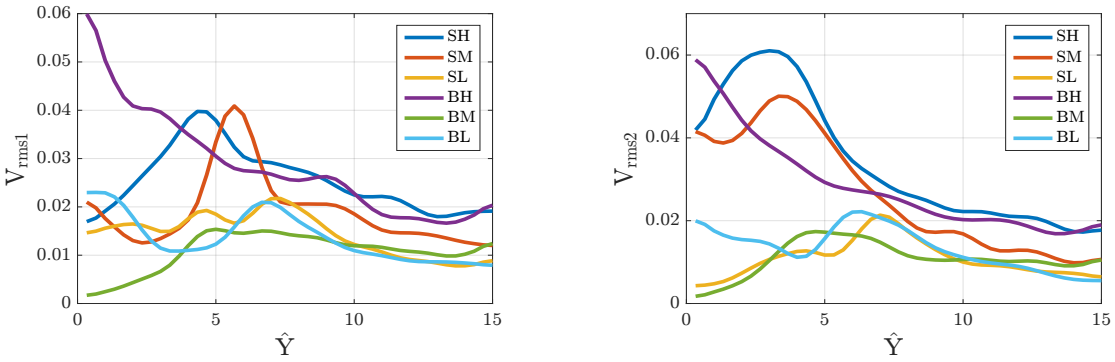

(a) $t = 5 - 50s$ (b) $t = 245 - 290s$

Figure 3.37: Centreline profile of rms of fluctuations of axial velocity (**S**: side opening, **B**: bottom opening, **H**: flow rate = $1.265lpm$, $Re = 3700$, **M**: flow rate = $0.88lpm$, $Re = 2600$, **L**: flow rate = $0.489lpm$, $Re = 1500$)

The radial velocity profiles fluctuate in both magnitude and direction indicating entrainment and mixing (Fig. 3.38). The high flow rate cases have higher fluctuations in radial velocity compared to other cases. The radial velocity fluctuations at an axial distance of $15D$ from the inlet are different for various cases unlike the axial velocity. This is an indication of the difference in entrainment and mixing between the side and bottom opening cases.

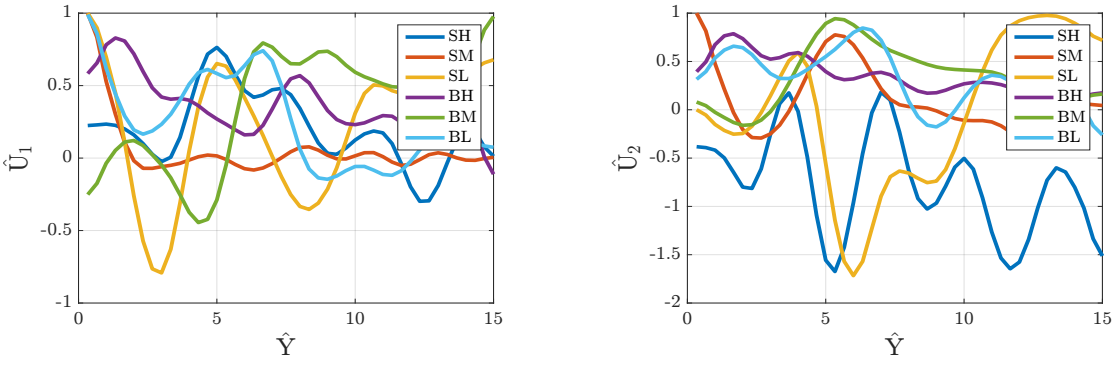

(a) $t = 5 - 50s$ (b) $t = 245 - 290s$

Figure 3.38: Centreline profile of radial velocity (**S**: side opening, **B**: bottom opening, **H**: flow rate = $1.265lpm, Re = 3700$, **M**: flow rate = $0.88lpm, Re = 2600$, **L**: flow rate = $0.489lpm, Re = 1500$)

Looking at the centreline profiles of rms fluctuations of radial velocity (Fig. 3.39), it can be observed that the fluctuations increase with increase in flow rate. Larger fluctuation means higher entrainment and mixing. For same flow rate cases, the difference in radial velocity fluctuations between side and bottom opening cases reduces from $t = 5-50s$ to $t = 245 - 290s$ possibly due to the reduction in density gradient.

From the normalized profiles of concentration, it could be observed that the mixing

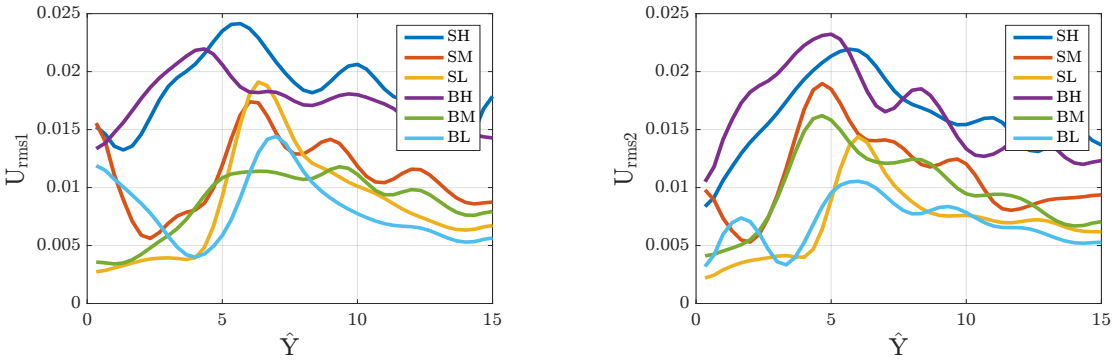

(a) $t = 5 - 50s$ (b) $t = 245 - 290s$

Figure 3.39: Centreline profile of rms of fluctuations of radial velocity (**S**: side opening, **B**: bottom opening, **H**: flow rate = $1.265lpm$, $Re = 3700$, **M**: flow rate = $0.88lpm$, $Re = 2600$, **L**: flow rate = $0.489lpm$, $Re = 1500$)

pattern is nearly similar for all cases between the axial location $5D - 10D$ from the inlet (Fig. 3.40). This is the region where most of the eddies caused by the jet-bottom wall interaction comes in contact with the jet again. There was a drop in the concentration level after a distance of $10D$ from the inlet, which could be a consequence of the presence of unmixed cores of large eddies in this region.The size of these large eddies does not vary with time as it is a case of forced turbulence for the time duration of the experiments. But the fluctuations in concentration increases with the axial distance from inlet due to the presence of eddies near the bottom plate.

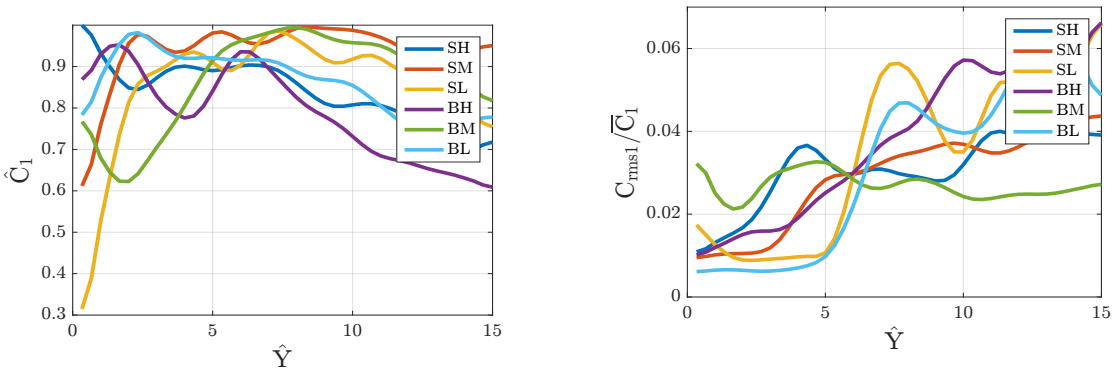

(a) Mean centreline concentration ($t = 5 - 50s$) (b) Centreline profile of fluctuation in concentration ($t = 5 - 50s$)

Figure 3.40: Centreline concentration ($t = 5 - 50s$) (**S**: side opening, **B**: bottom opening, **H**: flow rate = $1.265lpm$, $Re = 3700$, **M**: flow rate = $0.88lpm$, $Re = 2600$, **L**: flow rate = $0.489lpm$, $Re = 1500$)

Chapter 4

Entrainment and Mixing

Eckart [19] states that turbulent mixing comprises of three stages, which span over the complete space-time spectrum of the flow - entrainment, dispersion and diffusion. Entrainment could be considered as the most important property of turbulent flows. Entrainment is the transport of fluids across an interface between fluid domains caused by shear induced turbulent flux, over a spectrum of scales of considerable span. In the case of jets, the sharp velocity gradient causes shear regions at the jet edges which leads to the generation of turbulence. Entrainment decides the transport and mixing in turbulent flows which is evident in high Reynolds number flows.

The velocity of the entraining fluid is called entrainment velocity; the ratio between the relevant length and time scales. Morton, Turner and Taylor presented a successful model for entrainment where they argued that the entrainment velocity must be proportional to the effective speed of the flow [39]. Previous works of Breidenthal [46] show factors like confinement, stratification, rotations and acceleration can affect entrainment. The works of Brown and Roshko [9] and Konrad [32] states that entrainment and associated transport and mixing are decided mainly by the largest vortices which makes the sizes of these eddies the relevant length scales and their period of rotation the relevant time scales. Thus, the entrainment velocity could be defined as

$$v_e = \kappa . \left(\frac{\zeta}{\tau} \right) \tag{4.1}$$

where ζ is the size of the largest eddies, τ is the period of rotation of the largest eddies and κ is the constant of proportionality. *Eddy turnover time*, $t_l, (t_l = L/u_l)$ is the typical time scale for an eddy of length scale L to undergo "significant distortion" [55]. Transfer of energy occurs through these distortions and thus t_l is also the time scale for the energy transfer from larger to smaller scales. The ratio between the length scale and time scale of eddies also provides the characteristic velocity (V_{rms}) for turbulent flows. Experiments were conducted on free jet and confined jet flows at different density ratios to understand

the pattern of entrainment and subsequent mixing. The mixing also leads to further reduction in momentum. The entrainment was initiated by the largest eddies and the phases later dispersed and got mixed by the full spectrum of smaller scales. The works of Roshko [47] explains that the further mixing caused by smaller eddies is proportional to the large eddies and occurs at smaller time scales. Thus, the net flow process is controlled by the large eddies and only their length and time scales matter. Thus, it could be stated that the effect of buoyancy would be higher on the largest length scales.

4.1 Free jet

An axi-symmetric free/unconfined jet has a linear rate of spread in the lateral direction and the jet centreline velocity varies inversely with the axial distance. The entrainment region caused by turbulent eddies increases in size with the size of these eddies downstream. The infinite volume of fluid around the jet axis creates a uniformly inward pattern of entrainment around it. The free jet in the experiments conducted was a statistically steady jet whereas the jet in confinement was a statistically unsteady (decelerating) jet. The mode of entrainment in free jet for two cases ($\rho = 0kg/m^3$ and $\rho = 5kg/m^3$) is presented in Fig. 4.1 for an axial distance of $0 - 15D$ from the inlet ($Re = 2600$).

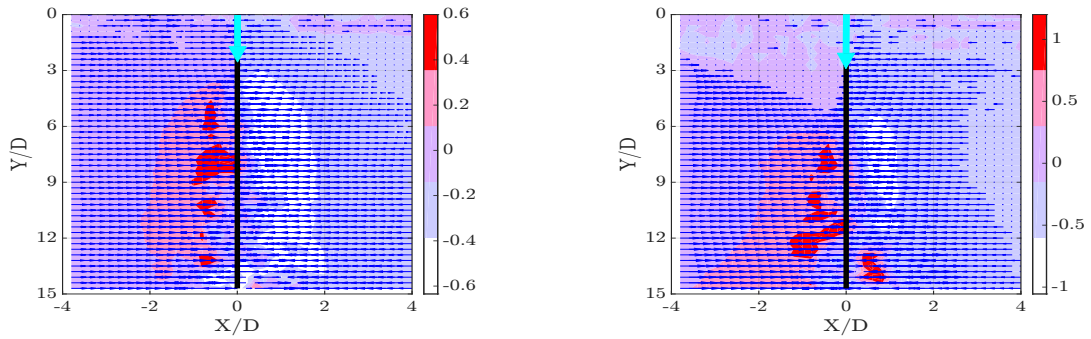

(a) $\Delta\rho = 0kg/m^3$ (b) $\Delta\rho = 5kg/m^3$

Figure 4.1: Entrainment (radial) velocity pattern around the jet centreline in unconfined jet flow cases. The black vertical line represents the jet centreline. The root of the cyan arrow shows the location of the source of the jet and its direction shows the direction of the jet. The contour plots represent the magnitude of entrainment velocity and arrows shows its direction. It can be observed that on either side of the centreline, the entrainment velocity is directed towards the centreline. The pattern is smooth and continuous. The vector plots show a regular pattern of entrainment of the ambient fluid by the jet towards its centreline (averaged over $t = 10s - 15s$).

The same trend is observed in different time periods in the time frame $0 - 290s$. In this near-field region, the vortices are relatively smaller and they get translated along

the mean jet flow. The factors that affect entrainment in incompressible flows include acceleration, confinement, stratification and stationarity of vortices [46].

4.2 Jet in confined space

There are significant differences in the jet hydrodynamics of a confined jet compared to that of a free jet due to the recirculation caused by entrainment and wall interactions. The abrupt reduction in the axial velocity of the jet due to walls contributes to changes in its radial velocity profile and affects the pattern of entrainment. The pattern of entrainment for a free jet and confined jet with $\Delta\rho = 5kg/m^3$ from $0-17D$ is shown in Fig. 4.2 ($Re = 2600$). Compared to a free jet where a significantly larger volume of fluid is available for entrainment, there is only a finite volume of fluid to interact for the confined jet and the confinement enforces circulation zones inside it to compensate the fluid transported by the eddies, which alters the pattern of entrainment. It could be observed from the change in sign of the entrainment velocity on either sides of the $2D$ plane along the axial direction. The presence of confinement will increase the shear rate, adding more interfacial areas and turbulence which help in mixing.

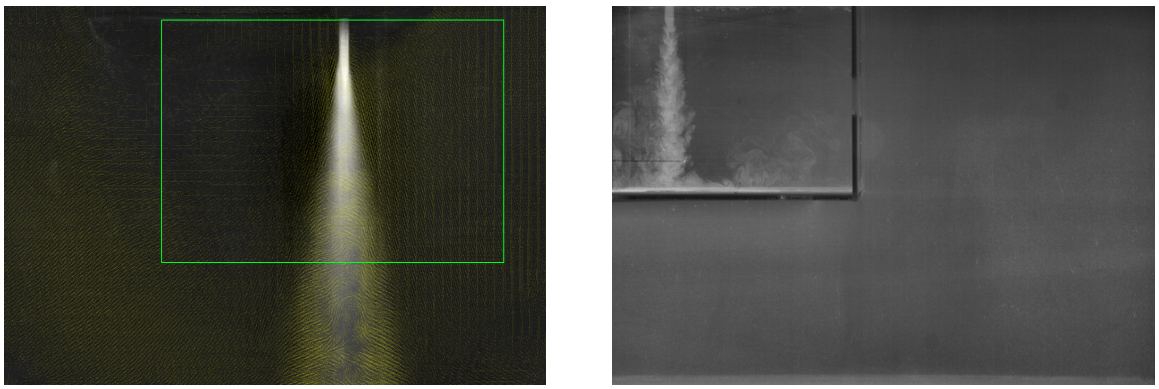

(a) Unconfined jet (b) Confined jet with a side opening

Figure 4.2: Difference in flow structures between an unconfined buoyant jet and a confined buoyant jet for a $\Delta\rho = 5kg/m^3$ between the jet and the ambient fluid. The confined jet creates trapped eddies that increase mixing inside the confinement.

In a pure jet, with the spreading of the shear layer, the unmixed jet-core disappears gradually whereas in the case of a confined jet, the unmixed jet-core disappears at a shorter length due to the abrupt change in the direction of the axial flow of the jet-core caused by the bottom wall of the confinement normal to the flow. Thus, along with the mixing due to shear layers, the bottom wall of the near-field confinement also causes mixing of the jet-core at a lesser axial span. The trapped eddies also play a significant role in the pattern of mixing, especially at the near-wall region.

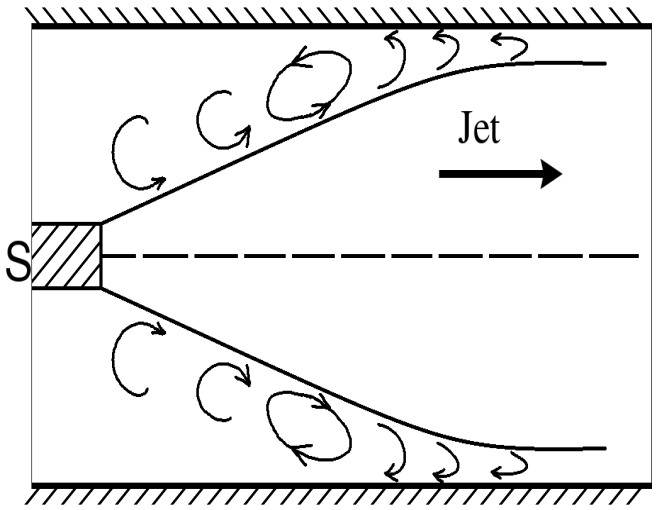

Figure 4.3: The pattern of circulation and entrainment in the case of a confined jet. The jet source (S) is placed at the left side of the figure. The trapped eddies cause vigorous mixing in the confinement. Compared to an unconfined jet that *entrains and transport away* the ambient fluid in the axial direction, the confined jet *entrains and mixes the surroundings* inside the confinement.

The entrainment rate and subsequent mixing depend on the stationarity of the vortices also. The confinement in the experiments was close to the jet centreline on its three sides, which causes the eddies to persist throughout the flow of the jet. The recirculation zones created by the confinement reverses the radial flow directions at different axial positions as shown in Fig. 4.3. Thus, in the experiments, the continuous jet and, the confinement creates persistent vortices that increase mixing. The vortical structures, namely the counter-rotating vortical pairs (CVP) play a significant role in the entrainment between the cross flow and transverse jet. Mean entrainment plots over an eddy turnover time ($5s$) were taken at different time instants and were found similar.

In Figure 4.4, it can be observed that the pattern of entrainment is different for the jet flow in confinement with a side opening and the jet flow in confinement with a bottom opening at $Re = 3700$. The entrainment velocities have higher magnitude for side opening cases compared to the bottom opening cases. The pattern of entrainment in side opening case has more deviation from the entrainment pattern in free jet compared to that of the bottom opening case. The entrainment velocity changes direction frequently in the side opening case.

The entrainment velocity is larger for jet flow in confinement with a side opening compared to a jet flow in confinement with a bottom opening (Fig 4.5). But unlike the side and bottom opening cases with $Re = 3700$, the pattern of entrainment are similar in the side and bottom opening cases at $Re = 2600$.

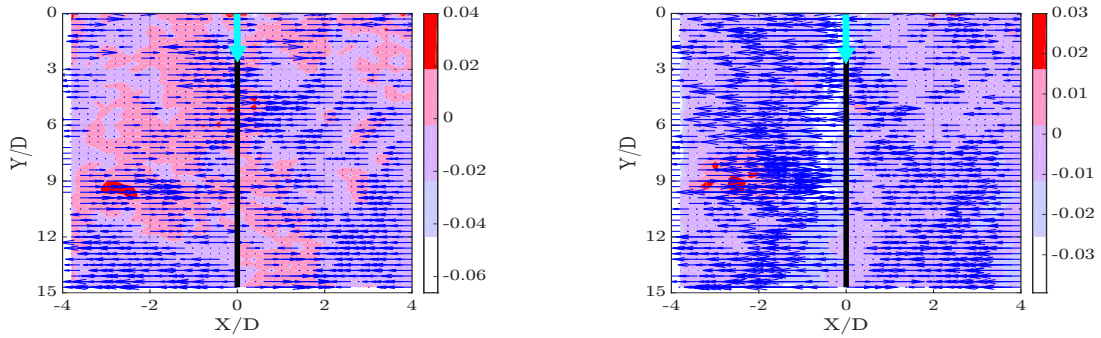

(a) Side opening geometry

(b) Bottom opening geometry

Figure 4.4: Entrainment (radial) velocity pattern around the jet centreline in a confined jet for a jet inflow rate = $1.265lpm$ ($Re = 3700$). The black vertical line represents the jet centreline. The root of the cyan arrow shows the location of the source of the jet and its direction shows the direction of the jet. Both the vector and contour plots represent the entrainment velocity (averaged over $t = 10s - 15s$).

The pattern and values of entrainment velocity are having higher match for side and bottom opening cases at $Re = 1500$ (Fig 4.6). Similar patterns of stratification was also observed at this Reynolds number for side and bottom opening cases. Statistically unsteady, confined jet was used in various cases for improving mixing through increased entrainment. The variation in the axial velocity of the jet contribute to fluctuations in the radial velocity components, increase turbulence and leads to enhanced mixing. The enhancement in entrainment due to the deceleration of jet is employed in the increased mixing of diesel jets in compression-ignition engines. The concentration of the jet along the centreline also reduces with increase in the fluctuations in the axial velocity of the jet.

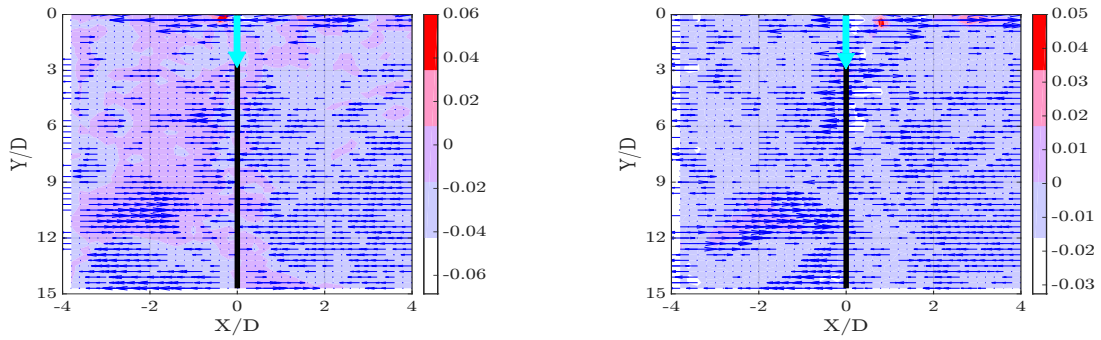

(a) Side opening geometry

(b) Bottom opening geometry

Figure 4.5: Entrainment (radial) velocity pattern around the jet centreline in a confined jet for a jet inflow rate = $0.88lpm$ ($Re = 2600$). The black vertical line represents the jet centreline. The root of the cyan arrow shows the location of the source of the jet and its direction shows the direction of the jet. Both the vector and contour plots represent the entrainment velocity (averaged over $t = 10s - 15s$).

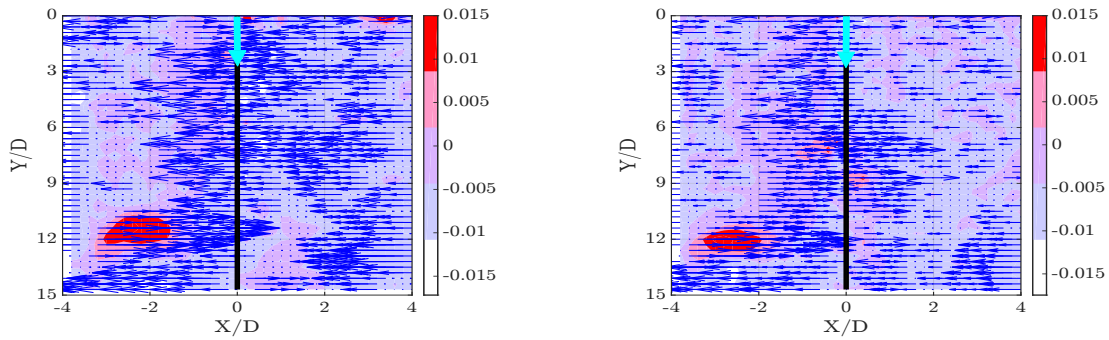

(a) Side opening geometry

(b) Bottom opening geometry

Figure 4.6: Entrainment (radial) velocity pattern around the jet centreline in a confined jet for a jet inflow rate = $0.489lpm$ ($Re = 1500$). The black vertical line represents the jet centreline. The root of the cyan arrow shows the location of the source of the jet and its direction shows the direction of the jet. Both the vector and contour plots represent the entrainment velocity (averaged over $t = 10s - 15s$).

The buoyant jet in the experiment is flowing through an asymmetric confinement (Fig. 4.7). The vertical wall of the confinement away from laser and normal to it, is nearer ($\sim 7D$) to the jet centreline (denoted as *near-wall region, B*) than the wall near to the laser ($\sim 20D$) and normal to it (denoted as *far-wall region, A*). Therefore either sides of the jet were analysed separately to see the patterns of entrainment. The figures given below show the variation of mean vertical velocity and mean concentration profiles in the near-field the jet in the axial direction at the near-wall region and the far-wall region respectively for different time instants. The profiles are normalized by their peak values. Fig. 4.8 - 4.13 shows the variation in mean velocity and mean concentration at the near and far-wall regions ($4D$ wide) of the jet for high Re case with side opening ($t = 5.1s - 45.1s$).

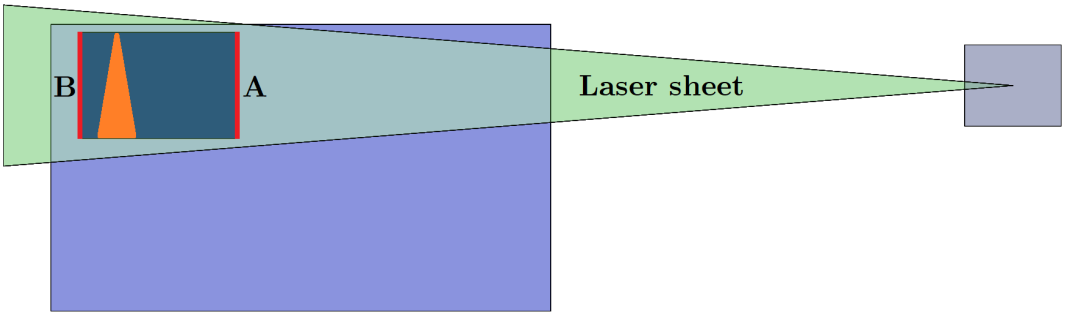

[h]

Figure 4.7: Schematic of the experiment set up. The sides A and B which are normal to the laser sheet are marked. A is the side near to the laser and B is the side far from the laser.

It could be clearly observed that the radial velocity values for the near-wall region fluctuate more with the distance from the inlet whereas the radial velocity profiles on the region near the jet away from the side wall does not exhibit any dependence with the distance from inlet. The entrainment and subsequent mixing is also higher in the *near-wall region* compared to the region on the *far-wall region*. The presence of walls cause higher entrainment at the *near-wall region* which causes a smaller standard deviation for the concentration values. On the *far-wall region*, the entrainment and subsequent mixing is lesser in the beginning upto an axial distance of $5D$ but later becomes comparable to *near-wall region*. The presence of a side opening also contributes to the radial velocity fluctuations and concentration but this flow falls under buoyancy driven convection and hence slower compared to the jet flow.

The effect of a rigid boundary at the *near-wall region* is clearly observed in the other side opening cases with lesser flow rate ($0.88lpm, Re = 2600$ and $0.489lpm, Re = 1500$). All these cases with different flow rate follow the same trend of increased radial velocity

fluctuation with axial distance from the jet inlet. The *far-wall region* shows no regular pattern for velocity in the side opening cases. In all the side opening cases with different flow rates, it could be observed that the proximity of the rigid wall creates a higher concentration at the *near-wall region* compared to the *far-wall region*. At low flow rate cases, there is less turbulence, no large eddies or significant interaction with the wall, which means there is less entrainment. The variation at the *far-wall region* could be attributed to the bidirectional flow through the side opening. The concentration profiles appear nearly similar on either sides of the jet which means mixing occurs mainly due to molecular diffusion.

The pattern of velocity and concentration profiles at the *near-wall region* and *far-wall region* are different for bottom opening cases. The radial velocity profiles at the *near-wall region* has lesser fluctuations near the jet inlet compared to side opening cases.

For side opening case at $Re = 3700$, the fluctuations in the radial velocity are higher at the *near-wall* side compared to the *far-wall* side. The concentration values are also higher in the *near-wall* region compared to the *far-wall* region after an axial distance of $10D$ (Fig. 4.8). For bottom opening cases at $Re = 3700$, the radial velocity has higher fluctuations at the *near-wall* region. But the concentration is higher at the *far-wall* region (Fig. 4.9).

In the case of side opening confinements at $Re = 2600$ (Fig. 4.10), the radial velocity fluctuations are higher at the *near-wall* region especially at the bottom due to trapped eddy. But the concentration values are higher at the *far-wall* region. For bottom opening cases at $Re = 2600$, the velocity fluctuations are higher at the *near-wall* region. The concentration values are higher at the *far-wall* region similar to the side opening case with same Reynolds number (Fig. 4.11).

In the case of $Re = 1500$, the velocity patterns are similar at the *near-wall* and *far-wall* regions for both side and bottom opening cases. The concentration pattern on either sides of the jet are similar for side opening (Fig. 4.12) and bottom opening (Fig. 4.13) cases but the values are higher for side opening cases.

Therefore it can be observed that the inlet Reynolds number decides the flow and mixing patterns more than the geometry. At $Re = 1500$, the flow and mixing patterns were similar for both side and bottom opening cases. The effect of geometry comes into picture only at higher Reynolds numbers. There are higher probability for stratifications in the *far-wall* region compared to the *near-wall* region due to weaker eddies.

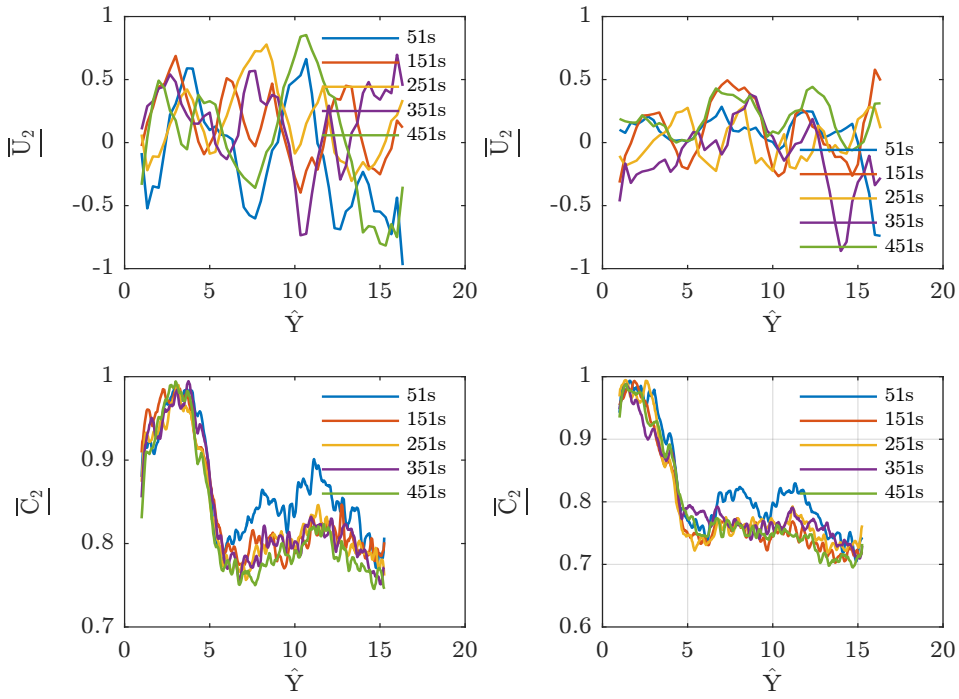

Figure 4.8: Mean radial velocity and mean concentration at the near-wall (left) and far-wall (right) regions for confined jet, side opening, inlet flow rate = $1.265 lpm (Re = 3700)$

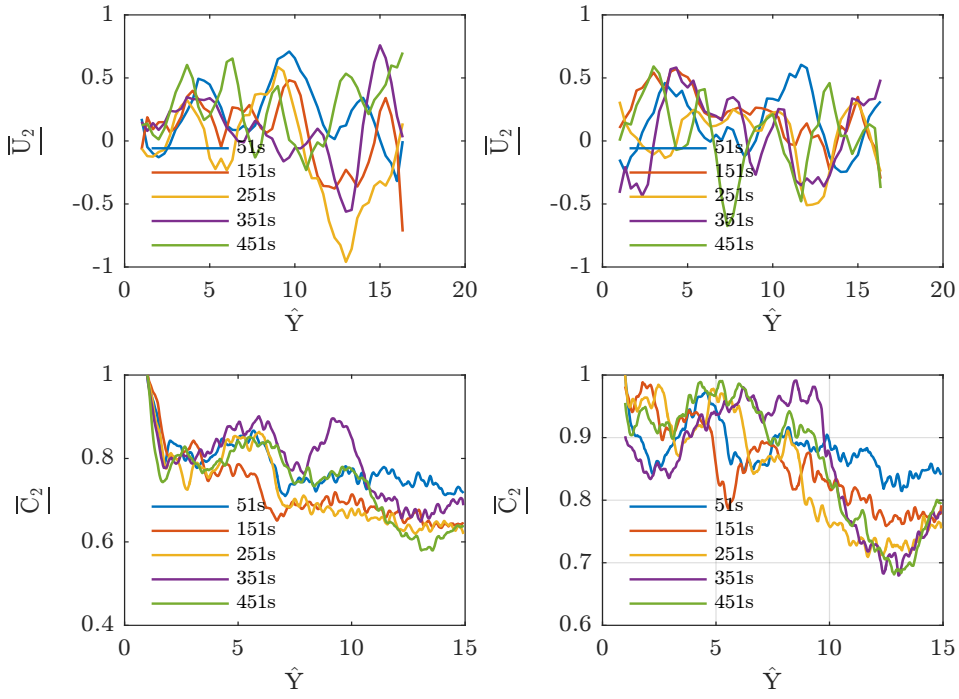

Figure 4.9: Mean radial velocity and mean concentration at the near-wall (left) and far-wall (right) regions for confined jet, bottom opening, inlet flow rate = $1.265 lpm (Re = 3700)$

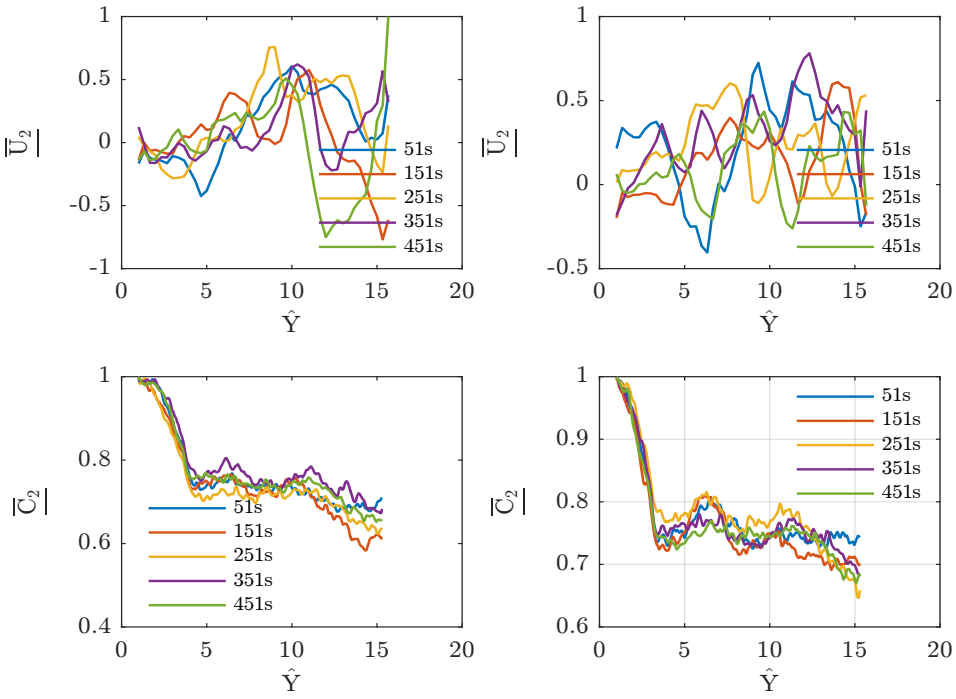

Figure 4.10: Mean radial velocity and mean concentration at the near-wall (left) and far-wall (right) regions for confined jet, side opening, inlet flow rate = $0.88lpm(Re = 2600)$

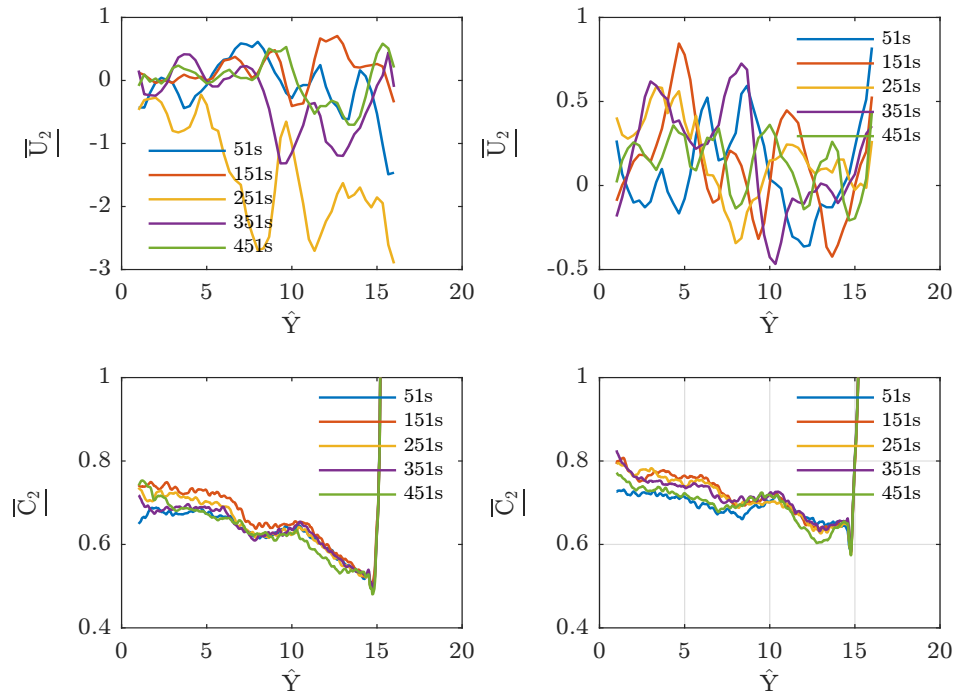

Figure 4.11: Mean radial velocity and mean concentration at the near-wall (left) and far-wall (right) regions for confined jet, bottom opening, inlet flow rate = $0.88lpm(Re = 2600)$

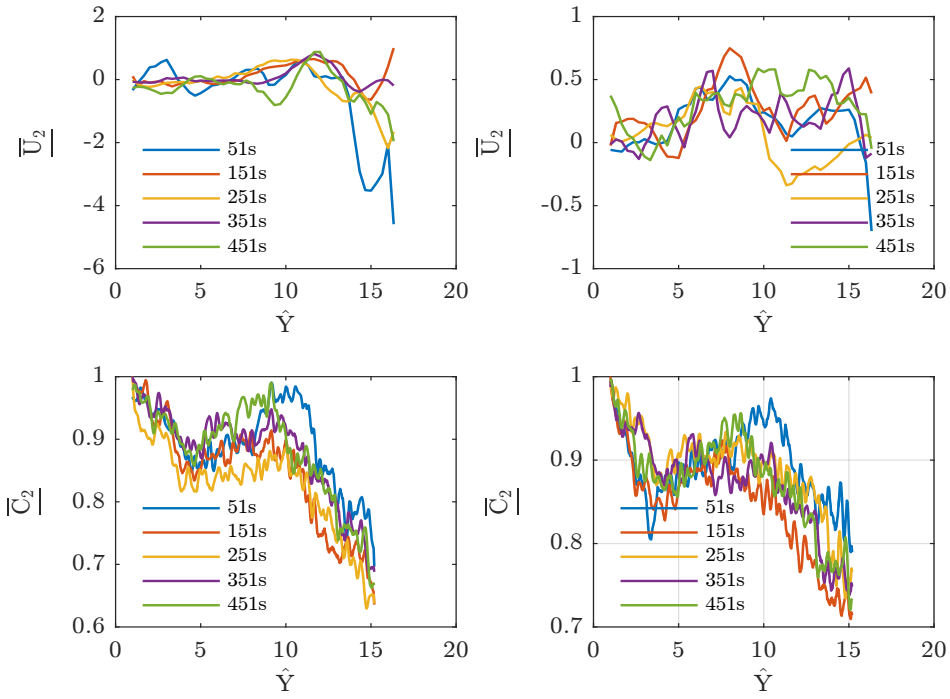

Figure 4.12: Mean radial velocity and mean concentration at the near-wall (left) and far-wall (right) regions for confined jet, side opening, inlet flow rate = $0.489 lpm (Re = 1500)$

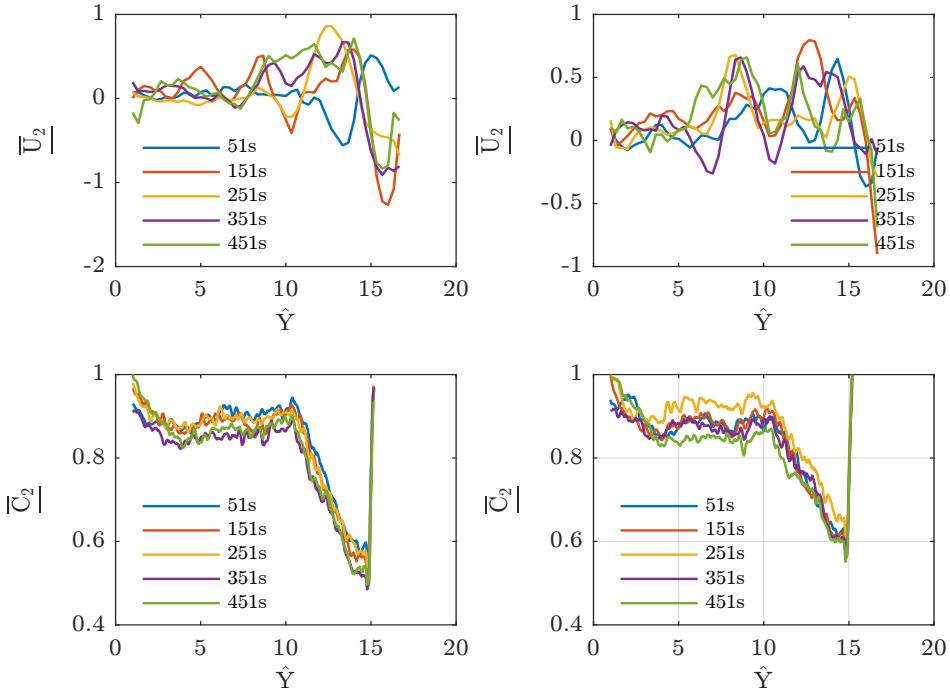

Figure 4.13: Mean radial velocity and mean concentration at the near-wall (left) and far-wall (right) regions for confined jet, bottom opening, flow rate = $0.489 lpm (Re = 1500)$

4.3 Coefficient of entrainment

The entrainment coefficient, α was calculated for all experiments for the bottom and side opening cases according to 1.10. On either side of the jet, the radial locations were identified where the local axial velocity becomes $1/e$ times the axial velocity at the centreline of the jet. Since the left and right side of the jet has different distance of separation from the wall, the entrainment values are calculated for both the walls nearer and farther from the laser and normal to it.

The coefficient of entrainment is higher near the inlet and reduces downstream. The values of entrainment coefficient approaches a value between that of vertical free jet (0.08) and vertical, buoyant free plume (0.12) after an axial distance of $10D$. The overall trend in the variation of entrainment coefficient is from higher value at the beginning of the flow to lower values towards the far-field. This is consistent with the theory that the entrainment coefficient is proportional with the mean centreline velocity.

The near-wall region of the jet appear to have steady entrainment compared to the far-wall region possibly due to circulation zones caused by trapped eddies. The entrainment values at the far-wall region of jet has higher fluctuation near the inlet compared to the near-wall region. The presence of the wall at one side of the jet aids circulation that cause further rise in entrainment towards the bottom of the confinement whereas there are no such rolling motion at the far-wall region and thus the mixing also is reduced there The side opening of the confinement affects the entrainment at the far-wall region.

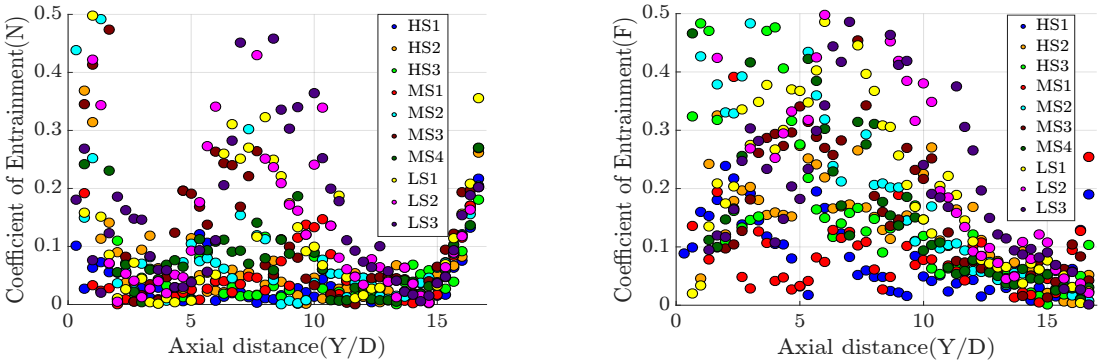

(a) α at the near-wall region of the jet

(b) α at the far-wall region of the jet

Figure 4.14: Entrainment Coefficients - Side opening

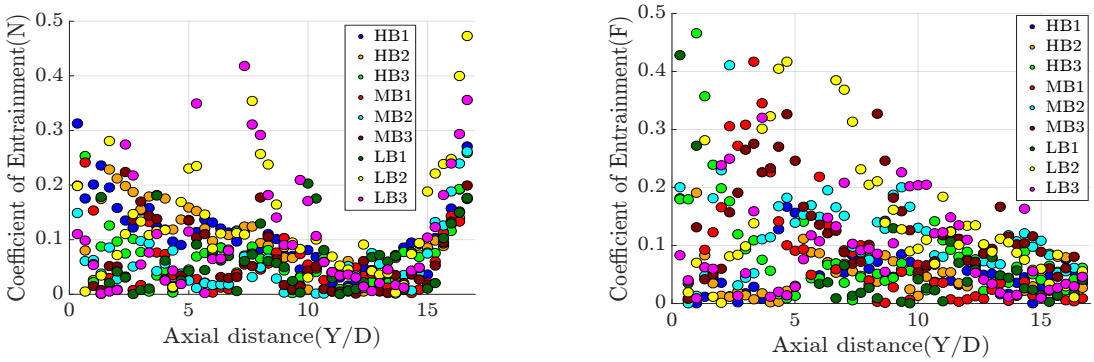

(a) α at the near-wall region of the jet

(b) α at the far-wall region of the jet

Figure 4.15: Entrainment Coefficients - Bottom opening

4.4 Stratification

Entrainment and turbulent mixing cause different flow patterns compared to typical stratification patterns expected from a laminar jet of denser fluid entering a confined space. Stronger stratification near the bottom wall was observed in the low Reynolds number cases ($Re = 1500$) and comparably weaker stratification at the same region in the higher Reynolds number cases ($Re = 2600, 3700$). The jet with low Reynolds number has lesser fluctuations in velocity, aids buoyancy driven stratification and does not cause strong mixing. The mode of stratification was independent of the density difference/buoyancy as different modes of mixing were observed inside the confinement for the same density difference between the incoming and ambient fluids. When the size of the largest eddies were considerably smaller than the box dimensions, strong stratification patterns were visible (Fig. 4.16). The deviation from the expected pattern of *stratification only in bottom opening geometry* [35] and increase in mixing caused by the near-field confinement can be clearly observed in the experiments conducted.

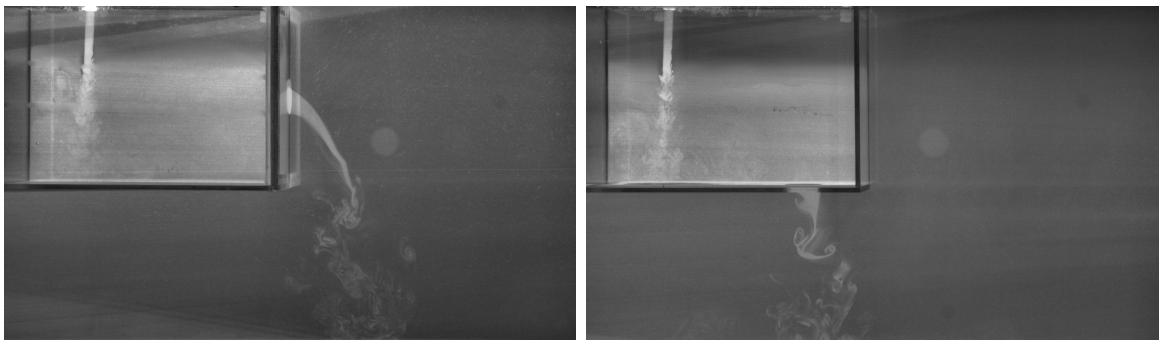

(a) Side opening geometry

(b) Bottom opening geometry

Figure 4.16: Strong stratification pattern and stable neutral level for jet inlet flow rate $= 0.489 lpm$ ($Re = 1500$).

4.5 Difference between confinements with side or bottom opening

In the case of confinement with side opening, the incoming salt solution after mixing, reaches the side opening and starts flowing outside the confinement. This could be taken as a buoyancy driven convection as the flow velocity was considerably less than the buoyant jet. This flow pattern caused by the overflow through the side opening (layer-wise overflow), was evident in the case of jet with low flow rate ($Re = 1500$). Stably stratified layers were observed in this case below the height of the side opening and the outward flow from the confinement was slow [35].

Bidirectional flow was observed at the box outlet in cases with side opening whereas unidirectional outflows were observed in the bottom opening cases. It could be observed that the bottom opening cases have no unmixed, fresh fluid inflow into the confinement compared to the side opening cases [35]. This would lead to higher concentration of the salt solution inside the confinement for the bottom opening cases compared to side opening cases.

The incoming denser salt solution would reach the bottom wall of the confinement due to the initial momentum of the jet and higher density. The mixing en route would be lesser compared to the mixing due to the bottom wall of the confinement. Thus the bottom region of the confinement continuously receives denser fluid, mixes them, makes it lighter and buoys upwards. The bottom opening helps in draining the densest layers to the ambient. But in the case of side opening, the fluid parcels with higher kinetic energy and less concentration reaches the side opening and flow outwards. Thus the bottom opening release out the denser fluid parcels while the side opening release the less denser parcels.

The bidirectional flow in the case of side opening affects the mixing patterns apart from feeding fresh, unmixed fluid. It can be observed that the lighter fluid that enters the confinement via buoyancy driven convection has less velocity and kinetic energy to involve in active mixing. These fluid parcels after entering the confinement immediately occupies the top region and creates a relatively stagnant zone with less salt concentration. They get involved in mixing via the entrainment caused by the incoming jet (Fig. 3.4, Fig. 3.5). The regions of highest vorticity was near the region of entry of the jet into the confinement.

While the incoming jet gets mixed by the confined fluid in bottom opening cases, it gets mixed with less mixed fluid in the case of confinement with side opening. In this way the confinement with side opening effectively reduces the density gradient of the jet fluid from the inlet itself. The rate of mixing inside the tank reduces with time as the concentration gradient inside the box weakens. The rate of increase in concentration inside the confinement would be lesser for side opening cases as the inflow of unmixed ambient fluid prevents the immediate depletion of pure fluid inside the confinement.

Chapter 5

Summary, Conclusion and Future Work

The buoyant jet is a flow that comes between momentum jet and plume or puff. The difference between them is in the continuous supply of mass and momentum. Experiments were conducted on free jet and, confined jet at different inlet Reynolds number and outlet positions. Confinement in near-field $(0 - 17D)$ with side opening and bottom opening geometries were selected to replicate basic wall and floor opening geometries. The buoyant free jet in the experiments exhibited a behaviour similar to vertical non-buoyant jet in open flow domains due to its low density difference/buoyancy but the confined buoyant jet has shown different behaviour in flow evolution. While a free, momentum jet moves with lesser mixing, the mixing in a buoyant jet in confinement is higher due to recirculation zones.

The buoyant jet exhibits an acceleration at the beginning and drops momentum faster due to mixing of components. In the case of a jet hitting a wall perpendicular to the flow, a non-buoyant jet loses energy and spreads uniformly all around. But in the case of a buoyant jet, once the momentum is lost after hitting the wall, the buoyancy driven convection also comes into picture and creates a preferential motion favouring density based stratification.

Self-similar profiles were observed for axial velocity and concentration at different cross sections in the far-field for steady, free, turbulent jet in various experimental studies conducted by others. In the present study, it was observed that there are cases in which axial velocity of the jet and concentration profiles at different cross sections were nearly self-similar in the near-field $(0 - 15D)$, for decelerating, confined, turbulent jet also. Difference in flow and mixing patterns were observed in the case of side and bottom opening cases. The side opening geometry effectively reduces the density gradient between the salt solution and ambient fluid near the jet inlet. The bottom opening geometry

selectively flushes out the bottom, denser layers of fluid. Thus, even with fluids with same density difference, the largest effective density difference inside the confinement can arise in the case of confinement with a side opening compared to that of a confinement with bottom opening.

5.1 Velocity and concentration profiles

From the normalized, mean centreline profiles of velocity and concentration of the decelerating, buoyant confined, turbulent jet in experiments, it can be observed that they are nearly self-similar like a steady, turbulent, free jet and it was observed inside a confinement of maximum axial dimension of $17D$ which falls in the near-field of the jet. The self-similar character shows the loss of memory of initial state of the flow. This finding matches with the findings of of Dong-hyuk Shin et.al [18]. Most of the kinetic energy of the turbulent jet is associated with the large scale structures. Thus there is a difference in the pattern of mixing in the near-field with large structures and at the far-field. The length of the unmixed jet-core/laminar length is related to the span of near-field of the jet. In the present experiments, it can be observed that in the cases with higher self-similarity for axial velocity values at different cross sections, the unmixed jet-core is minimal which indicates the beginning of fully developed flow from a shorter axial span.

Analysing the pattern of mixing near and away from the inlet, the mean near-inlet concentration is nearly $1.5times$ of the mean concentration away from inlet. The results from this study may be used for the design of buildings where room height falls within the near-field of a possible source of buoyancy like a gas leakage or local fire.

The flow patterns in low Reynolds number cases are simpler where stable stratification patterns were observed. It can be observed that at low Reynolds number ($Re = 1500$), there is less difference in flow and mixing between the side and bottom opening flow geometries. In the case of experiments in confinement with side opening, the height of neutral level reaches till the bottom portion of side opening. The less kinetic energy in the low Reynolds number flows reduces the number of eddy turnovers that negatively affects mixing. In the case of high Reynolds number flows, the higher kinetic energy leads to more number of eddy turnovers and a larger spectrum of energy cascade which causes violent mixing.

The low Reynolds number flows reach a steady state before $t = 240s$ from the beginning of the flow. In the high Reynolds number test cases with bottom opening, the violent mixing and preferential release of denser fluid does not cause a dynamic steady state even if the concentration values from fluorescence appear saturated. In the high

Reynolds number tests with side openings, the violent mixing and bidirectional side flows alters the flow patterns and it releases only the lighter layers of fluid to the ambient fluid domain. The denser layers inside the confinement are trapped at the bottom and the incoming lighter layers are trapped at the top due to buoyancy. Violent mixing can be observed at the locations of strong eddies and near the flow outlet where these two layers are brought in contact. The buoyancy induced density stratification and turbulent kinetic energy involved in mixing acts in opposite manner in the case of mixing. While buoyancy separates the layers and reduces interactions between fluid parcels of different density, turbulent kinetic energy facilitates more interaction and mixing.

Stable neutral level was observed inside the confinement for both side and bottom opening cases for jet flow at $Re = 1500$ but not observed for higher Reynolds number jet cases $Re = 2600, 3700$. This shows that in an actual case of fire emergency, the safe evacuation time available for occupants makes a sudden dip if the Reynolds number approaches 2600 from 1500.

5.1.1 Coefficient of entrainment

Comparing the entrainment coefficients for bottom and side opening cases, the difference in pattern of mixing is evident. While the near-wall side of the jet appears more or less similar in both cases, the far-wall side of the jet has different mixing pattern based on the location of the flow outlet. The entrainment values are higher at the near-field for the side opening cases over the bottom opening case. This is a clear indication of the enhanced mixing by the trapped circulation zones created by the confinement.

5.2 Mode of stratification

If the inlet and outlet are separated by a sufficient distance in displacement ventilation, stable stratification can happen irrespective of the inlet Reynolds number. But in the experiments conducted, the axial dimensions are restricted by the confinement at $17D$ which prevents stable stratifications, especially for the high Reynolds number cases. Therefore the typical patterns of displacement ventilation were not observed in the experiments conducted. The mode of stratification was dependent on the Reynolds number in the experiments conducted. The kinetic energy of the jet fluid was significantly larger than the buoyancy factors in the near-field.

In the case of experiments in confined space with side opening, especially in the cases of buoyant jet with low Reynolds number, if the side opening is near the bottom wall, the bidirectional flow may not happen effectively. In the case of a low momentum jet with

bottom opening and stratification, the stratified layers will put an extra pressure at the bottom outlet to flush out the denser layers of fluid. A finite pressure difference at the outlet makes a unidirectional flow that flushes out the fluid inside whereas a outlet with negligible pressure gradient allows bi-directional flow. The effectiveness of the openings depend mainly on the strength of the source of buoyancy and secondly on the position with respect to the stratification if it exists.

5.3 Confined space with anisotropic turbulence

Due to the continuous mean flow, there would be a large difference in the velocity fluctuation in the vertical direction compared to the horizontal direction in the jet region. But the presence of a $3D$ confinement in the near-field of the jet changes the mean flow direction continuously, which shifts the direction of anisotropy continuously. Since the mixing of components are related to the velocity fluctuations, the continuous shift in anisotropy in velocity fluctuations leads to better mixing of components.

The confined space also puts a limit to the size of the largest eddies, reducing the time scales. The integral time scale is related to the energy transfer between eddies. Reducing the time scale would bring the energy transfer immediately to the smaller sized eddies, where molecular diffusion occurs. Each change in direction of the mean flow by the confinement causes loss of energy making the condition favourable for mixing. Mixing is proportional to the area of interaction of fluid parcels at smaller scales. Increase in strain increases the area of interaction and enhances mixing. Thus the molecular diffusion phase was attained faster in the case of a jet in confinement compared to a free jet.

5.4 Engineering solutions

There is a significant difference between the flow dynamics of a near-field confined jet and a free jet. During a fire, opening a portion of roof near the source can change the flow dynamics of jet and make it similar to a free jet. In the actual case of a fire emergency, weaker fire sources cause smoke to reach the ceiling less mixed and stratify. Facilitating this lighter layer from escaping from the room at tall positions can help in maintaining less mixed air in a room.

In the case of gas leakage from a pressurized pipe, the flow pattern can be predicted based on the inlet Reynolds number and the geometry of the confined space from the present study. This would help in finding the reaction time, safe evacuation time, decide position of ventilators and formulate the safety protocols.

Placing all doors and windows above a certain height from the floor can help in achieving better safety through trapped, unmixed air, for human life and valuable assets. Sufficiently tall ceiling levels (far-field, based on possible sizes of gas leakage points) would help in these cases to hold all the dangerous gases allowing some time for safe evacuation whereas stronger sources of fire would make the gases mixed with the room atmosphere from lower heights. This would significantly reduce the time to evacuate the occupants to safety. The design of roof and wall openings need to be made carefully based on the near and far-field distances from possible jet sources to reduce the dangerous gases concentration inside the room and also to provide sufficient time for safe evacuation.

Stratification can be used to localise the lighter fluid at the top levels. Tilted roofs with openings at the highest points will favour stratification and preferential release of the lightest smoke (highest temperature air). Unlike the case of unconfined buoyant jet where the jet-core travels a distance, loses momentum and behaves like a plume, the confinement in the experiments conducted affects the unmixed jet-core and causes spreading in all horizontal direction which leads to higher mixing at the bottom plate. The buoyant jet after hitting the confinement will travel along these walls. If the walls are made in a manner so as to direct the flows to an opening, the outflow can be made more efficient.

5.5 Future works

Synchronized PIV-PLIF measurements can be done on selected regions to improve the resolution of data and quantify the concentration better. The fast moving jet and the slow buoyancy driven convection can be separately analysed in this way. Experiments with higher density differences and combination of roof and wall openings at different positions and shapes also can be done. The set up may be modified to perform $3D$-PIV tests also.

The derivatives of values obtained from PIV data have lesser resolution than the PIV data in each step. Increasing the resolution can help in resolving finer structures of turbulence and extract higher resolution data from derived quantities. In this way eddy viscosity and turbulent kinetic energy can be studied in detail. Obtaining turbulent kinetic energy and high resolution buoyancy field helps in understanding the pattern of mixing and stratification. The relationship between self-similarity obtained at near-field in confinement and the background turbulence can also be studied.

The modes of outflow from the confinement can be studied based on the Rayleigh-Taylor instabilities at the flow exits and the whole confinement. This would help in finding

optimum position and opening sizes for rooms to handle fire emergency. The study can be extended to buoyant plumes also to address the wide range of cases encountered in fire emergencies. The position of flow exits can be also checked based on the neutral level inside the confinement in the case of low Reynolds number flows.

Appendix

.1 Unsteady turbulent round jet

.1.1 Temporal evolution of centreline velocity

The variation of centreline velocity at different axial locations from time $t = 5 - 50s$ are shown in the following plots. The values show high degree of fluctuation throughout the duration of recording. They also show a gradual reduction in the magnitude of centreline velocity.

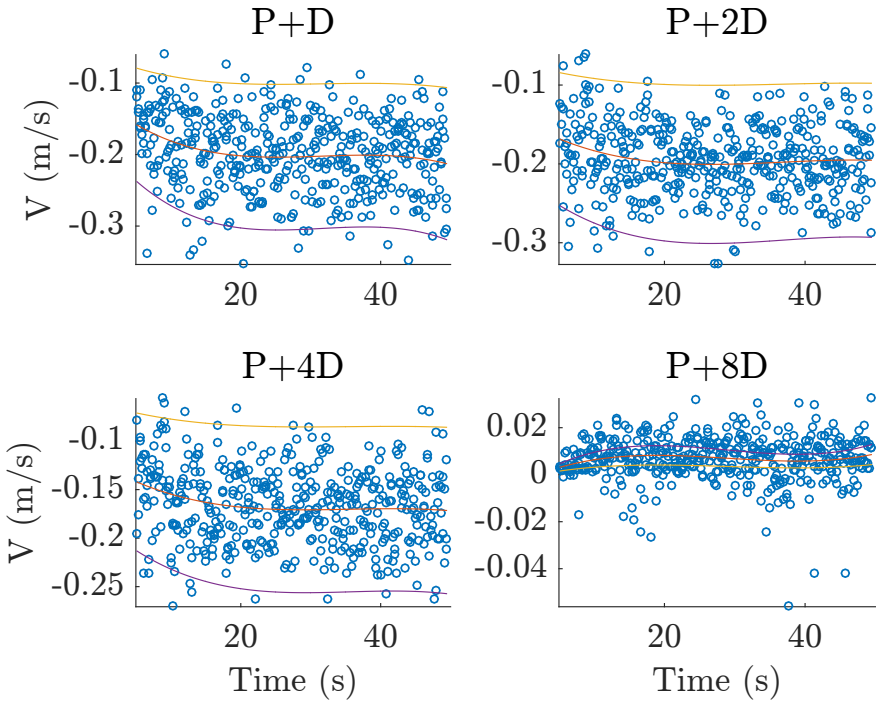

Figure 1: Temporal evolution of centreline velocity, $0.88lpm$ inflow rate, $\phi 30mm$ side opening $(t = 5 - 50s)$(P is the end of inlet and D is the inlet diameter)

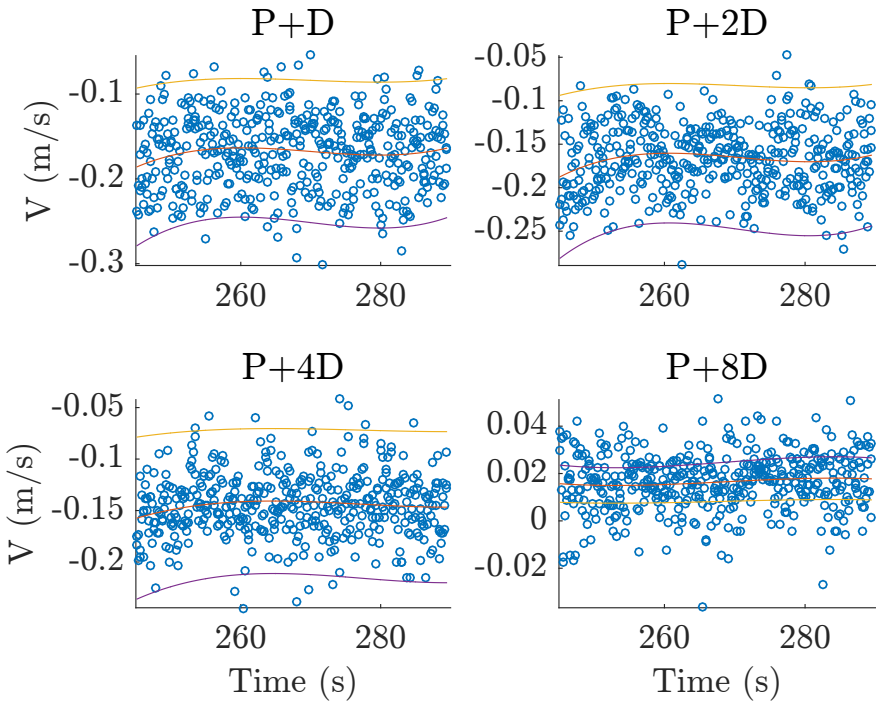

Figure 2: Temporal evolution of centreline velocity, $0.88lpm$ inflow rate, $\phi 30mm$ side opening $(t = 245 - 290s)$(P is the end of inlet and D is the inlet diameter)

.1.2 Autocorrelation tests on the temporal profile of centreline velocity

Autocorrelation tests were conducted on the temporal profile of centreline velocity and it was found that the velocity values at different time instants are weakly correlated.

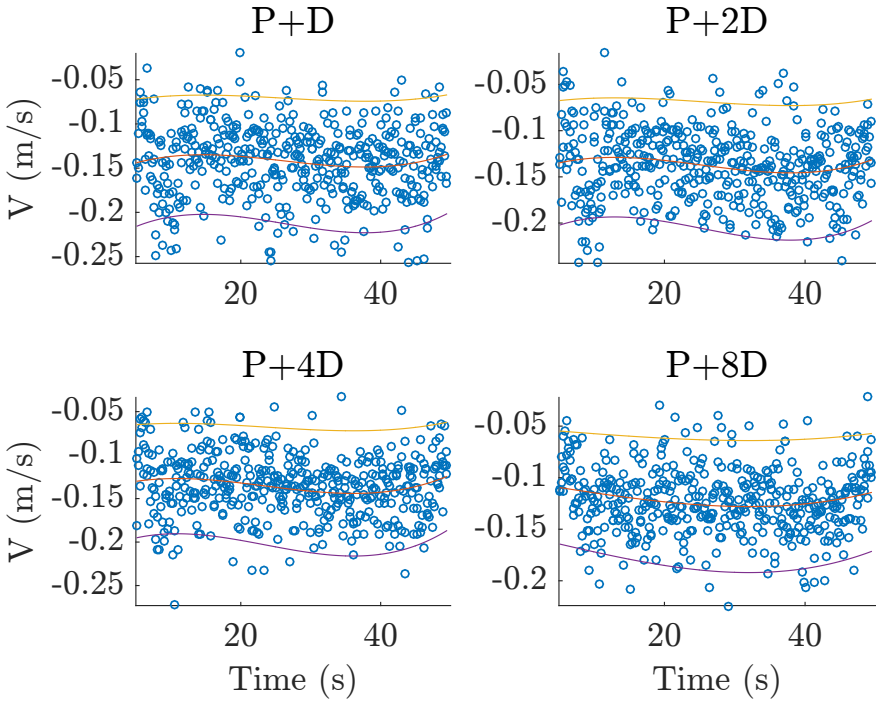

Figure 3: Temporal evolution of centreline velocity, $0.88lpm$ inflow rate, $\phi 30mm$ bottom opening $(t = 5 - 50s)(P$ is the end of inlet and D is the inlet diameter)

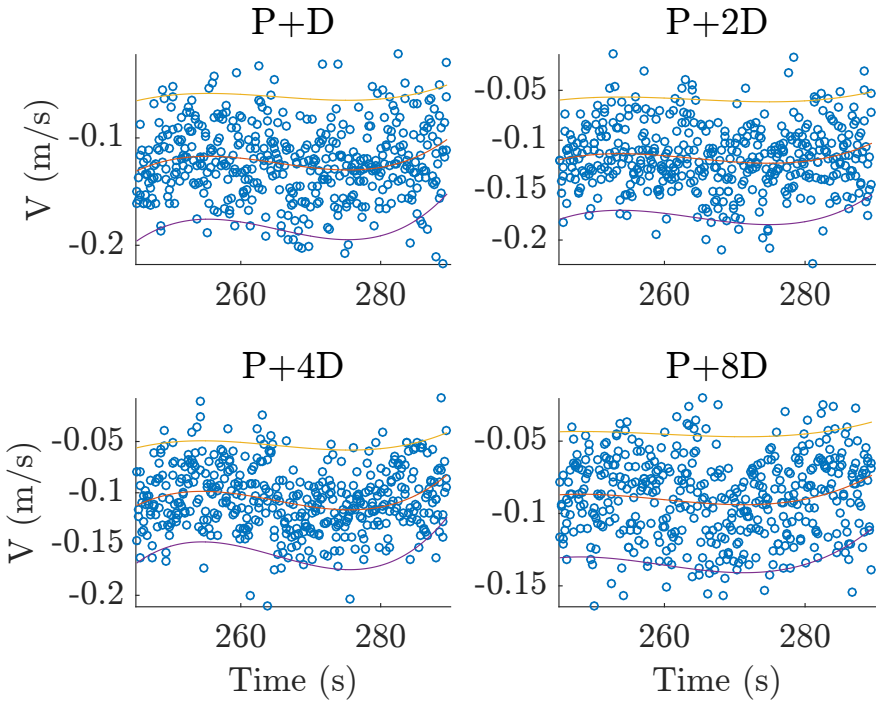

Figure 4: Temporal evolution of centreline velocity, $0.88lpm$ inflow rate, $\phi 30mm$ bottom opening $(t = 245 - 290s)(P$ is the end of inlet and D is the inlet diameter)

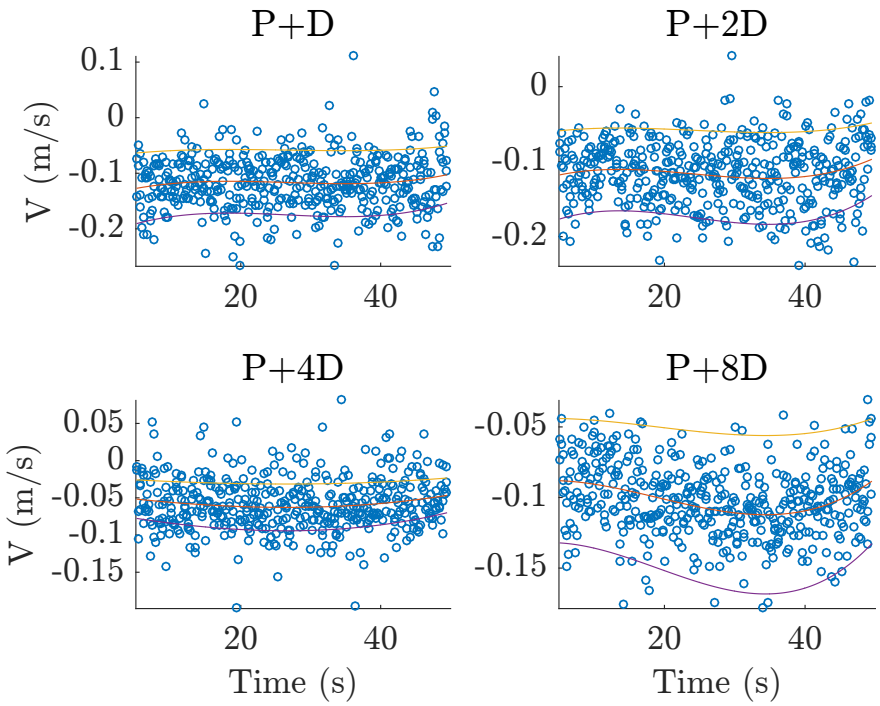

Figure 5: Temporal evolution of centreline velocity, $0.489lpm$ inflow rate, $\phi 30mm$ side opening $(t = 5 - 50s)(P$ is the end of inlet and D is the inlet diameter)

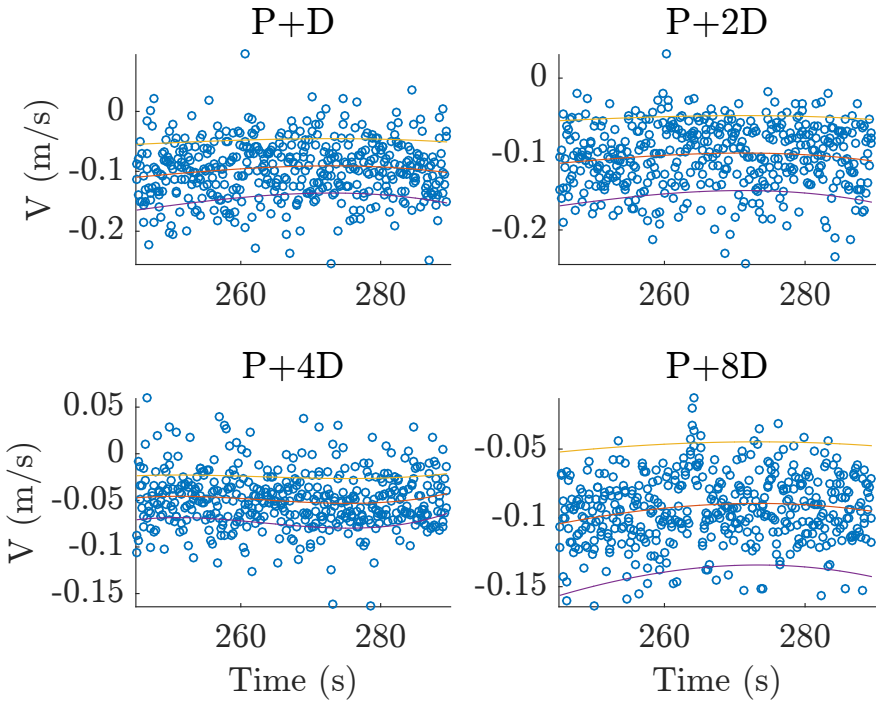

Figure 6: Temporal evolution of centreline velocity, $0.489lpm$ inflow rate, $\phi 30mm$ side opening $(t = 245 - 290s)(P$ is the end of inlet and D is the inlet diameter)

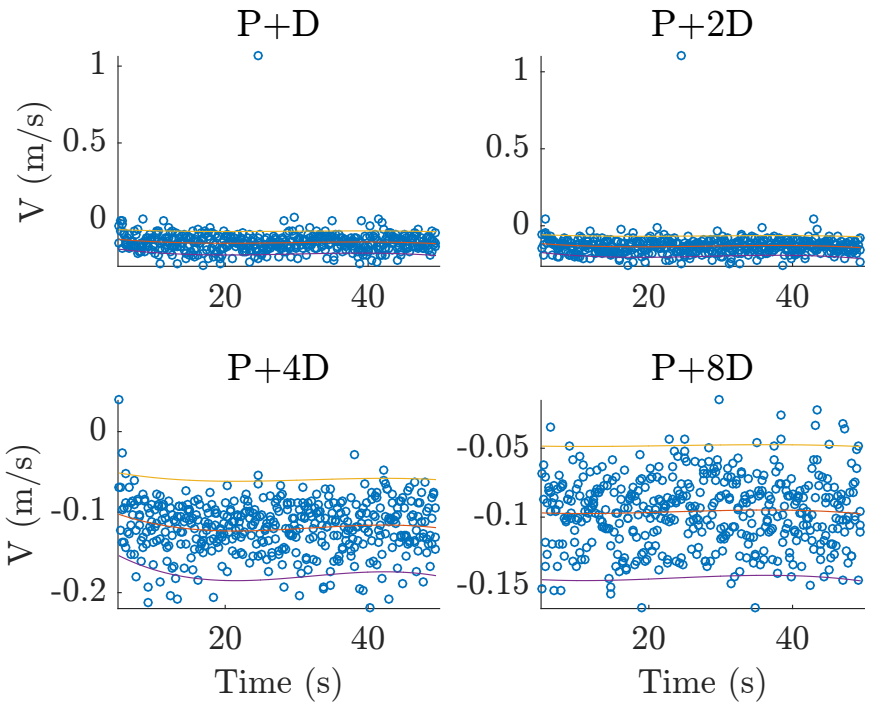

Figure 7: Temporal evolution of centreline velocity, $0.489lpm$ inflow rate, $\phi 30mm$ bottom opening $(t = 5 - 50s)(P$ is the end of inlet and D is the inlet diameter)

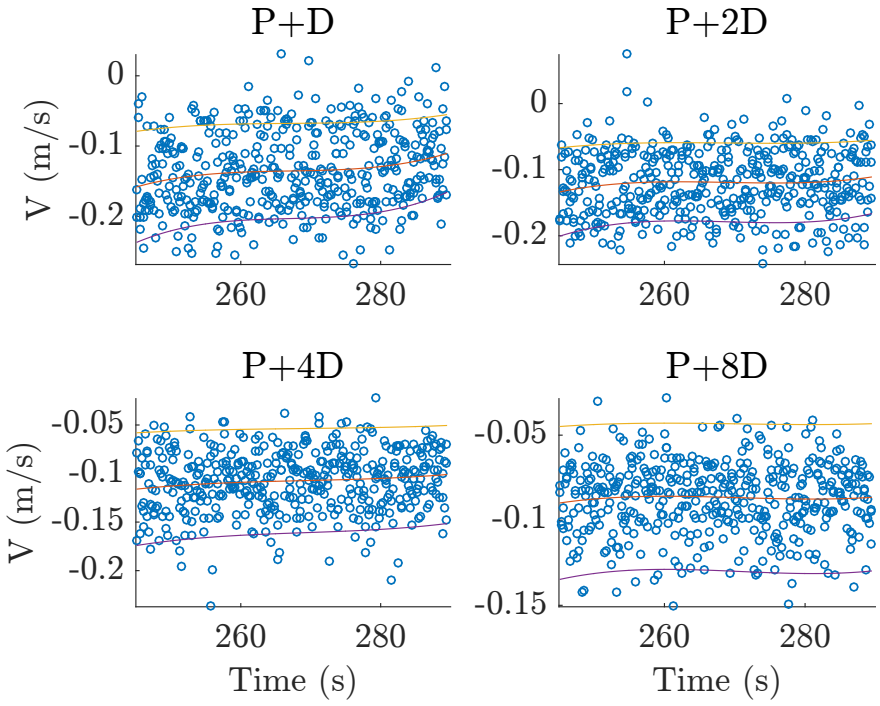

Figure 8: Temporal evolution of centreline velocity, $0.489lpm$ inflow rate, $\phi 30mm$ bottom opening $(t = 245 - 290s)(P$ is the end of inlet and D is the inlet diameter)

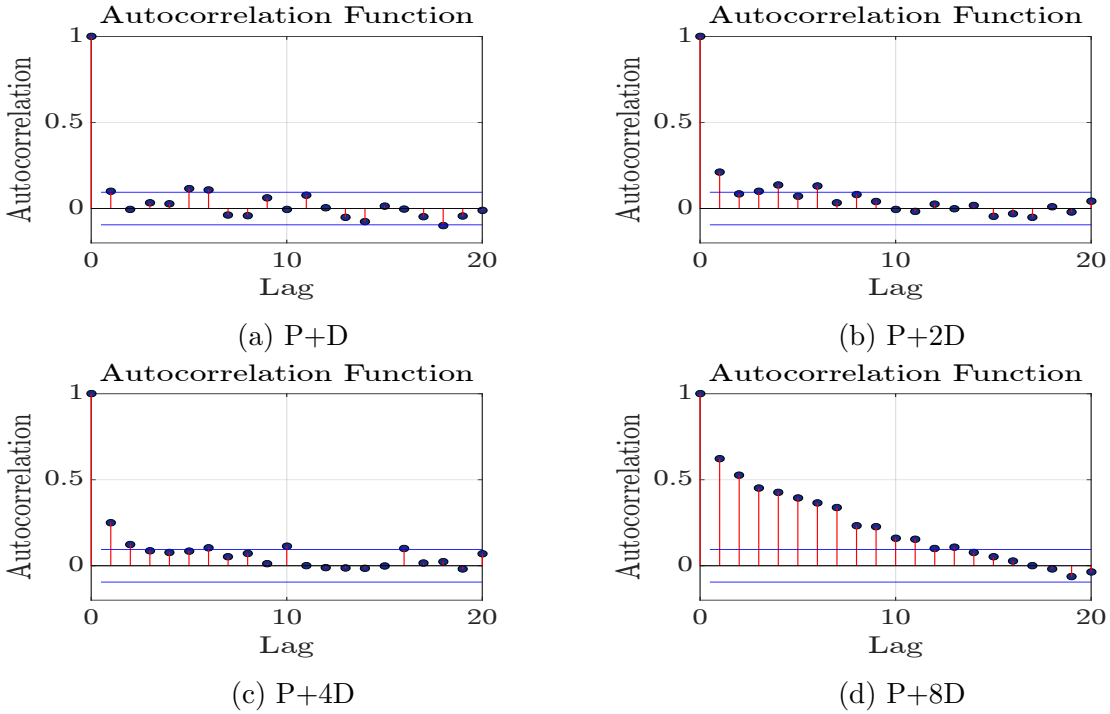

(a) P+D (b) P+2D

(c) P+4D (d) P+8D

Figure 9: Autocorrelation of the centreline velocity at different axial locations from time, $t = 5 - 45s$, for a confinement with side opening of $\phi 30mm$ and jet inlet flow rate = $0.88lpm$

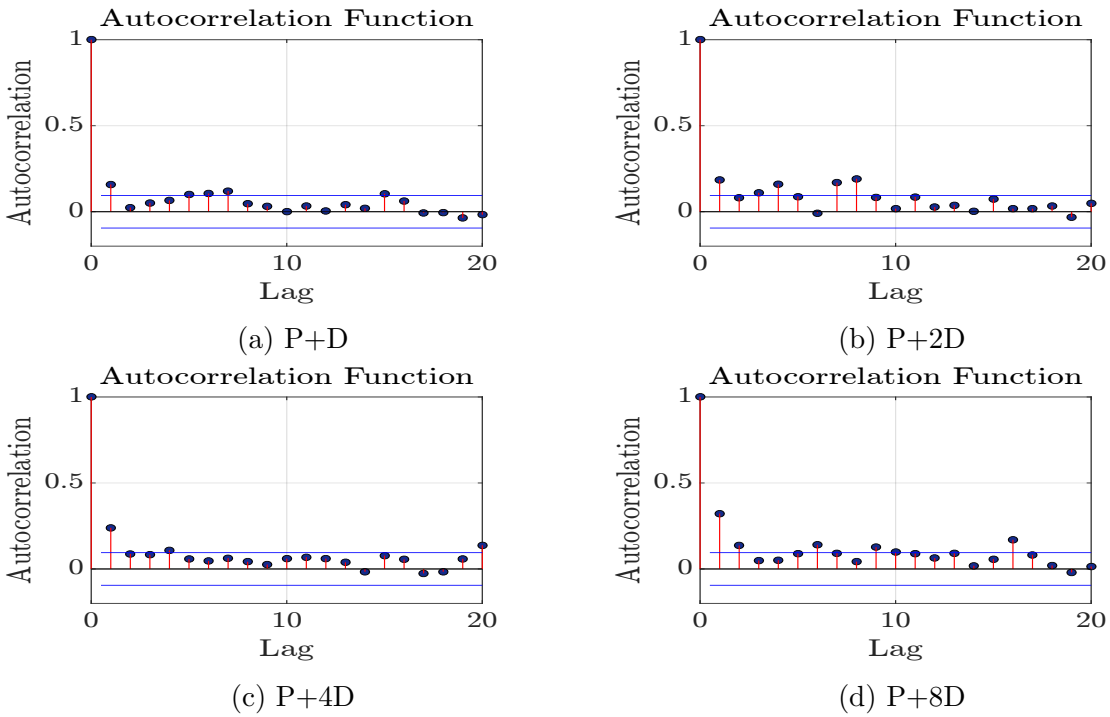

(a) P+D (b) P+2D

(c) P+4D (d) P+8D

Figure 10: Autocorrelation of the centreline velocity at different axial locations from time, $t = 5 - 45s$, for a confinement with bottom opening of $\phi 30mm$ and jet inlet flow rate = $0.88lpm$

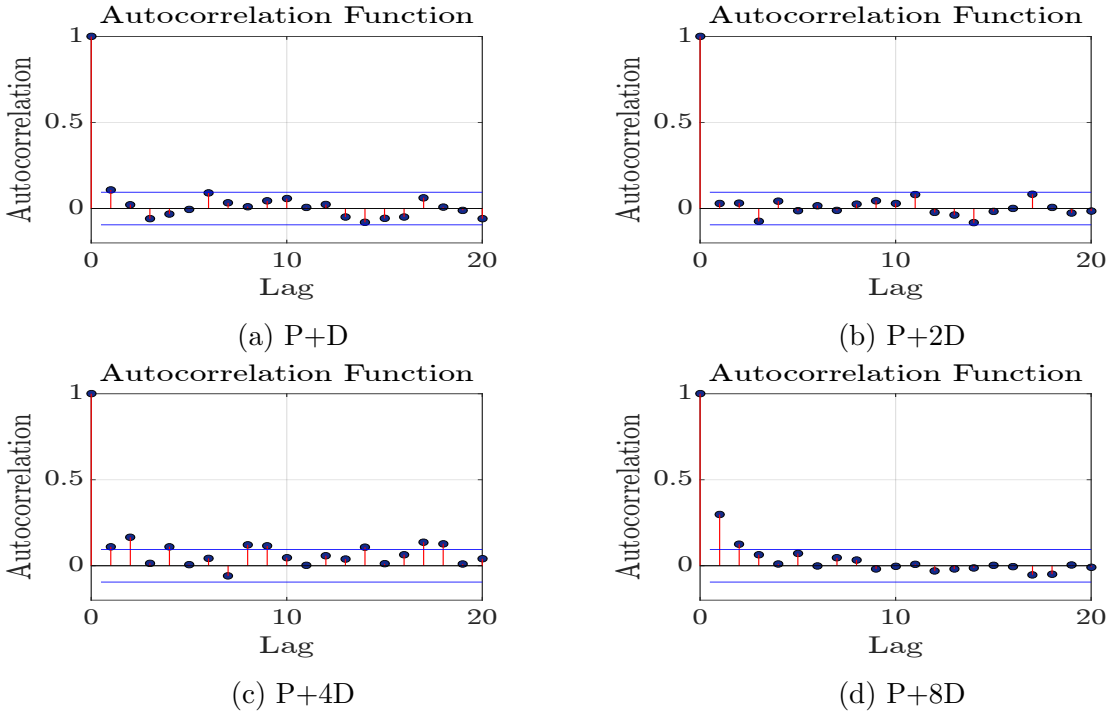

(a) P+D (b) P+2D

(c) P+4D (d) P+8D

Figure 11: Autocorrelation of the centreline velocity at different axial locations from time, $t = 5 - 45s$, for a confinement with side opening of $\phi 30mm$ and jet inlet flow rate $= 0.489lpm$

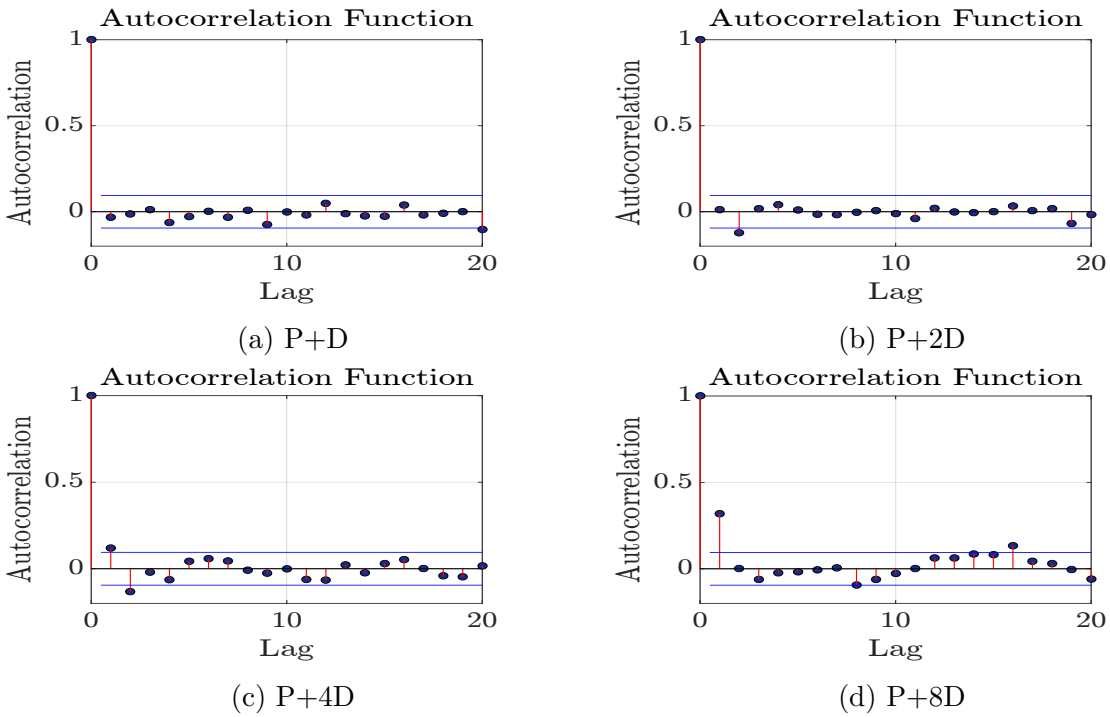

(a) P+D (b) P+2D

(c) P+4D (d) P+8D

Figure 12: Autocorrelation of the centreline velocity at different axial locations from time, $t = 5 - 45s$, for a confinement with bottom opening of $\phi 30mm$ and jet inlet flow rate $= 0.489lpm$

.2 Velocity-Concentration correlations

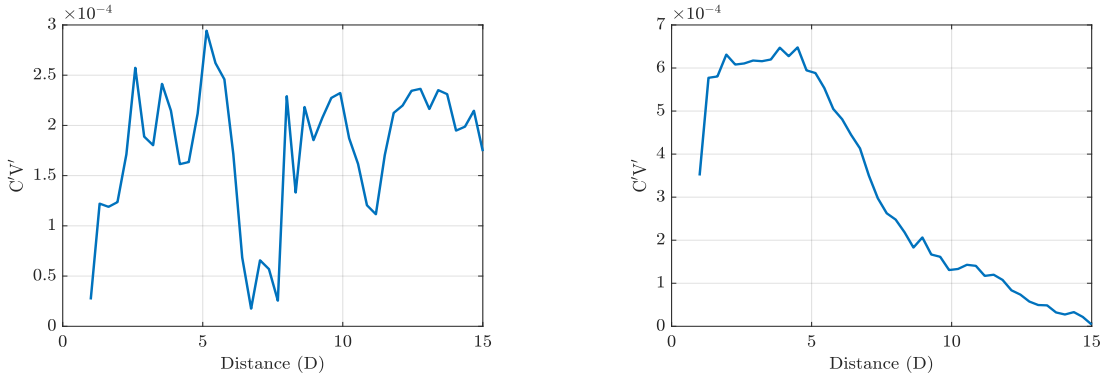

(a) Side Opening Geometry (b) Bottom Opening Geometry

Figure 13: Velocity-Concentration correlation for confinement with side and bottom opening of $\phi 30mm$ (flow rate $= 0.489lpm$, $Re \approx 1500$, $t = 5 - 50s$)

.3 Synchronized PIV-PLIF data

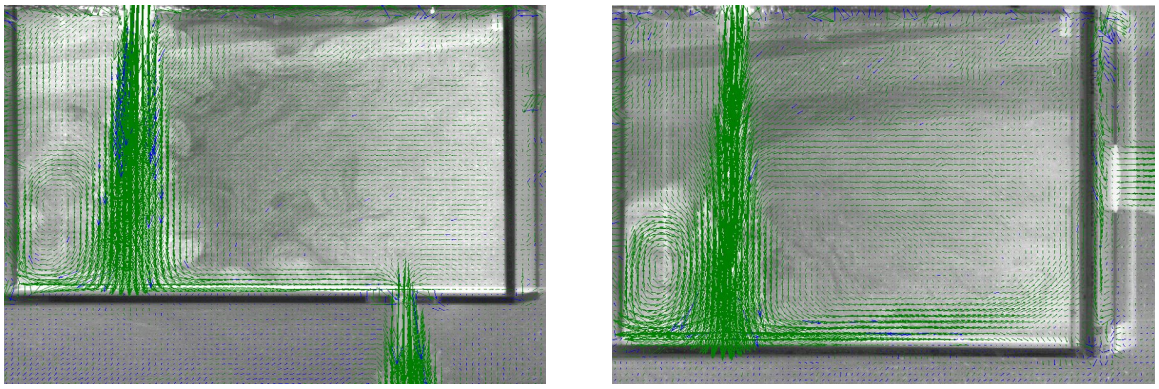

(a) Confinement with bottom opening (b) Confinement with side opening

Figure 14: PIV and PLIF results overlapped. It can be observed that the flow velocity of the buoyancy driven convection in the far region of the jet inside the confinement is far lesser in magnitude compared to the flow velocity in the jet domain.

Bibliography

[1] Abramovich G.N. *The Theory of Turbulent Jets*. The MIT Press

[2] Adel Abdel-Rahman *A Review of Effects of Initial and Boundary Conditions on Turbulent Jets*. WSEAS Transactions on Fluid Mechanics, Issue 4, Volume 5, 2010, 257-275

[3] Adrian Wing-Keung Law, Hongwei Wang. *Measurement of mixing processes with combined digital particle image velocimetry and planar laser induced Fluorescence*. Experimental Thermal and Fluid Science, 22 (2000) 213-229

[4] Alahyari, A., Longmire, E. K *Particle image velocimetry in a variable density flow: application to a dynamically evolving microburst*. Experiments in Fluids, Vol. 17, 6 (1994)434-440

[5] Andreopoulos, J. and Rodi, W. *Experimental investigation of jets in a crossflow*. Journal of Fluid Mechanics, 138 (1984) 93-127

[6] Becker, H. A., Massaro, T. A. *Vortex evolution in a round jet*. Journal of Fluid Mechanics, (1968) 3 1 :435-48

[7] Boree.J, Atassi.N and Charnay.G *Phase averaged velocity field in an axisymmetric jet subject to a sudden velocity decrease*. Exp. Fluids 21(6), 447–456 1996

[8] Boree.J, Atassi.N, Charnay.G and Taubert.L *Measurements and image analysis of the turbulent field in an axisymmetric jet subject to a sudden velocity decrease*. Exp. Therm. Fluid Sci. 14 (1), 45–51, 1997

[9] Brown, G.L., Roshko, A. *On density effects and large scale structure in turbulent mixing layers*. Journal of Fluid Mechanics, (1974) 64 775-816.

[10] Charonko and Vlachos *Estimation of uncertainty bounds for individual particle image velocimetry measurements from cross correlation peak ratio*. Meas Sci Technol, 24(6) 065301, (2013)

[11] Crimaldi J.P. *Planar laser induced fluorescence in aqueous flows*. Exp Fluids (2008) 44:851–863, DOI 10.1007/s00348-008-0496-2

[12] Crow, S. C., Champagne , F. H *Orderly structure in jet turbulence.* Journal of Fluid Mechanics, (1971) 48:547-91

[13] Dahm, W.J.A, Dimotakis, P.E. *Measurements of entrainment and mixing in turbulent jets.* AIAA J. 25, 1216-1223 (1987); AIAA Paper 85-0056

[14] Dahm W.J.A., Dimotakis P.E. *Mixing at large Schmidt number in the self-similar far field of turbulent jets.* Journal of Fluid Mechanics, 217 (1990), pp. 299-330

[15] Dantec Dynamics *DynamicStudio users guide.* Dantec.

[16] Dimotakis, P.E. *Turbulent Mixing.* Annu. Rev. Fluid Mech. 2005. 37:329–56

[17] Dimotakis P.E, Miake-Lye R.C and Papantoniou D.A *Structure and dynamics of round turbulent jets.* Physics of Fluids, 26(11), pp. 3185-3192 (1983)

[18] Dong-hyuk Shin, A.J. Aspden and Edward S. Richardson *Self-similar properties of decelerating turbulent jets.* Journal of Fluid Mechanics, (2017), vol. 833, R1

[19] Eckart C. *An analysis of the stirring and mixing processes in incompressible fluids.* J.Mar.1948 Res.7:265–75

[20] Fannelop T.K, D.M. Webber *On buoyant plumes rising from area sources in a calm environment.* Journal of Fluid Mechanics, (2003), vol. 497, pp. 319–334.

[21] Fellouah .H *The velocity spectra and turbulence length scale distributions in the near to intermediate regions of a round free turbulent jet.* Phys. Fluids 21, pp.115101 (2009)

[22] Freymuth, P. *On transition in a separated laminar boundary layer.* Journal of Fluid Mechanics, (1966) 25:683-704

[23] Gartrell, G. *Studies on the mixing in a density-stratified shear flow.* PhD thesis. (1979) Calif. Inst. Technol., Pasadena, Calif. 446 pp.

[24] Gauntner, J.W., Hrycak, P., Lee, D.T., Livingood, J.N.B. *Experimental flow characteristics of a single turbulent jet impinging on a flat plate.* NASA Technical Reports Server

[25] George W.K and Davidson .L *Role of Initial Conditions in Establishing Asymptotic Flow Behavior.* AIAA J, Vol.42, No.3, 2004, pp.438-446.

[26] Hannoun I.A *Matching the Refractive Index in Density Stratified Flows.* Technical Memorandum 85-1, WK Keck Laboratory of Hydraulics and Water Resources, California Institute of Technology (1985)

[27] Holger Martin *Heat and Mass Transfer between Impinging Gas Jets and Solid Surfaces.* Advances in Heat Transfer 1977

[28] Horn .G, Thring M. W *Angle of Spread of Free Jets.* Nature, volume 178, pages 205–206 (1956)

[29] Jamil Zinoubi, Rejeb Ben Maad, Ali Belghith *Influence of the vertical source–cylinder spacing on the interaction of a thermal plume with a thermosiphon flow: an experimental study.* Experimental Thermal and Fluid Science 28 (2004) 329–336.

[30] Jung .D, Gamard .S, and George W. K *Downstream evolution of the most energetic modes in a turbulent axisymmetric jet at high Reynolds number. Part 1. The near-field region.* Journal of Fluid Mechanics, (2004) 514, pp. 173

[31] Kaminski, E. Tait, S. and Carazzo, G. *Turbulent entrainment in jets with arbitrary buoyancy.* Journal of Fluid Mechanics, (2005), vol. 526, pp.361–376

[32] Konrad, J.H. *An experimental investigation of mixing in two-dimensional turbulent shear flows with applications to diffusion-controlled chemical reactions.* Ph.D. thesis, 1976, California Institute of Technology

[33] Kwon S.J, and Seo I.W *Reynolds number effects on the behaviour of a nonbuoyant round jet.* Exp. Fluids, Vol.38, 2005, pp.801–812.

[34] Linden P.F. *The fluid mechanics of natural ventilation.* Annual Rev. Fluid Mech. 1999. 31:201–38

[35] Linden P.F., Lane - Serff G.F. and Smeed D.A. *Emptying filling boxes : The Fluid Mechanics of Natural Ventilation.* Journal of Fluid Mechanics, (1990), vol. 212, p p . 309-335

[36] List E.J *Turbulent jets and plumes.* Ann. Rev. Fluid Mech. (1982) 14:189-212

[37] Mcdougall, Trevor .J *On the elimination of refractive-index variations in turbulent density-stratified liquid flows.* Journal of Fluid Mechanics, Vol. 93, 1 (1979)83–96

[38] Mcnaughton K.J. and Sinclair C.G. *Submerged jets in short cylindrical flow vessels.* Journal of Fluid Mechanics, (1966), 25, 367–375

[39] Morton B.R., Sir Geoffrey Taylor, F.R.S., Turner J.S. *Turbulent gravitational convection from maintained and instantaneous sources.* Proceedings of the Royal Society A, 24 January 1956.DOI: 10.1098/rspa.1956.0011

[40] Papantoniou D.A. *Observations in turbulent buoyant jets by use of laser-induced fluorescence.* Ph.D. thesis, California Institute of Technology, 1985

[41] Papantoniou .D.A, List E.J. *Large-scale structure in the far field of buoyant jets.* Journal of Fluid Mechanics, 209 (1989), pp. 151-190

[42] Petrov .V, Manera .A *Validation of Star-CCM+ for Buoyancy Driven Mixing in a PWR Reactor Pressure Vessel.* Proc. 14th Int. Topl. Mtg. on Nuclear Reactor Thermal-Hydraulics (NURETH-14), Toronto, Canada, September 25–30, 2011 (2011)

[43] Rajaratnam .N and Flint-Peterson .L *Low Reynolds number circular turbulent jets.* Proc. Inst. of Civil Engineers, London, Vol. 87, 1989, pp. 299-305.

[44] Reungoat, D., Rivière, N., and Fauré, J.P. *3C PIV and PLIF Measurement in Turbulent Mixing (Round Jet Impingement).* Journal of Visualization, Vol. 10, No. 1 (2007)99-110

[45] Ricou .F, and Spalding D.B *Measurements of entrainment by axisymmetric turbulent jets.* Journal of Fluid Mechanics, Vol.11, (1961) pp.21-32.

[46] Robert E. Breidenthal *Elements of entrainment.* Article

[47] Roshko, A. *Structure of turbulent shear flows: A new look.* AIAA J., 1976, 14(10) 1349-1353.

[48] Ruud Weersink *Experimental study of the oscillatory interaction between two free opposed turbulent round jets.* MS Thesis, Syracuse University, University of Twente, 2010

[49] Sciacchitano *et al. PIV uncertainty quantification by image matching.* Meas Sci Technol, 24 045302, (2013)

[50] Sunming Qin, Benedikt Krohn, John Downing, Victor Petrov, Annalisa Manera *High-Resolution Velocity Field Measurements of Turbulent Round Free Jets in Uniform Environments.* Nuclear Technology, Vol. 205, 1-2 (2019)213-225

[51] Sunming Qin, Benedikt Krohn, Victor Petrov and Annalisa Manera *Velocity and Scalar Fields of a Turbulent Buoyant Jet in the Self-Similar Region.* Nuclear Technology, (2019)1-15

[52] Tennekes H., Lumley J.L *A first course in turbulence.* The MIT Press

[53] Tokumaru P.T, Dimotakis P.E. *Image correlation velocimetry.* Experiments in Fluids 19 (1995) 1 15 9 Springer-Verlag 1995

[54] Tollmien .W *Berechnung Turbulenter Ausbreitungsvorgänge.* ZAMM-Journal of Applied Mathematics and Mechanics/Zeitschrift für Angewandte Mathematik und Mechanik, 6(6), pp. 468-478 (1926)

[55] Uriel Frisch *Turbulence: The Legacy of A. N. Kolmogorov*. Cambridge University Press

[56] Wehrmann, 0., Wille, R. *Beitrag zur Phanomenologie des laminar-turbulenten Obergange im Freistrahl bei kleinen Reynoldszahlen*. In Boundary Layer Research. (1957) lUTAM Sym. Frieburg. ed. H . Gortler, p p . 387-403